5-8-2024

Flavor Equilibration in Neutron Star Mergers

Ziyuan Zhang
Washington University in St. Louis

WASHINGTON UNIVERSITY IN ST. LOUIS
Department of Physics

Dissertation Examination Committee:
Mark Alford, Chair
Robert Charity
Willem Dickhoff
Zohar Nussinov
Saori Pastore

Flavor Equilibration in Neutron Star Mergers

by
Ziyuan Zhang

A dissertation presented to
Washington University in St. Louis
in partial fulfillment of the
requirements for the degree
of Doctor of Philosophy

May, 2024
St. Louis, Missouri

Table of Contents

List of Figures

List of Tables

Acknowledgements

First, I would like to thank my advisor Prof. Mark Alford. He brought me into the field of theoretical physics and phenomenology. He taught me how to think as a theorist, and taught me the way to understand and model physical systems and processes. He also introduced me to the MUSES collaboration, where there are plenty of exciting physics going on. During the five years in the group, I have learned a lot.

Second, I would like to thank members of my committee, Prof. Saori Pastore, Prof. Willem Dickhoff, Prof. Zohar Nussinov, and Prof. Robert Charity for reading this thesis and providing valuable feedback. In particular, I would like to thank Saori and Wim for being on my committee for the past few years and for providing helpful suggestions.

I would like to thank all other members in the group, Dr. Alex Haber, Dr. Steven Harris, and Liam Brodie, for helpful discussions. I would also like to thank all PIs and members in MUSES, Prof. Nicolas Yunes, Prof. Jacquelyn Noronha-Hostler, Prof. Jorge Noronha, Prof. Claudia Ratti, Prof. Veronica Dexheimer, Dr. Andrew Manning, and so on, for starting such a great collaboration. I would also like to thank, Prof. Ramanath Cowsik and Prof. Bradley Jolliff, who awarded me the McDonnell fellowship to support 3 years of research.

I would like to thank friends and officemates, Daria Kowsari, Will Charles, Linghan Zhu, Xilong Xu, Du Li, Haonna Wang, Mutian Shen, Dingyi Ye, Zeyuan Ye, Yizhou Wang, and Ziyan Li, JR Cruise, Takuya Okawa. Thank everyone for having such a joyful time together.

I would like to thank every colleague at Morgan Stanley, where I interned at. It has been an amazing time.

A special thanks to Guanxiu Lin. Meeting you is one of the most wonderful and happiest things in my life.

A special thanks to Peidong Wang. Time has passed quickly. It has been 10 years since

we first met. You have been inspiring me for long. I still remember the first time you took me to the MIT campus. When we randomly walked into a classroom and saw some words on the blackboard saying "Hard work is the only solution to success. So don't give up". It has really been encouraging me and keeping up.

Most of all, I would like to thank my parents and my family for their love and support. I hope I will be a proud of my family one day.

Ziyuan Zhang

Washington University in St. Louis

May, 2024

ABSTRACT OF THE DISSERTATION

Flavor Equilibration in Neutron Star Mergers

by

Ziyuan Zhang

Doctor of Philosophy in Physics

Washington University in St.Louis, 2024

Professor Mark Alford (Chair)

Neutron star mergers probe the high-density and high-temperature regime of dense matter. The mergers can reach several times saturation density, and their temperatures can reach up to a hundred MeV. Simulations are essential for a better understanding of dense matter physics and for comparing theoretical predictions with observations. Current merger simulations, based on numerical general relativity and hydrodynamics, lack microphysical inputs. Therefore, the goal of the thesis is to develop models and provide microphysical insights for the theory community and the merger simulation community. Specifically, it includes the state-of-the-art study on flavor equilibration under neutron star merger conditions. This includes significant improvements on direct and modified Urca calculations, and the development of a unified approach to Urca processes, etc. As part of the MUSES framework, the physics has been implemented in the flavor equilibration module and is ready for use by the communities.

In the first chapter, we will make a short introduction to neutron star mergers and the equation of states that describe the matters in the merger. In the second chapter, we present the state-of-the-art direct Urca calculations and subsequently correct the traditional cold beta-equilibrium. In the third chapter, we estimate the isospin relaxation rates, and find

that at temperatures around five MeV, the relaxation timescale is comparable to the timescale of the density oscillations in the mergers, which produces a resonant peak in bulk viscosity. In the fourth chapter, we first provide the state-of-the-art modified Urca calculation, which is the first full phase space, fully relativistic rate calculation. In order to solve an unphysical divergence issue in the modified Urca calculation, we tackle the problem in two ways, and one of them leads to a unified approach that includes all Urca processes. In the fifth chapter, we give a short introduction to MUSES and our flavor equilibration module. Besides, in order to use a better interpolation scheme, we explored and implemented the Gaussian process regression, which outperforms linear interpolation in accuracy.

Chapter 1

QCD Phase Diagram and the MUSES Framework

1.1 QCD Phase Diagram

The strong force is one of the four fundamental forces in Nature. It binds together nucleons to counter electromagnetic force and form nuclei. The theory that describes the strong force most successfully is Quantum Chromodynamics (QCD). The fundamental degrees of freedom are quarks and gluons that mediate the interaction.

An important mission of the study of QCD and QCD matter is to map out its phase diagram. Like water takes the form of 3 different phases in the temperature-pressure space, QCD matters can be in different phases in the baryon chemical potential μ_B and the temperature T plane (see Fig. 1.1) [6, 7, 8, 9, 10]. If studying asymmetric matter (asymmetric in up and down quarks, or neutron and protons) where the isospin chemical potential μ_I is non-zero, one would include a third axis [11].

In principle, one would solve the path integral to obtain the partition function, and hence the thermodynamic quantities (i.e. equation of states [10, 12, 13, 14, 15, 16, 17]) to describe the QCD matter in various phases. However since QCD is hard to solve directly, researchers

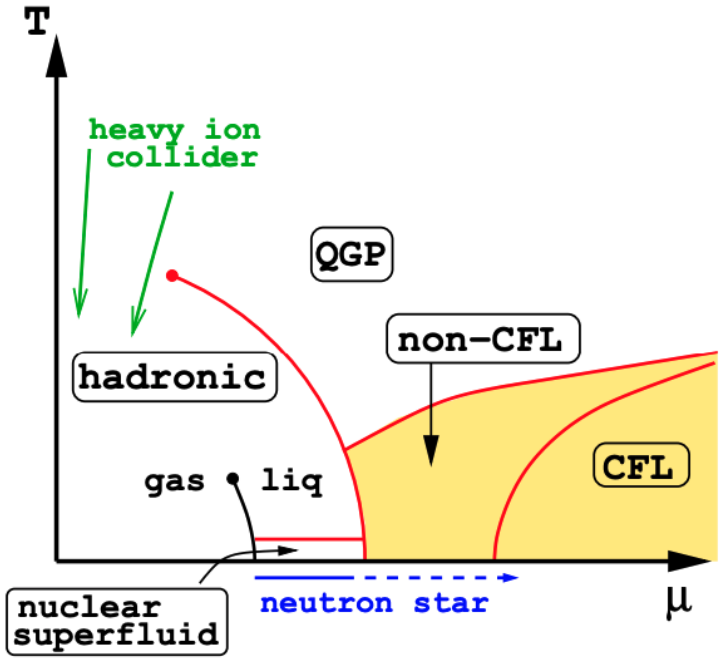

Fig. 1.1: A schematic plot for the QCD phase diagram [1].

use different methods and probes to study different regimes of the relevant parameter space.

Lattice QCD is an approach that solves QCD on a lattice. It can solve for $\mu_B = 0$. For finite μ_B, expansion schemes allow it to give reliable results up to $\mu_B/T \sim 3.5$ [18]. Above this μ_B, the weightings of the configurations become imaginary, and this is the well-known sign problem in lattice QCD [19, 20, 21, 22, 23].

In regimes where μ_B or T is large, the QCD coupling becomes small. This is because of the asymptotic property of QCD, an anti-screening effect. In these regimes, one can solve QCD perturbatively. pQCD gives reliable results when $T \geq 300$MeV or $n_B \geq 40n_0$, where n_0 is the nuclear saturation density [24, 25, 26].

In regimes where the temperature is low, an approach reliable for up to $\sim 2n_0$ is the chiral effective theory (χEFT). It preserves the chiral symmetry of QCD and allows for systematic

expansions of 2-body and 3-body nucleon-nucleon interactions [27]. It also employs a systematic study of uncertainties, which are constrained below $2n_0$. It is a good approximation of QCD at low density or low baryon chemical potential [17, 28, 29, 30].

At low densities and temperatures, the matter is in the hadron gas phase. The model that describes this phase is the hadron resonance gas model [31, 32]. As temperature and density increase, it is generally believed that there is a deconfinement phase transition from hadrons to the quark-gluon plasma phase [33, 34]. At very low temperatures, there is also a liquid-gas phase transition line around $\mu_B \sim 939\,\mathrm{MeV}$, where the baryon onset is [35, 36, 37].

At low temperatures and high densities, neutron stars and neutron star mergers are good probes to understand nuclear matter and possibly quark matter phases. Understanding flavor equilibration dynamics in neutron stars and neutron star mergers is the topic that the thesis is contributing to.

1.2 Neutron Stars and Neutron Star Mergers

Neutron stars are produced in supernova explosions. It is the densest object in the universe except black hole. It can reach above twice the solar mass while its radius is only about 10 to 12 km. The current maximum mass observed is $M_{\max} = 2.14^{+0.10}_{-0.09}\,M_\odot$ from NANOGrav [38], followed by an update $M_{\max} = 2.072^{+0.067}_{-0.066}\,M_\odot$ from NICER [39].

In the outer crust, electrons have Fermi energy larger than the binding energy to the nuclei, so electron gas is formed. In this part of the neutron star, matter mainly consists of nuclei lattice and free electrons. In the inner crust, nucleons start to disassociate with nuclei, and neutron superfluid is formed. In this part of the neutron star, there are free electrons, free neutrons, and nuclei lattices. In the inner crust, some new forms of matter called nuclear pasta are proposed [10, 40]. As density increases, in the outer core, there is

no more individual spherical nucleus, but rather, a sea of neutrons, protons, electrons, and muons, modeled as infinite nuclear matter. As density further increases, in the inner core, the forms of matter are not clear yet. Hyperons, condensates, and quark matter may exist [41, 10].

In 2017, the discovery of the event GW170817 opened a new window for exploring dense matter [42]. Since then, there are more NS-NS, NS-BH, and BH-BH mergers being observed [43, 44, 45, 46]. An isolated neutron star long after supernova is considered cold, whose temperatures are less than 1 MeV, whereas a neutron star merger can reach temperatures up to tens of MeV [47]. The mergers can also reach several times nuclear saturation density, depending on the equation of state (more introduction in Sec. 1.3). Observations can help understand, model, infer, and constrain microphysics [48, 49, 50, 51, 52, 53, 54].

Before the merger happens, two neutron stars orbit around each other. The strong gravitational force begins to deform the stars and gravitational waves start to emit. This is the inspiral phase. As the neutron stars start to touch and merge, the merging system becomes much more complicated. The frequency increases from hundreds of Hz to the kHz range, and matters are out of equilibrium [55]. For the first 20 ms, gravitational waves continue to emit, and decay after about 20 ms. Angular momentum redistribution and neutrino interactions become the dominant processes [47]. If the remnant survives after several seconds, it gradually spins down, or it can collapse into a black hole.

The neutron star merger simulations are based on numerical general relativity and hydrodynamics. At the current stage, merger simulations lack microphysical input for the merger and postmerger phases. Therefore, this thesis is aiming at better understanding the important microphysics of the merger.

1.3 Equation of State

Equation of state describes the thermodynamic relations of the system. In order to model nuclear matter in the outer core, we use relativistic mean field (RMF) theory models [56, 57, 58]. Ref. [58] provides an extensive study on RMFs.

RMFs model nucleon interactions by meson exchange. One can write down the Lagrangian of the theory and solve for the mean fields. In the following, IUF RMF [59] is used to illustrate.

The total Lagrangian consists of the nucleon contribution, the meson contribution, and the interactions among them.

$$\mathcal{L} = \mathcal{L}_N + \mathcal{L}_\sigma + \mathcal{L}_\omega + \mathcal{L}_\rho + \mathcal{L}_{\sigma\omega\rho} \tag{1.1}$$

$$\begin{aligned}
&= \bar{\psi}(i\gamma^\mu\partial_\mu - m_N)\psi + g_\sigma\bar{\psi}\sigma\psi - g_\omega\bar{\psi}\gamma^\mu\omega_\mu\psi - \frac{1}{2}g_\omega\bar{\psi}\gamma^\mu\vec{\rho}_\mu\vec{\tau}\psi \\
&+ \frac{1}{2}(\partial_\mu\sigma\partial^\mu\sigma - m_\sigma^2\sigma^2) - \frac{\kappa}{6}(g_\sigma\sigma)^3 - \frac{\lambda}{24}(g_\sigma\sigma)^4 \\
&- \frac{1}{4}(\partial_\mu\omega_\nu - \partial_\nu\omega_\mu)(\partial^\mu\omega^\nu - \partial^\nu\omega^\mu) + \frac{1}{2}m_\omega^2\omega_\mu\omega^\mu + \frac{\zeta}{24}g_\omega^4(\omega_\mu\omega^\mu)^2 \\
&- \frac{1}{4}(\partial_\mu\vec{\rho}_\nu - \partial_\nu\vec{\rho}_\mu - g_\rho(\vec{\rho}_\nu\times\vec{\rho}_\mu))(\partial^\mu\vec{\rho}^\nu - \partial^\nu\vec{\rho}^\mu - g_\rho(\vec{\rho}^\nu\times\vec{\rho}^\mu)) + \frac{1}{2}m_\rho^2\vec{\rho}_\mu\vec{\rho}^\mu \\
&+ \Lambda_\omega g_\rho^2\vec{\rho}_\mu\vec{\rho}^\mu g_\omega^2\omega_\mu\omega^\mu\,,
\end{aligned} \tag{1.2}$$

and the relevant parameters can be found in the reference [59].

Apply the Euler-Lagrangian equation to obtain the equation of motion for the mean

fields:

$$m_\sigma^2\sigma = g_\sigma n_s - \frac{\kappa}{2}g_\sigma^3\sigma^2 - \frac{\lambda}{6}g_\sigma^4\sigma^3\,, \tag{1.3}$$

$$m_\omega^2\omega_0 = g_\omega n_B - \frac{\zeta}{6}g_\omega^4\omega_0^3 - 2\Lambda_\omega g_\omega^2 g_\rho^2\rho_{03}^2\omega_0\,, \tag{1.4}$$

$$m_\rho^2\rho_{03} = \frac{g_\rho}{2}(n_p - n_n) - 2\Lambda_\omega g_\omega^2 g_\rho^2\rho_{03}\omega_0^2\,, \tag{1.5}$$

where the number density, energy density, entropy density, and the Fermi-Dirac distribution are [57]

$$n = 2\int\frac{d^3k}{(2\pi)^3}f_k\,, \tag{1.6}$$

$$\epsilon = 2\int\frac{d^3k}{(2\pi)^3}E_k f_k\,, \tag{1.7}$$

$$s = -2\int\frac{d^3k}{(2\pi)^3}[(1-f_k)ln(1-f_k) + f_k ln f_k]\,, \tag{1.8}$$

$$f_k = \frac{1}{1+\exp(E_k-\mu_k)/T}\,, \tag{1.9}$$

In order to solve for $\sigma, \omega, \rho, \mu_n, \mu_p, \mu_e$ of the system, we need to impose another 3 constraints, which are charge neutrality $n_p = n_e$, chemical equilibrium $\mu_n = \mu_p + \mu_e$ and definition of baryon number density $n_B = n_{B_n} + n_{B_p}$, where n_B is a number given from the input. Now we have 6 equations to solve for the 6 variables $(\sigma, \omega, \rho, \mu_n, \mu_p, \mu_e)$ with some proper initial guess for the mean fields and chemical potentials.

The effective masses are

$$m_N^* = m_N - g_\sigma\sigma\,, \tag{1.10}$$

the dispersion relations are

$$E_n = \sqrt{p^2 + m_n^{*2}} + g_\omega \omega_0 - \frac{1}{2} g_\rho \rho_{03} \,, \tag{1.11}$$

$$E_p = \sqrt{p^2 + m_p^{*2}} + g_\omega \omega_0 + \frac{1}{2} g_\rho \rho_{03} \,, \tag{1.12}$$

and the effective chemical potentials are

$$\mu_n^* = \mu_n - g_\omega \omega_0 + \frac{1}{2} g_\rho \rho_{03} \,, \tag{1.13}$$

$$\mu_p^* = \mu_p - g_\omega \omega_0 - \frac{1}{2} g_\rho \rho_{03} \,, \tag{1.14}$$

Now we treat nucleons as free quasi-particles, with their masses, energies, and chemical potentials being shifted by the mean fields. The sigma field contributes to the shift in mass. The omega field contributes to the shift in energy and chemical potential. The rho field contributes to the split between neutrons and protons, as well as energy and chemical potential. For more details, see [57].

Although the parameters are fit to nuclear properties around saturation density, it is important at higher densities the RMF produces enough pressure to counterbalance the gravitational force.

An RMF model produces an equation of state for neutron stars, which is related to the astrophysical observables through the Tolman-Oppenheimer-Volkov (TOV) equation [60, 61],

$$\frac{dP}{dr} = -\frac{G\varepsilon(r)m(r)}{r^2} \left[1 + \frac{P(r)}{\varepsilon(r)}\right] \left[1 + \frac{4\pi r^3 P(r)}{m(r)}\right] \left[1 - \frac{2Gm(r)}{r}\right]^{-1} \,, \tag{1.15}$$

$$\frac{dm}{dr} = 4\pi r^2 \epsilon(r) \,. \tag{1.16}$$

Given an equation of state, one can solve the TOV equation to obtain the mass-radius curve.

1.4 Urca Processes

Flavor equilibration dynamics (or isospin equilibration or proton fraction equilibration) is an important aspect of the whole neutron star merger dynamics. Flavor equilibration happens dominantly via Urca processes, which include direct Urca

$$\begin{aligned} n &\to p + e^- + \bar{\nu} \\ p + e^- &\to n + \nu \end{aligned} \tag{1.17}$$

and modified Urca

$$\begin{aligned} N + n &\to N + p + e^- + \bar{\nu} \\ N + p + e^- &\to N + n + \nu, \end{aligned} \tag{1.18}$$

where N is the spectator particle.

This thesis explores the neutrino-transparent regime where the temperature is below 10 MeV. Above 10 MeV, neutrinos are generally assumed to be trapped, and there are studies on the neutrino-trapped regime [62, 63, 64, 65]. At low temperatures, particles that participate in the reactions are close to their Fermi surfaces, or else they are exponentially suppressed. In order for the processes to happen, momentum needs to be conserved. However, there generally exists a threshold density, below which $k_{Fn} \geq k_{Fp} + k_{Fe}$ and direct Urca cannot happen. In this case, spectator nucleons participate and provide extra momenta, hence modified Urca happens instead.

The direct Urca neutron decay and electron capture rates, from Fermi's golden rule, are

[3]

$$\Gamma_{\rm nd} = \int \frac{d^3k_n}{(2\pi)^3}\frac{d^3k_p}{(2\pi)^3}\frac{d^3k_e}{(2\pi)^3}\frac{d^3k_\nu}{(2\pi)^3} f_n(1-f_p)(1-f_e) \\ \frac{\sum|M|^2}{(2E_n^*)(2E_p^*)(2E_e)(2E_\nu)}(2\pi)^4\delta^{(4)}(k_n-k_p-k_e-k_\nu)\,, \tag{1.19}$$

and

$$\Gamma_{\rm ec} = \int \frac{d^3k_n}{(2\pi)^3}\frac{d^3k_p}{(2\pi)^3}\frac{d^3k_e}{(2\pi)^3}\frac{d^3k_\nu}{(2\pi)^3}(1-f_n) f_p f_e \\ \frac{\sum|M|^2}{(2E_n^*)(2E_p^*)(2E_e)(2E_\nu)}(2\pi)^4\delta^{(4)}(k_p+k_e-k_n-k_\nu)\,, \tag{1.20}$$

where $\Sigma|M|$ is the spin-summed matrix element, $E_i^* = \sqrt{k_i^2 + m_i^{*2}}$ are the effective nucleon dispersion relations, $E_e = \sqrt{k_e^2 + m_e^2}$ and $E_\nu = k_\nu$ are the electron/neutrino dispersion relations, and f_i are Fermi-Dirac distributions.

The modified Urca neutron decay and electron capture rates are,

$$\Gamma_{mU,nd} = \int \frac{d^3k_n}{(2\pi)^3}\frac{d^3k_p}{(2\pi)^3}\frac{d^3k_e}{(2\pi)^3}\frac{d^3k_\nu}{(2\pi)^3}\frac{d^3k_{N_1}}{(2\pi)^3}\frac{d^3k_{N_2}}{(2\pi)^3}\,(2\pi)^4\delta^{(4)}(k_n+k_{N_1}-k_p-k_e-k_\nu-k_{N_2}) \\ f_n f_{N_1}(1-f_p)(1-f_e)(1-f_{N_2})\Big(s\frac{\sum|M|^2}{2^6E_n^*E_p^*E_eE_\nu E_{N_1}^*E_{N_2}^*}\Big), \tag{1.21}$$

$$\Gamma_{mU,ec} = \int \frac{d^3k_n}{(2\pi)^3}\frac{d^3k_p}{(2\pi)^3}\frac{d^3k_e}{(2\pi)^3}\frac{d^3k_\nu}{(2\pi)^3}\frac{d^3k_{N_1}}{(2\pi)^3}\frac{d^3k_{N_2}}{(2\pi)^3}\,(2\pi)^4\delta^{(4)}(k_p+k_e+k_{N_1}-k_n-k_\nu-k_{N_2}) \\ f_p f_e f_{N_1}(1-f_n)(1-f_{N_2})\Big(s\frac{\sum|M|^2}{2^6E_n^*E_p^*E_eE_\nu E_{N_1}^*E_{N_2}^*}\Big)\,, \tag{1.22}$$

where $\Sigma|M|$ is the spin-summed matrix element for modified Urca processes.

The physics of flavor equilibration and details of the calculations are discussed in Chap. 2

and Chap. 3.

1.5 the MUSES Framework

MUSES (Modular Unified Solver of Equation of States) is an open-source cyberinfrastructure that provides novel tools to study gravitational wave astrophysics, nuclear physics, and heavy-ion physics. The MUSES official website is `https://musesframework.io/` and all the source codes are in the following GitLab repo `https://gitlab.com/nsf-muses`.

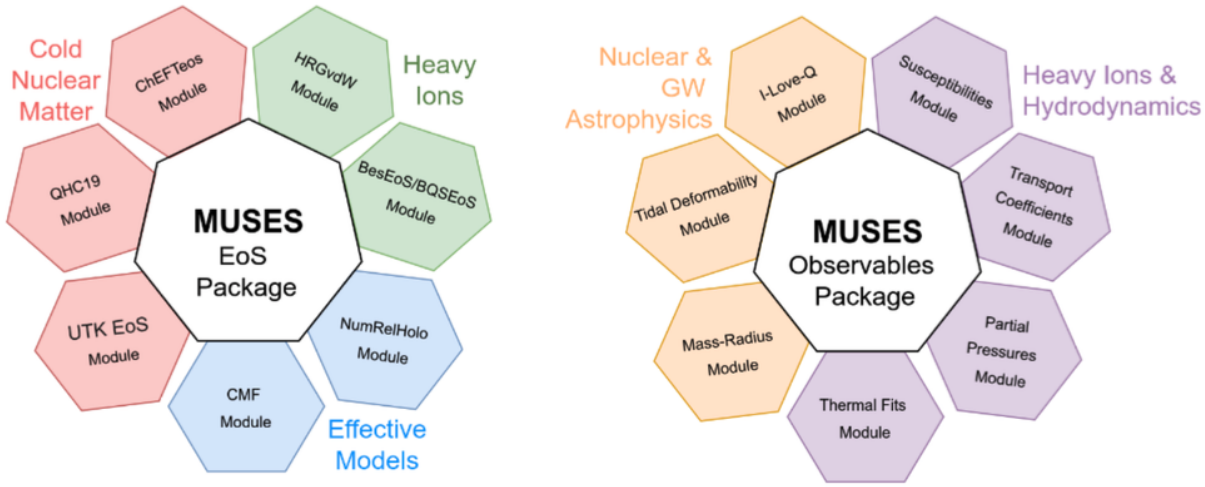

Fig. 1.2: Proposed MUSES modules. Produced by the MUSES collaboration.

The MUSES collaboration has been expanding since its initiation. Currently, its physics mainly consists of two parts, as shown in Fig. 1.2. The EoS Modules include effective modules such as CMF [15], heavy ion EoSes such as BQS [12, 66], cold nuclear EoSes such as χEFT [17], UTK [16]. The Observable/Users Modules include flavor equilibration module [67, 68] which provides calculations for Urca rates and flavor equilibration information, QLIMR module which provides calculations for mass-radius, I-Love-Q universal relation and tidal deformability information. More groups are joining and in their development stages.

The MUSES is aiming at covering most parts of the QCD phase diagram. The EoS package will ultimately combine and merge all EoS modules into a smooth, unified EoS, as the collaboration name suggests.

In terms of technology, MUSES is different from other platforms such as ComPOSE. MUSES will use more modern tools such as Docker container technology for each module and build a scalable deployment system that can work across different environments. MUSES will also provide an interactive interface for its calculation engine and workflow management to users.

For more details about MUSES and the flavor equilibration module, see Chap. 5.

1.6 Outline of the Thesis

The thesis is outlined as follows.

In chapter 2, we develop the state-of-the-art calculation for direct Urca processes in the neutrino-transparent regime. We use a fully consistent description of nucleons, and full matrix elements and perform 5-dim full phase-space numerical integral. Based on the rate calculation, we correct the cold beta-equilibrium as a result of neutrino leaving the system. The correction to the equilibrium condition can reach 20 MeV, which can lead to wrong Urca rates if neglected.

In chapter 3, based on the state-of-the-art rate calculation and the correction to the cold beta-equilibrium developed in chapter 2, we analyze the isospin ("beta") equilibration properties of neutrino-transparent nuclear (npe) matter in the temperature and density range that is relevant to neutron star merger. We find that the isospin relaxation rate rises rapidly as the temperature rises, and at T $\approx$ 5 MeV, it is comparable to the timescale of the density oscillations that occur immediately after the merger. This produces a resonant peak in the

bulk viscosity at T $\approx$ 5 MeV, which causes density oscillations to be damped on the timescale of the merger. We conclude that there is good reason to include isospin relaxation dynamics in merger simulations.

In chapter 4, the improvement of modified Urca calculation [4] over the traditional crude modified Urca calculation encounters an unphysical divergence issue around the threshold. First, we successfully solved the divergence issue by adding a width to the internal particle propagator. Then, we take further steps to build a unified framework of Urca processes from a neutrino self-energy diagram. This approach combines Urca processes into one calculation and easily allows going beyond Fermi surface approximations. Besides, a modified Urca rate calculation based on full 11-dim phase-space integrals and relativistic treatment of the nucleons has been presented.

In chapter 5, an introduction to the MUSES framework and the flavor equilibration module is provided. All physics and calculations discussed in chapter 2 and chapter 3 are implemented in the flavor equilibration module. Besides, in order to improve the interpolation schemes used in MUSES, we explore the performance of Gaussian process interpolations, which is a Bayesian regression framework. It is shown that the GP interpolator better interpolates the equation of state tables compared to the linear interpolator.

Chapter 2

Urca Processes and Beta Equilibrium

We develop the state-of-the-art calculation for direct Urca processes in the neutrino-transparent regime. We use a fully consistent description of nucleons and perform 5-dim full phase-space numerical integral. Based on the rate calculation, we correct the beta-equilibrium condition in the temperature range $1\,\mathrm{MeV} \leq T \leq 5\,\mathrm{MeV}$ as a consequence of neutrino leaving the system. The correction to the equilibrium condition can reach 20 MeV, which can lead to wrong Urca rates if neglected.

2.1 Introduction

Nuclear matter in neutron stars settles into beta equilibrium, meaning that the proton fraction is in equilibrium with respect to the weak interactions. In this paper we will study the conditions for beta equilibrium in ordinary nuclear matter (where all the baryon number is contributed by neutrons (n) and protons (p)) in the temperature range $1\,\mathrm{MeV} \lesssim T \lesssim 5\,\mathrm{MeV}$. This regime, which arises in neutron star mergers [69, 70, 71, 72], is cool enough so that neutrinos are not trapped, but warm enough so that there are corrections to the low-temperature equilibrium condition. It has previously been shown [73] that in this regime the

full beta equilibrium condition is

$$\mu_n = \mu_p + \mu_e + \Delta\mu \ , \tag{2.1}$$

where $\Delta\mu$ is a correction that arises from the violation of detailed balance (neutrino transparency) and the breakdown of the Fermi surface approximation (see Sec. 2.2). In nuclear matter in the temperature regime discussed here, the proton fraction will equilibrate towards the value given by Eq. (2.1). Even if equilibrium is not reached on the timescale of a merger, one needs to know the correct equilibration condition in order to analyze phenomena associated with this relaxation process, such as bulk viscosity and neutrino emission. At low temperatures ($T \ll 1\,\mathrm{MeV}$) $\Delta\mu$ is negligible, but in the temperature regime under consideration here it has been estimated to be up to tens of MeV [73]. The calculation in Ref. [73] went beyond the Fermi-surface approximation by performing the phase space integral for the equilibration rate over the entire momentum space. However, it used a very crude model of the in-medium nucleons, assigning them their vacuum mass and assuming that their kinematics remained nonrelativistic at all densities.

In this paper we improve on the analysis of Ref. [73]. We treat nuclear matter consistently using relativistic mean field models [56, 58] with fully relativistic dispersion relations for the nucleons. We show that this makes a considerable difference to the beta equilibration rates because in these models the nucleons at the Fermi surface become relativistic at densities of a few times nuclear saturation density n_0. We calculate the direct Urca rate using the entire weak-interaction matrix element rather than its non-relativistic limit, and evaluate the full phase space integral.

Other authors have evaluated direct Urca phase space integrals in calculations of the direct Urca rate, the neutrino emissivity, or the neutrino mean free path. Fully relativistic

computations of direct Urca phase space integrals are uncommon in the literature, but they do appear. Refs. [74, 75, 76, 77] calculate the neutrino mean free path using a fully relativistic formalism, while integrating over the full phase space. Ref. [76] calculates the direct Urca electron capture rate using a fully relativistic formalism and performs the full phase space integration. While these calculations perform the full integration over phase space, they focus on high temperatures ($T \gtrsim 5$ MeV) where neutrinos are trapped and where the direct Urca threshold is blurred over a wide density range. In this temperature regime, which can be reached in mergers as well [69, 78, 79, 80], beta equilibrium is given by

$$\mu_n + \mu_\nu = \mu_p + \mu_e \,, \tag{2.2}$$

with μ_ν being the neutrino chemical potential. As discussed in more detail in Sec. 2.2, the neutrino trapped beta equilibration condition does not require an additional finite temperature correction. This paper will examine the phase space integral at lower temperatures where the direct Urca threshold is apparent and a key feature in the physics of beta equilibration or neutrino emission.

Other works use the relativistic formalism, but assume the nuclear matter is strongly degenerate (using the Fermi surface approximation, described below), and thus their results have a sharp direct Urca threshold density [81, 82, 83]. Ref. [84] uses the Fermi surface approximation, but develops a way to incorporate the finite 3-momentum of the neutrino, slightly blurring the threshold at nonzero temperature. Some works do the full phase space integration, but use nonrelativistic approximations for the matrix element and nucleon dispersion relations [63, 62, 73, 85]. The vast majority of calculations use non-relativistic approximations of the matrix element and the nucleon dispersion relations, together with the Fermi surface approximation [86, 87, 88, 89, 90, 91, 92, 93, 94, 3, 95, 96, 97]. All of

these calculations are approximations of the full phase space integration using the fully relativistic formalism. Under certain conditions, the approximations match well with the full calculation, and have the advantage of being simple.

In Sec. 2.3 we introduce the two relativistic mean field models, IUF and SFHo, that we use. Sec. 2.4 describes our calculation of the rate of direct Urca processes, where we integrate over the entire phase space in order to include contributions from the region that would be kinematically forbidden in the low temperature limit. Sec. 2.5 describes our calculation of the modified Urca contribution to the rate, where we use the Fermi surface approximation since there is no kinematically forbidden region for those processes in the density range that we consider. Sec. 2.6 presents our results, and Sec. 2.7 provides our conclusions.

We work in natural units, where $\hbar = c = k_B = 1$.

2.2 Beta equilibration

Beta equilibration in npe^- matter is established by the Urca processes [61]. The modified Urca processes

$$\begin{aligned} N + n &\to N + p + e^- + \bar{\nu} \\ N + p + e^- &\to N + n + \nu, \end{aligned} \tag{2.3}$$

(here, N represents a "spectator" neutron or proton) operate at all densities in the core of the neutron star[1]. The direct Urca processes

$$n \to p + e^- + \bar{\nu} \qquad (2.4)$$
$$p + e^- \to n + \nu$$

are exponentially suppressed when the temperature is much less than the Fermi energies and the density is in the range where $k_{Fn} > k_{Fp} + k_{Fe}$. In nuclear matter, the proton fraction rises as the density rises above n_0 and eventually may reach a "direct Urca threshold" where $k_{Fn} = k_{Fp} + k_{Fe}$. Above this threshold density beta equilibration is dominated by direct Urca, since (when kinematically allowed) it is faster than modified Urca.

In nuclear matter at temperatures greater than, say, 10 MeV, the neutrino mean free path is short and the nuclear matter system (for example, a protoneutron star) is neutrino-trapped and has conserved lepton number $Y_L = (n_e + n_\nu)/n_B$. In this case, the Urca processes (3.25) and (3.24) can proceed forward and backward, as the nuclear matter contains a population of neutrinos (or antineutrinos). In beta equilibrum, the forward and reverse processes have equal rates (detailed balance) and the beta equilibrium condition is given by balancing the chemical potentials of the participants in the equlibration reactions [99, 56]

$$\mu_n + \mu_\nu = \mu_p + \mu_e \qquad (\nu\text{-trapped}) \qquad (2.5)$$

In cooler nuclear matter, at the temperatures considered in this work, the neutrino mean free path is comparable to or longer than the system size and therefore neutrinos are not

[1] In npe^- matter, the proton-spectator modified Urca process operates at densities where $x_p > 1/65$ [3, 89]. However, this condition is only violated (if ever) in the inner crust of neutron stars [98] where the matter is not uniform and thus the calculations in this paper would not apply.

in thermodynamic equilibrium: they escape from the star. Neutrinos can then occur in the final state but not the initial state of the Urca processes. Beta equilibrium is still achieved, but now by a balance of the neutron decay and the electron capture processes. However, the principle of detailed balance is not applicable because electron capture is not the time-reverse of neutron decay. There is then no obvious equilibrium condition that can be written down a priori.

In the limit of low temperature ($T \ll 1\,\mathrm{MeV}$) the Fermi surface approximation becomes valid: the particles participating in the Urca processes are close to their Fermi surfaces, and the neutrino carries negligible energy $\sim T$. The beta equilibrium condition can then be obtained by neglecting the neutrino, so that neutron decay and electron capture are just different time orderings of the same process $n \leftrightarrow p\ e^-$, and detailed balance gives[2]

$$\mu_n = \mu_p + \mu_e \qquad \text{(low temperature, } \nu\text{-transparent)}. \tag{2.6}$$

At temperatures $T \gtrsim 1\,\mathrm{MeV}$ corrections to the Fermi surface approximation start to become significant, particularly for the protons whose Fermi energy is in the 10 MeV range. Then one cannot neglect the nonzero-temperature correction to (2.6)

$$\mu_n = \mu_p + \mu_e + \Delta\mu, \quad \text{(general, } \nu\text{-transparent)} \tag{2.7}$$

The correction $\Delta\mu$ is a function of density and temperature, and its value in beta equilibrium is found by explicitly calculating the neutron decay and electron capture rates and adjusting $\Delta\mu$ so that they balance [73] (see also [101], where a similar calculation was done in the

[2] The same condition on the chemical potentials can be reached by examining the phase space integrals for the direct Urca neutron decay and electron capture rates, taking the limit where the neutrino energy and momentum go to zero [100].

context of a hot plasma). In this paper we perform that calculation.

For weak interactions we use the Fermi effective theory, which is an excellent approximation at nuclear energy scales. The main approximations arise in our treatment of the strong interaction. To describe nuclear matter and the nucleon excitations we use two different relativistic mean field models, both consistent with known phenomenology and chosen to illustrate a plausible range of behaviors. We describe these models in Sec. 2.3. For the modified Urca process we model the nucleon-nucleon interaction with one-pion exchange [2, 3].

2.3 Nuclear matter models

We will use two different equations of state, IUF [59] and SFHo [5], to calculate the Urca rates and the nonzero-temperature correction $\Delta\mu$. These are both consistent at the 2σ level with observational constraints on the maximum mass and the radius of neutron stars.

IUF predicts a maximum mass of neutron star to be $1.95 M_\odot$, and SFHo predicts $2.06 M_\odot$. Both are consistent with the observed limits, which are:

- $M_{\rm max} > 2.072^{+0.067}_{-0.066}\, M_\odot$ from NICER and XMM analysis of PSR J0740+6620 [39],
- $M_{\rm max} = 1.928^{+0.017}_{-0.017}\, M_\odot$ from NANOGrav analysis of PSR J1614-2230 [102],
- $M_{\rm max} = 2.01^{+0.14}_{-0.14}\, M_\odot$ from pulsar timing analysis of PSR J0348+0432 [103].

For the radius of a star of mass $2.06\, M_\odot$, SFHo predicts $R = 10.3\,$km, consistent with $R = 12.39^{+1.30}_{-0.98}\,$km from NICER and XMM analysis of PSR J0740+6620 [39]. For the radius of a $1.4\, M_\odot$ neutron star, IUF predicts $R = 12.7\,$km and SFHo predicts $R = 11.9\,$km, consistent with $R = 11.94^{+0.76}_{-0.87}\,$km obtained by a combined analysis of X-ray and gravitational wave measurements of PSR J0740+6620 in Ref. [104]. Both models reproduce properties of nuclear

matter around saturation within known experimental constraints. Although both models predict a slightly different value for the saturation density n_0, we will use $n_0 = 0.16\,\mathrm{fm}^{-3}$ in all our plots.

It is still not determined whether there is a direct Urca threshold or not in nuclear matter at neutron star densities [105, 106, 107, 108, 109], so we choose one equation of state (IUF) with a threshold slightly above $4\,n_0$ and one (SFHo) with no threshold, as shown in Fig. 2.1. Our approach could be applied to any equation of state where the beta process rates can be calculated. As we will see in Sec. 2.6.3, the density dependence of the momentum surplus $k_{Fp} + k_{Fe} - k_{Fn}$ is an important factor in the behavior of the direct Urca rates at low temperature, but the density dependence of the nucleon effective masses and Fermi momenta has a noticeable impact as well.

The coupling constants for SFHo are shown in Appendix A. Notice that the constants are taken from the online CompOSE database (`https://compose.obspm.fr/`), and are different from the values provided in Ref. [5].

A key feature of our calculation is that we use the full relativistic dispersion relations for the nucleons. In Figs. 2.2 and 2.3 we illustrate the importance of this in relativistic mean field theories, where the nucleon effective mass drops rapidly with density[3]. We plot the Dirac effective mass [114] and the Fermi momentum of the neutrons and protons in these two EoSs. While around nuclear saturation density n_0, the nucleons are nonrelativistic, as the density rises to several times n_0, the nucleon effective mass has dropped significantly below its vacuum value. Neutrons on their Fermi surface become relativistic at $2-3n_0$, while protons on their Fermi surface remain nonrelativistic until the density rises to $3-6n_0$. In Figs. 2.13 and 2.14, we show that using a non-relativistic approximation would lead to Urca

[3] While the precipitous drop in the nucleon Dirac effective mass with increasing density is a common feature in relativistic mean field theories [110, 111], we note that in two recent treatments that go beyond the mean field approximation, the drop in the effective mass was not as dramatic [112, 113].

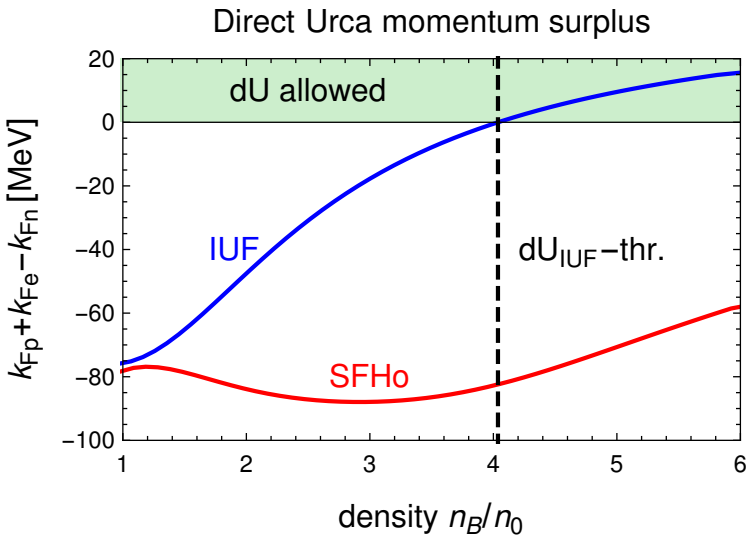

Fig. 2.1: Direct Urca momentum surplus $k_{Fp} + k_{Fe} - k_{Fn}$ for IUF and SFHo equations of state at $T = 0$. When the surplus is negative, direct Urca is forbidden. IUF has an upper density threshold above which direct Urca is allowed; SFHo does not.

rates that are incorrect by about an order of magnitude, although for direct Urca neutron decay the discrepancy can be many orders of magnitude.

2.4 Beta equilibration via direct Urca

We calculate the in-medium direct Urca rates for neutron decay and electron capture using the relativistic weak-interaction matrix element and the relativistic dispersion relations for the nucleons and electrons. We also integrate over the full momentum phase space, not relying on the Fermi surface approximation. This is important because in the "dUrca-forbidden" density range the Fermi surface approximation would say the direct Urca rate is zero, so nonzero-temperature corrections are the leading contribution. These become significant (comparable to modified Urca) at the temperatures of interest here, $T \gtrsim 1\,\mathrm{MeV}$ [73].

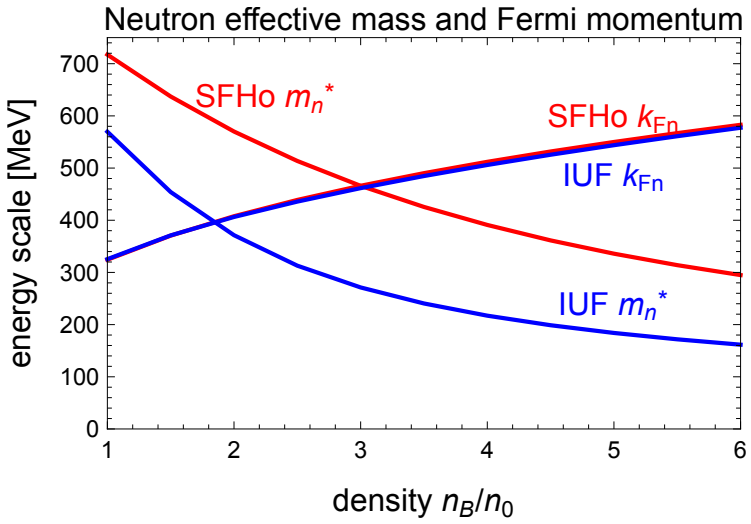

Fig. 2.2: Density dependence of the neutron's (Dirac) effective mass and Fermi momentum for the IUF and SFHo EoSs, showing that neutrons at the Fermi surface become relativistic at densities above 2 to $3\,n_0$.

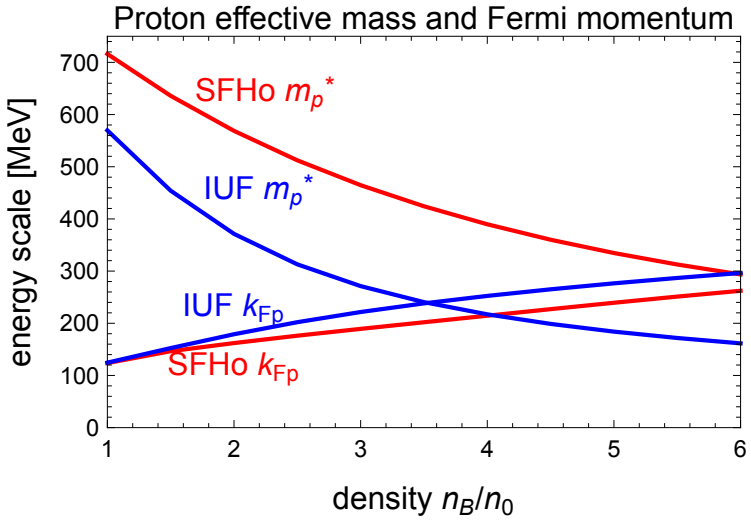

Fig. 2.3: Density dependence of the proton's (Dirac) effective mass and Fermi momentum for the IUF and SFHo EoSs, showing that protons at the Fermi surface become relativistic starting at densities between $3-6n_0$.

In relativistic mean field models the dispersion relations for the neutrons, protons, and electrons are

$$\begin{aligned} E_n &= \underbrace{\sqrt{m_n^{*\,2} + k_n^2}}_{E_n^*} + U_n \\ E_p &= \underbrace{\sqrt{m_p^{*\,2} + k_p^2}}_{E_p^*} + U_p \\ E_e &= \sqrt{m_e^2 + k_e^2} \\ E_\nu &= k_\nu \end{aligned} \tag{2.8}$$

where the nucleons' effective mass m_i^* and energy shift U_i depend on density and temperature [76]. The unshifted energies E_i^* arise in the phase space normalization and the Dirac traces [75].

2.4.1 Neutron decay

The direct Urca neutron decay rate is [3, 115]

$$\begin{aligned} \Gamma_{\rm nd} = \int \frac{d^3k_n}{(2\pi)^3}\frac{d^3k_p}{(2\pi)^3}\frac{d^3k_e}{(2\pi)^3}\frac{d^3k_\nu}{(2\pi)^3} \\ f_n(1-f_p)(1-f_e)\frac{\sum |M|^2}{(2E_n^*)(2E_p^*)(2E_e)(2E_\nu)} \\ (2\pi)^4\delta^{(4)}(k_n - k_p - k_e - k_\nu)\ . \end{aligned} \tag{2.9}$$

For a more detailed explanation of this expression and its evaluation, see Appendix B. As described there, it can be reduced to 5-dimensional momentum integral (B.34)

$$\Gamma_{\rm nd} = \frac{G^2}{16\pi^6}\int_0^\infty dk_n \int_0^{k_p^{\rm max}} dk_p \int_0^{k_e^{\rm max}} dk_e \\ k_n^2 k_p^2 k_e^2 f_n(1-f_p)(1-f_e)\,\Theta(E_\nu) \\ \int_{z_p^{\rm min}}^{z_p^{\rm max}} dz_p \int_{z_e^-}^{z_e^+} dz_e \frac{4E_\nu \mathcal{M}_{\phi_0}}{\sqrt{S^2-(E_\nu^2-R)^2}}\ , \tag{2.10}$$

where R, S, and $\mathcal{M}_{\phi_0}$ are defined in Eqs. (B.15), (B.16), and (B.17). The antineutrino energy E_ν is given by

$$E_\nu = E_n - E_p - E_e, \tag{2.11}$$

which becomes a function of the remaining integration variables, k_n, k_p, and k_e. Note that there are Fermi-Dirac distributions for the neutrons, proton vacancies, and electron vacancies, but none for the neutrinos because we work in the neutrino-transparent regime where neutrinos escape from the star and do not form a Fermi gas. We evaluate this integral numerically using a Monte-Carlo algorithm.

2.4.2 Electron capture

The expression for the electron capture rate can be obtained from that for neutron decay (B.1) by making the following changes: (1) the energy-momentum delta function now corresponds the the process $p\ e^- \to n\ \nu$, and (2) there are Fermi-Dirac distributions for proton

and electron particles, and neutron vacancies,

$$\Gamma_{\rm ec} = \int \frac{d^3k_n}{(2\pi)^3}\frac{d^3k_p}{(2\pi)^3}\frac{d^3k_e}{(2\pi)^3}\frac{d^3k_\nu}{(2\pi)^3} \\ (1-f_n)f_p f_e \,\frac{\sum |M|^2}{(2E_n^*)(2E_p^*)(2E_e)(2E_\nu)} \\ (2\pi)^4\delta^{(4)}(k_p + k_e - k_n - k_\nu)\ . \tag{2.12}$$

Evaluating this expression takes us through the same steps as for neutron decay, except that the neutrino energy is now

$$E_\nu = E_p + E_e - E_n\ , \tag{2.13}$$

and the requirement that this be positive leads to different limits on the momentum integrals,

$$\Gamma_{\rm ec} = \frac{G^2}{16\pi^6}\int_0^\infty dk_n \int_0^\infty dk_p \int_0^\infty dk_e \\ k_n^2 k_p^2 k_e^2 f_n(1-f_p)(1-f_e)\Theta(E_\nu) \\ \int_{z_p^{\rm min}}^{z_p^{\rm max}} dz_p \int_{z_e^-}^{z_e^+} dz_e \frac{4E_\nu \mathcal{M}_{\phi_0}}{\sqrt{S^2-(E_\nu^2-R)^2}}\ . \tag{2.14}$$

2.5 Beta equilibration via modified Urca

We calculate the rate of the modified Urca processes (3.25) using the relativistic dispersion relations of the nucleons in the phase space integration, but unlike the direct Urca rate we do not perform the phase space integration exactly, which would be difficult because the involvement of the spectator particles would lead to an 11-dimensional numerical integral over momentum. Instead we use the Fermi Surface approximation. This is reasonable for modified

Urca as long as the Fermi surfaces are not too thermally blurred, i.e. when the temperature is below the lowest Fermi kinetic energy, which is that of the proton. The modified Urca processes do not have a density threshold in the range of densities we consider here (see footnote 1), so the Fermi surface approximation never predicts a vanishing rate. In this work we explore the temperature range $1\,\mathrm{MeV} < T < 5\,\mathrm{MeV}$, and the proton's Fermi kinetic energy is at least 10 MeV in the density range $n > n_0$, so the Fermi surface approximation is justified for modified Urca rates. The first paragraph of Sec. 2.4 contains a discussion of why we need to go beyond the Fermi surface approximation in our direct Urca rate calculations. For the matrix elements that arise in modified Urca (C.1) and (C.16), we use the standard results (see, e.g., [3]), which were calculated assuming non-relativistic nucleons. It has been pointed out [4] that the standard calculation of the modified Urca matrix element [2], which we use here, is based on a very crude approximation for the propagator of the internal off-shell nucleon. A more accurate treatment would lead to different modified Urca rates and shift our predicted values of $\Delta\mu$; we defer such a calculation to future work.

2.5.1 Neutron Decay

Modified Urca can proceed with either a neutron spectator or a proton spectator. From Fermi's Golden rule, we have the rate for the neutron decay process

$$\begin{aligned}\Gamma_{mU,nd} = \int & \frac{d^3k_n}{(2\pi)^3}\frac{d^3k_p}{(2\pi)^3}\frac{d^3k_e}{(2\pi)^3}\frac{d^3k_\nu}{(2\pi)^3}\frac{d^3k_{N_1}}{(2\pi)^3}\frac{d^3k_{N_2}}{(2\pi)^3} \\ & (2\pi)^4\delta^{(4)}(k_n + k_{N_1} - k_p - k_e - k_\nu - k_{N_2}) \\ & f_n f_{N_1}(1-f_p)(1-f_e)(1-f_{N_2}) \\ & \Big(s\frac{\sum|M|^2}{2^6 E_n^* E_p^* E_e E_\nu E_{N_1}^* E_{N_2}^*}\Big). \end{aligned} \tag{2.15}$$

Here, $s = 1/2$ because of the identical particles appearing in the process. N_1 and N_2 are neutrons in the n-spectator process and for the p-spectator neutron decay process, N_1 and N_2 are protons. The matrix element is different for each process (see Eqs. C.1 and C.16). The detailed derivation of the modified Urca rates is in Appendix C. For n-spectator neutron decay, allowing the system to deviate from the low-temperature beta equilibrium condition (2.6) by amount

$$\xi = \frac{\mu_n - \mu_p - \mu_e}{T}, \tag{2.16}$$

we obtain

$$\begin{aligned}\Gamma_{mU,nd(n)}(\xi) = \frac{7}{64\pi^9} G^2 g_A^2 f^4 \frac{(E^*_{Fn})^3 E^*_{Fp}}{m_\pi^4} \\ \frac{k^4_{Fn} k_{Fp}}{(k^2_{Fn} + m^2_\pi)^2} F(\xi) T^7 \theta_n \,,\end{aligned} \tag{2.17}$$

where $f \approx 1$ is the N-π coupling [3],

$$\begin{aligned}F(\xi) \equiv &- (\xi^4 + 10\pi^2\xi^2 + 9\pi^4)\mathrm{Li}_3(-e^\xi) + 12(\xi^3 + 5\pi^2\xi) \\ &\mathrm{Li}_4(-e^\xi) - 24(3\xi^2 + 5\pi^2)\mathrm{Li}_5(-e^\xi) \\ &+ 240\xi\mathrm{Li}_6(-e^\xi) - 360\mathrm{Li}_7(-e^\xi)\,,\end{aligned} \tag{2.18}$$

and

$$\theta_n \equiv \begin{cases} 1 & k_{Fn} > k_{Fp} + k_{Fe} \\ 1 - \dfrac{3}{8}\dfrac{(k_{Fp} + k_{Fe} - k_{Fn})^2}{k_{Fp} k_{Fe}} & k_{Fn} < k_{Fp} + k_{Fe}\,. \end{cases} \tag{2.19}$$

The functions $\mathrm{Li}_n(x)$ are polylogarithms of order n [116]. For p-spectator neutron decay, we obtain

$$\Gamma_{mU,nd(p)}(\xi) = \frac{1}{64\pi^9} G^2 g_A^2 f^4 \frac{(E^*_{Fp})^3 E^*_{Fn}}{m_\pi^4} \frac{(k_{Fn}-k_{Fp})^4 k_{Fn}}{((k_{Fn}-k_{Fp})^2+m_\pi^2)^2} F(\xi) T^7 \theta_p \,, \tag{2.20}$$

where

$$\theta_p \equiv \begin{cases} 0 & \text{if } k_{Fn} > 3k_{Fp} + k_{Fe} \\ \dfrac{(3k_{Fp}+k_{Fe}-k_{Fn})^2}{k_{Fn}k_{Fe}} & \text{if } \begin{array}{l} k_{Fn} > 3k_{Fp} - k_{Fe} \\ k_{Fn} < 3k_{Fp} + k_{Fe} \end{array} \\ 4\dfrac{3k_{Fp}-k_{Fn}}{k_{Fn}} & \text{if } \begin{array}{l} 3k_{Fp} - k_{Fe} > k_{Fn} \\ k_{Fn} > k_{Fp} + k_{Fe} \end{array} \\ \left(2 + 3\dfrac{2k_{Fp}-k_{Fn}}{k_{Fe}} - 3\dfrac{(k_{Fp}-k_{Fe})^2}{k_{Fn}k_{Fe}}\right) & \text{if } k_{Fn} < k_{Fp} + k_{Fe} \,. \end{cases} \tag{2.21}$$

2.5.2 Electron Capture

The electron capture modified Urca rate can be obtained in a similar way to neutron decay, by changing the sign of the neutrino 4-momentum in the energy-momentum delta function

and interchanging the particle and hole Fermi-Dirac factors,

$$\begin{aligned}\Gamma_{mU,ec} = \int & \frac{d^3k_n}{(2\pi)^3}\frac{d^3k_p}{(2\pi)^3}\frac{d^3k_e}{(2\pi)^3}\frac{d^3k_\nu}{(2\pi)^3}\frac{d^3k_{N_1}}{(2\pi)^3}\frac{d^3k_{N_2}}{(2\pi)^3} \\ & (2\pi)^4\delta^{(4)}(k_p + k_e + k_{N_1} - k_n - k_\nu - k_{N_2}) \\ & f_p f_e f_{N_1}(1-f_n)(1-f_{N_2}) \\ & \left(s\frac{\sum|M|^2}{2^6 E_n^* E_p^* E_e E_\nu E_{N_1}^* E_{N_2}^*}\right). \end{aligned} \tag{2.22}$$

Through a similar calculation, we find that the modified Urca neutron decay and electron capture rates in the Fermi surface approximation are related by

$$\Gamma_{mU,ec(n)}(\xi) = \Gamma_{mU,nd(n)}(-\xi)\,, \tag{2.23}$$

and

$$\Gamma_{mU,ec(p)}(\xi) = \Gamma_{mU,nd(p)}(-\xi)\,. \tag{2.24}$$

2.6 Results

2.6.1 Beta equilibrium at nonzero temperature

Figs. 2.4 and 2.5 show our final results for the nonzero-temperature correction $\Delta\mu$ required to achieve beta equilibrium, for the IUF and SFHo equations of state respectively. The key features are

- At low temperatures $T \lesssim 1\,\mathrm{MeV}$, the Fermi Surface approximation is valid and beta equilibrium is achieved with a negligible correction $\Delta\mu$ (see Sec. 2.2).

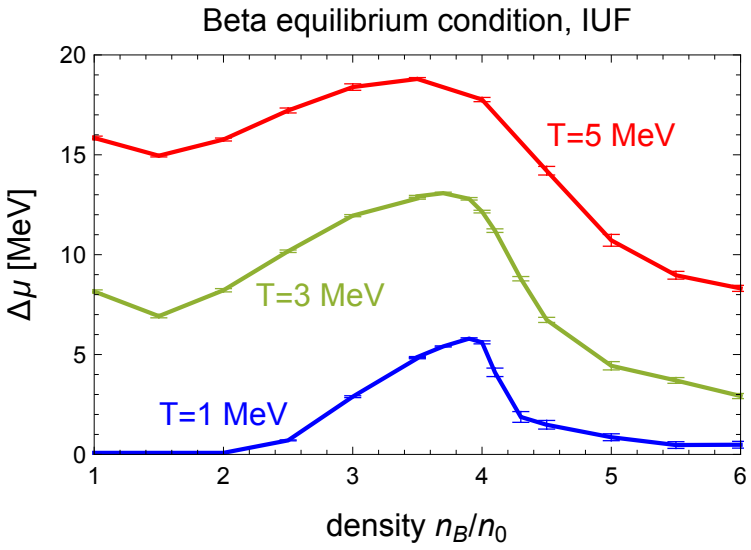

Fig. 2.4: Nonzero-temperature correction $\Delta\mu$ required for beta equilibrium (Eq. 2.7) with the IUF EoS.

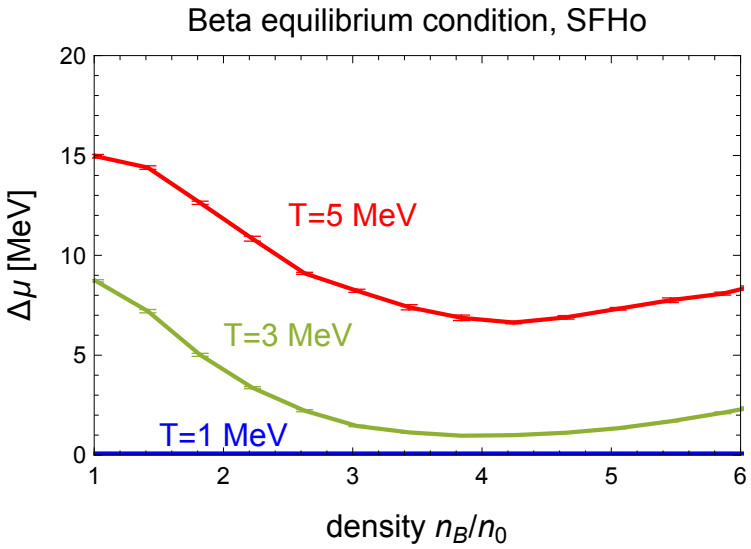

Fig. 2.5: Nonzero-temperature correction $\Delta\mu$ required for beta equilibrium (Eq. 2.7) with the SFHo EoS.

- As the temperature rises through the neutrino-transparent regime, the value of $\Delta\mu$ rises.
- We only provide results for temperatures up to 5 MeV because at temperatures of around 5 to 10 MeV the neutrino mean free path will become smaller than the star, invalidating our assumption of neutrino transparency.
- The figures indicate that the nonzero-temperature correction reaches values of 10 to 20 MeV before neutrino trapping sets in.
- The density dependence of $\Delta\mu$ appears very different for different EoSs. For IUF the largest values are reached at moderate densities, near the direct Urca threshold. For SFHo, $\Delta\mu$ has a minimum at those densities.

In the rest of this section we will explain these features of our results.

The temperature dependence follows from the breakdown of the Fermi surface approximation. At $T \lesssim 1\,\mathrm{MeV}$ the Urca processes are dominated by modes close to the Fermi surfaces of the neutron, protons, and electrons. The energy of the emitted neutrino is of order T which is negligible, so the direct Urca process is effectively $n \leftrightarrow p\ e^-$, for which the equilibrium condition is $\mu_n = \mu_p + \mu_e$, i.e. $\Delta\mu = 0$. As the temperature approaches the Fermi energy of the protons, the Fermi surface approximation breaks down. Modes far from the proton and electron Fermi surfaces begin to play a role, and the energy of the emitted neutrino becomes important. The processes that establish beta equilibrium, $n \to p\ e^-\ \bar{\nu}_e$ and $p\ e^- \to n\ \nu_e$, are not related by time reversal, so the principle of detailed balance does not apply. This means that even below the direct Urca threshold density, direct Urca processes can be fast enough and sufficiently different in their rates to require a correction $\Delta\mu$ to bring them into balance. As we will explain below, at $\Delta\mu = 0$ electron capture is much

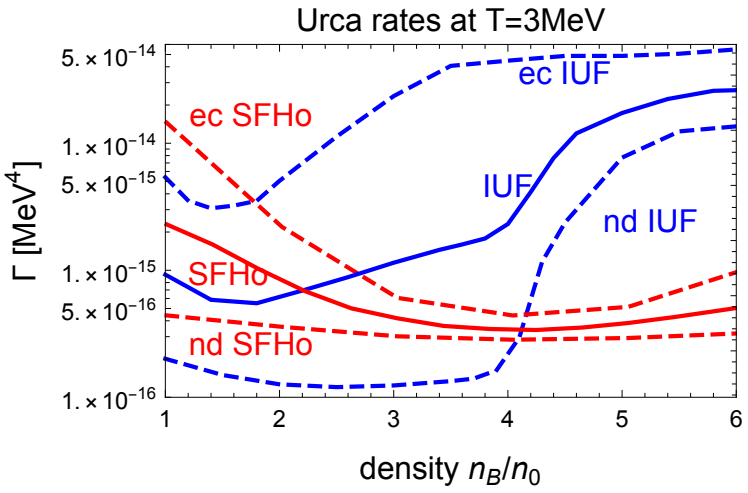

Fig. 2.6: Urca (direct plus modified) rates for IUF and SFHo EoSs at $T = 3\,\mathrm{MeV}$. When $\Delta\mu = 0$ (dashed lines) the rates for neutron decay (nd) and electron capture (ec) do not balance. With the correct choice of $\Delta\mu$ (Figs. 2.4, 2.5) the neutron decay and electron capture rates (solid lines) become equal and the system is in beta equilibrium.

less suppressed than neutron decay, requiring a positive value of $\Delta\mu$ to decrease the proton fraction and equalize the rates.

The density dependence of the correction $\Delta\mu$ is more complicated, depending on specific features of the equations of state. We will discuss this in more detail below.

2.6.2 Urca Rates

Fig. 2.6 illustrates how, without the nonzero-temperature correction $\Delta\mu$ (dashed lines), the neutron decay (nd) and electron capture (ec) rates become very different when the temperature rises to 3 MeV. For both EoSs, electron capture is significantly faster than neutron decay, so a positive $\Delta\mu$ will be required to balance the rates and establish beta equilibrium (solid lines). This is because a positive $\Delta\mu$ reduces the proton fraction. The resultant change in the phase space near the neutron and proton Fermi surfaces enhances the

neutron decay rate and suppresses electron capture, bringing the two processes into balance with each other.

For IUF, the mismatch between electron capture and neutron decay is greatest just below the IUF direct Urca threshold density of $4\,n_0$, which explains why for IUF $\Delta\mu$ reaches its highest value there (Fig. 2.4). For SFHo, the mismatch is smallest at that density, which explains why for SFHo $\Delta\mu$ reaches a local minimum there (Fig. 2.5).

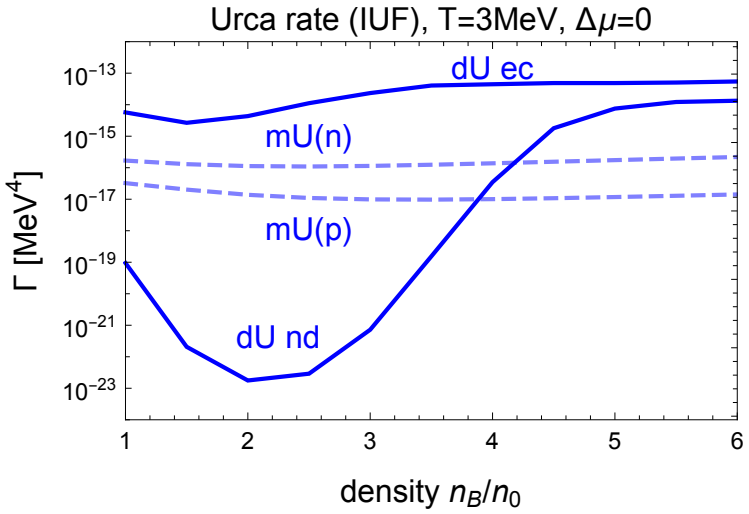

Fig. 2.7: Urca rates calculated using the IUF EoS at $T = 3\,\mathrm{MeV}$. Because $\Delta\mu = 0$ there is a large mismatch between the direct Urca rates for neutron decay and electron capture. Modified Urca (with neutron spectator (n) and proton spectator (p)) rates are calculated in the Fermi surface approximation and therefore match automatically.

Figs. 2.7 and 2.8 give further insight in to the density dependence of the rates by showing the separate contributions from direct and modified Urca.

For IUF (Fig. 2.7), in the dUrca-forbidden density range one would expect that the direct Urca rates should be exponentially suppressed at low temperature, leaving the modified Urca rates which automatically balance when $\Delta\mu = 0$ because they are calculated in the Fermi Surface approximation. We see that the direct Urca neutron decay rate is indeed strongly

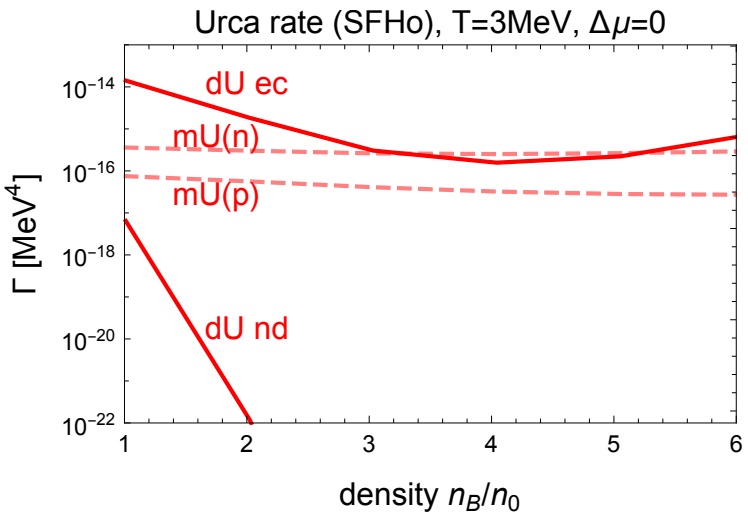

Fig. 2.8: Urca rates calculated using the SFHo EoS at $T = 3\,\mathrm{MeV}$. Because $\Delta\mu = 0$ there is a large mismatch between the direct Urca rates for neutron decay and electron capture. Modified Urca (with neutron spectator (n) and proton spectator (p)) rates are calculated in the Fermi surface approximation and therefore match automatically.

suppressed, but the direct Urca electron capture rate only shows a slight reduction below the threshold, and remains well above the modified Urca rates. This mismatch is what leads to a positive correction $\Delta\mu$ in beta equilibrium. We will explain below why this is the case.

For SFHo (Fig. 2.8), the analysis is similar: neutron decay is heavily suppressed as expected in the dUrca-forbidden region (up to infinite density), but electron capture is much less suppressed. In the middle density range (3 to $5\,n_0$) where mUrca is dominant there is no need for a correction, since the mUrca rates balance at $\Delta\mu = 0$. However, at lower or higher densities the direct Urca electron capture rate becomes large enough to dominate, so a positive $\Delta\mu$ will be required to pull it down and establish equilibrium between neutron decay and electron capture.

In the next subsection we analyze the imbalance between electron capture and neutron decay rates in the dUrca-forbidden density range. This imbalance is the reason why a nonzero

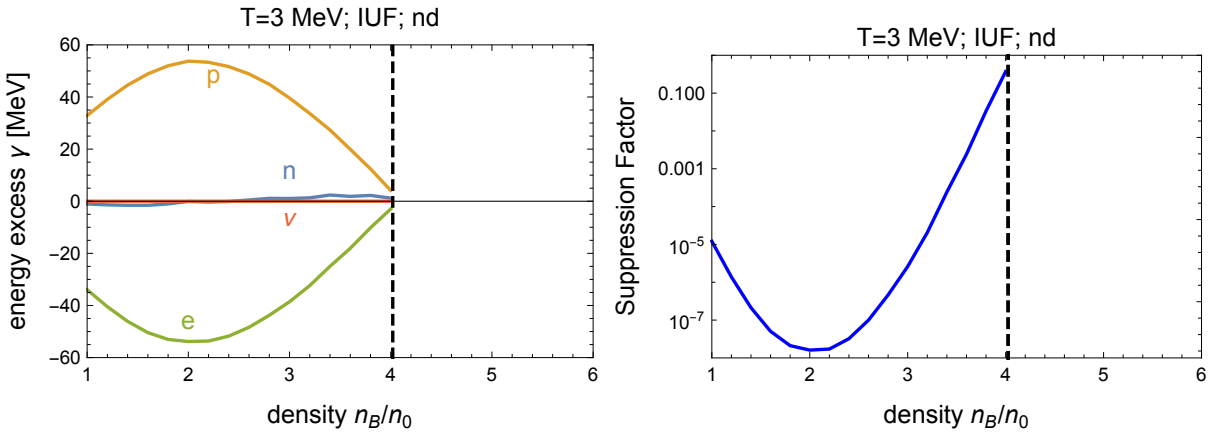

Fig. 2.9: The optimal kinematics for neutron decay for the IUF EoS. Left panel: the least suppressed kinematic arrangement, showing the energy distance γ of each particle from its Fermi surface. Right panel: the Fermi-Dirac suppression factor, $e^{-|\gamma_e|/T} e^{-|\gamma_n|\Theta(\gamma_n)/T}$ which is dominated by the difficulty of finding an electron hole at energy γ_e below its Fermi surface.

$\Delta\mu$ is required in beta equilibrium. We can understand the difference in the rates, and their density dependence, by looking at which parts of the phase space dominate the rate integrals. This is largely determined by the Fermi-Dirac factors in the rate integrals, since the matrix element depends only weakly on the magnitudes of the momenta.

2.6.3 Direct Urca suppression factors

The density and temperature dependence of the direct Urca rates is dominated by the Fermi-Dirac factors. Below the dUrca threshold density, at zero temperature all direct Urca processes would be forbidden, but at nonzero temperature the Fermi surfaces are blurred, so there is some non-zero occupation of particle and hole states in regions of momentum space where the direct Urca process is kinematically allowed. The rate is governed by the Fermi-Dirac suppression factors for those momentum states.

At each density and temperature we search for the combination of momenta that is least

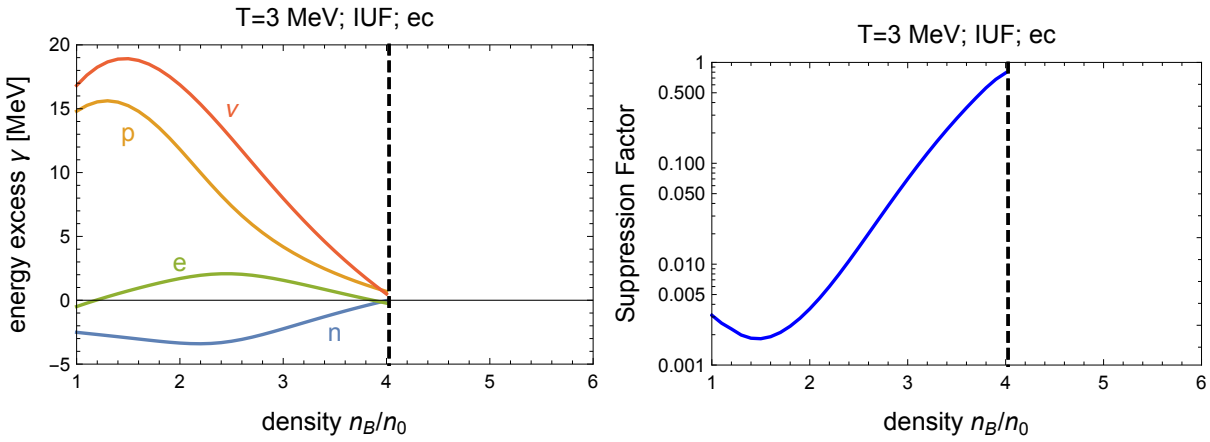

Fig. 2.10: The optimal kinematics for electron capture for the IUF EoS. Left panel: the least suppressed kinematic arrangement, showing the energy distance γ of each particle from its Fermi surface. Right panel: the overall Fermi-Dirac suppression factor, $e^{-|\gamma_p|/T}e^{-|\gamma_e|\Theta(\gamma_e)/T}e^{-|\gamma_n|\Theta(-\gamma_n)/T}$, which is dominated by the difficulty of finding a proton at energy γ_p above its Fermi surface.

suppressed, i.e. that maximizes the product of Fermi-Dirac factors in the rate integral while maintaining energy-momentum conservation. The magnitude of that product of Fermi-Dirac factors tells us how suppressed the whole process will be, at that density and temperature.

Below the direct Urca threshold density, considering particles near their Fermi surfaces, the neutron has a momentum larger than the sum of proton and electron momenta, even if the proton and electron are coaligned (see Fig. 2.1). In this regime, the direct Urca kinematics will become essentially one-dimensional, as this is how the electron and proton momenta can come closest to adding up to the large neutron momentum. We take the neutron momentum to be positive, so a negative momentum indicates motion in the direction opposite of the neutron. For momentum conservation to hold, the electron and proton will have to be away from their Fermi surfaces. In the assumption of one-dimensional kinematics, we determine the optimal momenta $\{k_n^{\rm opt}, k_p^{\rm opt}, k_e^{\rm opt}, k_\nu^{\rm opt}\}$ as follows. For neutron decay, we maximize $f_n(1-f_p)(1-f_e)$ and for electron capture we maximize $(1-f_n)f_pf_e$. Energy and (one-dimensional) momentum conservation impose two constraints on the momentum, leaving

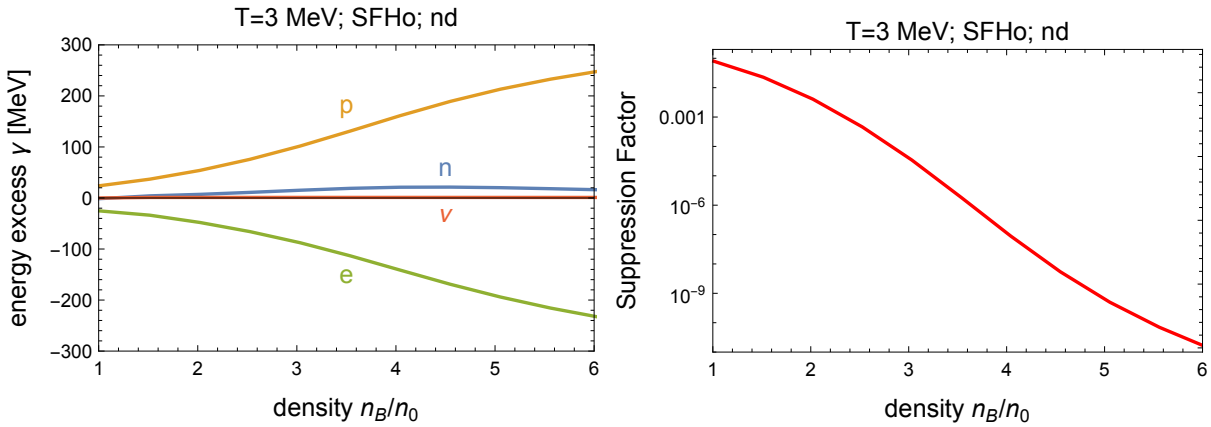

Fig. 2.11: The optimal kinematics for neutron decay at $T = 3\,\mathrm{MeV}$ for SFHo, obtained by maximizing the Fermi-Dirac products. The suppression factor, $e^{-|\gamma_e|/T} e^{-|\gamma_n|\Theta(\gamma_n)/T}$ is dominated by the difficulty of finding an electron hole below its Fermi surface.

two independent momenta over which to maximize.

The results of this maximization exercise are shown for the IUF EoS in Figs. 2.9 and 2.10, and for SFHo in Figs. 2.11 and 2.12.

The left panels show how far from their Fermi surfaces the particles are in the least Fermi-Dirac-suppressed kinematic configuration. For each particle i we show $\gamma_i \equiv E_i^{\mathrm{opt}} - E_{Fi}$, which is the extra energy the particle with its optimal momentum has relative to its Fermi energy. The curves only exist in the dUrca-forbidden region, which for IUF ends slightly above $4\,n_0$. (In the dUrca-allowed region all particles can be on their Fermi surfaces, so the curves would be trivially zero and are not shown). The right panels show the maximum value of the Fermi-Dirac factor, which gives the overall suppression of the process.

Neutron decay Direct Urca neutron decay is suppressed because the neutrons at their Fermi surface have just enough energy to make a proton and electron near their Fermi surfaces (this is a consequence of the beta equilibrium condition (2.6)), but too much momentum (Fig. 2.1). The process can still proceed (with an exponential suppression factor) by exploiting the

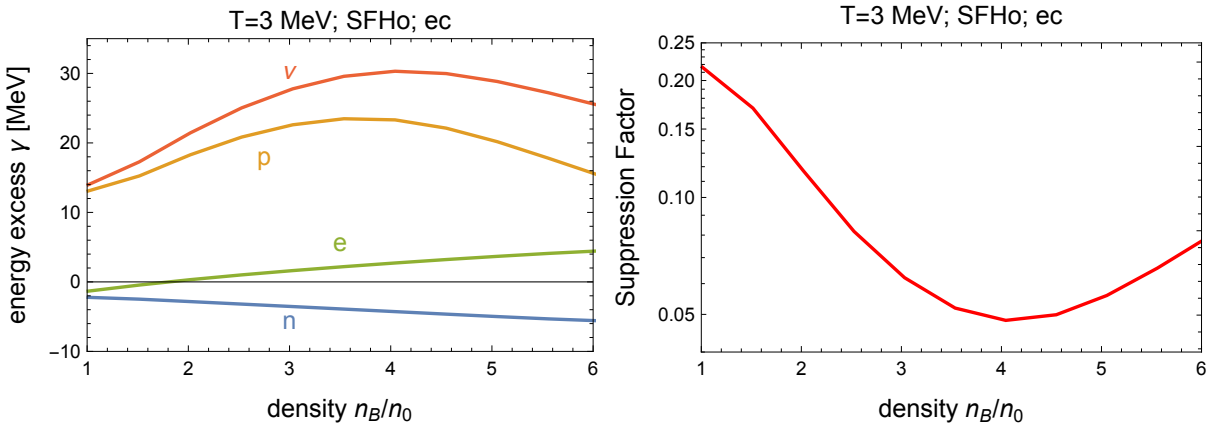

Fig. 2.12: The optimal kinematics for electron capture at $T = 3\,\mathrm{MeV}$ for SFHo, obtained by maximizing the Fermi-Dirac products. The suppression factor, $e^{-|\gamma_p|/T} e^{-|\gamma_e|\Theta(\gamma_e)/T} e^{-|\gamma_n|\Theta(-\gamma_n)/T}$, is dominated by the difficulty of finding a proton above its Fermi surface.

thermal blurring of the Fermi surfaces. Figs. 2.9 (IUF) and 2.11 (SFHo) show that the best option is to create a proton at energy γ_p above its Fermi surface and an electron at energy $\gamma_e = -\gamma_p$ which is below its Fermi surface. The co-linear proton and electron now have more momentum then when they were both on their Fermi surfaces because the proton's momentum rises rapidly with γ_p because the proton is less relativistic, whereas the electron's momentum drops more slowly as γ_e becomes more negative, because the electron is ultrarelativistic. The creation of the proton incurs no Fermi-Dirac suppression because states above the Fermi surface are mostly empty, but the creation of the electron is suppressed by a Fermi-Dirac factor of $e^{-|\gamma_e|/T}$ reflecting the scarcity of electron holes available to take such an electron. The net suppression of the rate, $e^{-|\gamma_e|/T} e^{-|\gamma_n|\Theta(\gamma_n)/T}$, is shown in the right panels of Figs. 2.9 (IUF) and 2.11 (SFHo). For IUF we see the strongest suppression at around $2\,n_0$, which explains the density dependence of the IUF neutron decay rate shown in Fig. 2.7. For SFHo, since the dUrca-forbidden region extends up to infinite density, and the momentum deficit remains large across the density range surveyed, we see stronger suppression that does

not relent at the upper end of the density range, explaining the almost total suppression seen in Fig. 2.8.

We can understand the density dependence of γ_p in terms of the one-dimensional model within which the maximization was performed.

We assume that, as seen in Figs. 2.9 (IUF) and 2.11 (SFHo), the neutron remains on its Fermi surface, and the neutrino takes negligible energy/momentum, since lack of momentum to build the final state is the main obstacle. Conservation of energy and momentum then tells us that

$$k_{Fn} = k_p^{\rm opt} + k_e^{\rm opt} \ , \tag{2.25}$$

$$E_{Fn} = E_p(k_p^{\rm opt}) + k_e^{\rm opt} \ . \tag{2.26}$$

Using the dispersion relations (2.8) we can solve for $k_p^{\rm opt}$ and $k_e^{\rm opt}$ and, after using that $E_{Fn} = E_{Fp} + E_{Fe}$ (since we have assumed $\Delta\mu = 0$), we find

$$k_p^{\rm opt} - k_{Fp} = \frac{\Delta k(2E^*_{Fp} - \Delta k)}{2(E^*_{Fp} + k_{Fp} - k_{Fn})} \ , \tag{2.27}$$

where $\Delta k \equiv k_{Fn} - k_{Fp} - k_{Fe}$ is the momentum deficit (we plotted the surplus $-\Delta k$ in Fig. 2.1). From this analysis, we learn that the density dependence of γ_p, and therefore the rate, not only depends on the momentum deficit Δk, but on the relative behavior of the neutron and proton Fermi momenta and their effective masses.

Although the momentum deficit Δk in IUF monotonically shrinks with density, γ_p shows a slight increase at low densities due to the fast drop of the effective proton mass m_p^* (see Fig. 2.3). This fast decrease counter-intuitively leads E^*_{Fp} to drop with density, while the real Fermi energy, which includes the nuclear mean field, U_p, rises with density as expected.

Closer to the threshold density, the momentum deficit dominates the behavior of γ_p and the rate, so that γ_p goes to zero at the threshold as Δk approaches zero, leading to $k_p^{\rm opt} = k_{Fp}$ as expected.

For the SFHo EoS, the direct Urca momentum deficit is only varying weakly with density (see again Fig. 2.1). Although the momentum deficit is slowly falling, γ_p continues to rise with density as shown in Fig. 2.11. This is due to the neutron Fermi momentum which rises fast enough that the denominator in Eq. (2.27) decreases by more than a factor of five in the studied density range while the momentum surplus stays nearly constant in comparison.

Electron capture [0.5ex] In the dUrca-forbidden density range, using the one-dimensional kinematics described above, we find that the optimal kinematics for electron capture has a proton above its Fermi surface and an electron close to its Fermi surface combining to make a neutron slightly below its Fermi surface and a neutrino. The Fermi-Dirac suppression factor is $e^{-\gamma_p/T} e^{-|\gamma_e|\Theta(\gamma_e)/T} e^{-|\gamma_n|\Theta(-\gamma_n)/T}$, reflecting the scarcity of protons and electrons above their Fermi surfaces, and of neutron holes below the neutron Fermi surface.

Figs. 2.10 and 2.12 show the corresponding energy excesses γ_i and Fermi-Dirac suppression factors. In the right panels we see that in the dUrca-forbidden region, electron capture is somewhat suppressed but not nearly as suppressed as neutron decay. This is because, as we explain below, it is able to proceed using a proton that is much closer to its Fermi surface than is possible for neutron decay, and there is correspondingly less Fermi-Dirac suppression (compare the left panels of Figs. 2.9 vs. 2.10, and Figs. 2.11 vs. 2.12).

The special feature of electron capture is that there is a very efficient way to exploit the thermal blurring of the Fermi surfaces. Given a momentum shortfall $\Delta k \equiv k_{Fn} - k_{Fp} - k_{Fe}$, we can start with a proton whose momentum is less than Δk above the Fermi surface. The rarity of finding such a proton leads to a Fermi-Dirac suppression factor of $e^{-|\gamma_p|/T}$. This proton captures an electron near its Fermi surface with momentum parallel to the proton's.

At this point their combined momentum is not enough to make a neutron on its Fermi surface, and there is excess energy. But we can use that excess energy to create, along with a neutron on its Fermi surface, a neutrino whose momentum partly cancels the neutron momentum, so the combined momentum of the proton and electron is enough to create that final state.

Because of the "help" from the neutrino, the proton does not need to be as far above its Fermi surface as the proton in neutron decay, so the electron capture rate is suppressed by a smaller Fermi-Dirac factor,

The density dependence of the suppression factors (right panels of Fig. 2.10 for IUF and Fig. 2.12 for SFHo) explain the density dependence of the direct Urca electron capture rates shown in Figs. 2.7 and Figs. 2.8.

To understand the density dependence of γ_p, we can perform a similar analysis as for neutron decay. We now assume neutron and electron to be on their Fermi surfaces, as shown in Figs. 2.10 (IUF) and 2.12 (SFHo), which is not as good as an assumption compared to the neutron decay analysis, but still helps us to gain insight into the behavior of the rates. Energy-momentum conservation again allows us to deduce that

$$k_{Fn} = k_p^{\rm opt} + k_{Fe} + k_\nu^{\rm opt} \,, \tag{2.28}$$

$$E_{Fn} + k_\nu^{\rm opt} = E_p(k_p^{\rm opt}) + k_{Fe}^{\rm opt} \,, \tag{2.29}$$

which leads, following the same procedure as in the neutron decay case, to

$$k_p^{\rm opt} - k_{Fp} = \frac{\Delta k(\Delta k + 2E_{Fp}^*)}{2(E_{Fp}^* + k_{Fn} - k_{Fp})} \,. \tag{2.30}$$

For IUF at low densities, we can neglect the proton Fermi momentum compared to the

effective mass. The behavior of γ_p is then again dominated by the effective proton mass, whose rapid decrease overcomes the rising neutron Fermi momentum at low densities. This pushes the proton further away from its Fermi surface at low densities, before the momentum surplus dominates the behavior of γ_p as the threshold is approached. As for neutron decay, $\Delta k = 0$ at the threshold, therefore the rate is again dominated by particles on their respective Fermi surfaces.

For SFHo, the momentum surplus is becoming smaller from n_0 to $3\,n_0$ while the combination of the effective masses and Fermi momenta in (2.30) varies slowly with density. This allows the behavior of the momentum surplus Δk to dominate the behavior of γ_p at low densities, so both are increasing and therefore pushing the proton further away from its Fermi surface initially. At higher densities, SFHo is seemingly approaching asymptotically a direct Urca threshold. Both the momentum surplus and the Fermi momenta and effective masses in Eq. (2.30) are pushing the ideal proton momentum back closer to the Fermi surface. Overall, the behavior of the electron capture rate in SFHo can therefore largely be explained by the density dependence of the momentum surplus.

2.6.4 Non-relativistic Rate vs. Relativistic Rate

In Sec. 2.3 we emphasized that as the density rises above about $2n_0$ relativistic corrections become important in the nucleon dispersion relations. In this section we illustrate the importance of relativistic corrections in the neutron decay rate.

2.6.4.1 Direct Urca neutron decay

Fig. 2.13 shows various approximations to the direct Urca neutron decay rate at $T = 3\,\mathrm{MeV}$ (with $\Delta\mu = 0$). We show the rate calculated with fully relativistic dispersion relations, with

the non-relativistic dispersion relation

$$E_N = m_N^* + \frac{p_N^2}{2m_N^*} + U_N \,, \tag{2.31}$$

and with the "vacuum dispersion relation" used in [73],

$$E_N = m_{\text{eff,N}} + \frac{p_N^2}{2m_N} \,, \tag{2.32}$$

where $m_N = 940\,\text{MeV}$, and $m_{\text{eff,N}}$ is chosen such that $E_N(p_F) = \mu_N$.

For the non-relativistic curves, we use a corresponding non-relativistic approximation of the rescaled matrix element (B.3),

$$\mathcal{M} = 1 + 3g_A^2 + (1 - g_A^2)\frac{\vec{p}_e \cdot \vec{p}_\nu}{E_e E_\nu} \,, \tag{2.33}$$

see Refs. [73, 3], and the derivation in Appendix C of [117]. We see that relativistic corrections make an enormous difference to the rate. The non-relativistic approximation is reasonably accurate at low density (where the nucleons are indeed non-relativistic) but overestimates the rate by up to eight orders of magnitude (at $T = 3\,\text{MeV}$) between $2\,n_0$ and the direct Urca threshold at $4.1\,n_0$. Due to the breakdown of the non-relativistic approximation, the direct Urca threshold condition is incorrectly already fulfilled below two times saturation density, which explains the steep increase of the non-relativistic rate around this density. For a detailed discussion of the density dependence of the relativistic rate, see Sec. 2.6.3.

The thermal blurring of the Fermi energy, which is proportional to the temperature T, translates to a blurring in momentum space of order T/v_F, where v_F is the Fermi velocity. In the correct relativistic treatment, v_F has an upper bound of 1, whereas for the non-relativistic dispersion relation, the Fermi velocity grows without a limit. This leads to a suppression of

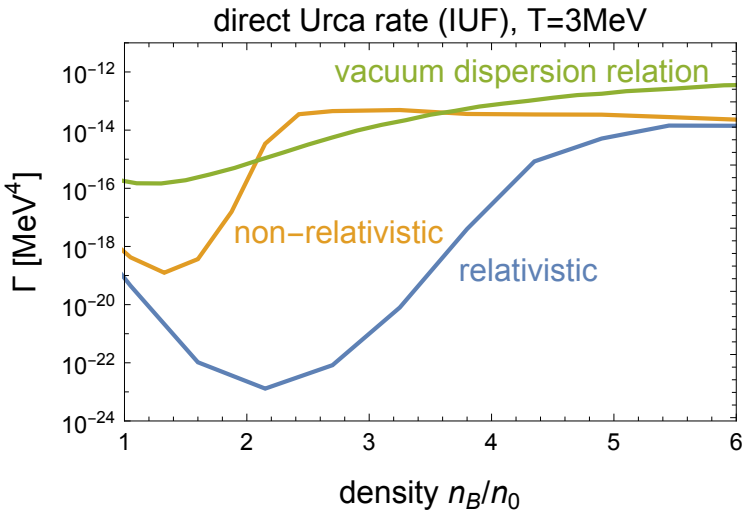

Fig. 2.13: Direct Urca neutron decay rate calculated using relativistic, non-relativistic and the vacuum dispersion relations at $T = 3\,\mathrm{MeV}$ for IUF.

the non-relativistic rate at higher densities which partially cancels the effects of the earlier threshold.

The "vacuum dispersion relation" gives a rate that is one to eight orders of magnitude too large (at $T = 3\,\mathrm{MeV}$), and is less suppressed at higher densities since the corresponding Fermi velocity stays comparatively small in the plotted density range.

2.6.4.2 Modified Urca neutron decay

Fig. 2.14 shows the importance of using relativistic dispersion relations in calculating modified Urca. The rates are calculated for the IUF equation of state in the Fermi surface approximation at $T = 3\,\mathrm{MeV}$. The relativistic rate is about 1 to 2 orders of magnitude smaller than the non-relativistic rate. The modified Urca rates are not sensitive to the direct Urca threshold because of the spectator providing extra momenta. Much of the difference between the non-relativistic calculation and the relativistic calculation comes from the prefactors, as shown in Sec. 2.5 and Eqs. (C.14), (C.17), (C.15) and (C.18). The relativistic

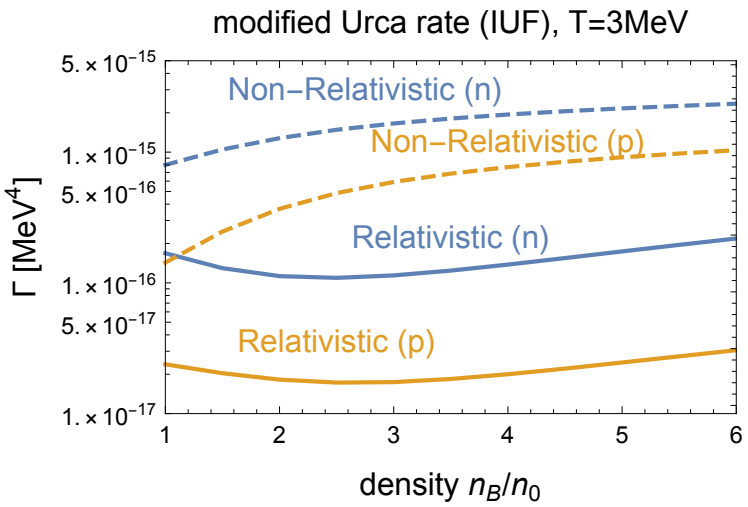

Fig. 2.14: Modified Urca rate calculated using relativistic and non-relativistic dispersion relations at $T = 3\,\mathrm{MeV}$ for IUF. (n) stands for neutron-spectator modified Urca and (p) stands for proton-spectator modified Urca.

rates are suppressed by $\prod_i m_i^*/E_i^*$, where i is the index for each of the nucleons participating the interaction. Notice that the proton-spectator modified Urca rate is always less than the neutron-spectator rate because the proton Fermi surface, and its accompanying phase space, is smaller.

2.7 Conclusions

We have investigated the conditions for beta equilibrium in nuclear matter in neutron stars, focusing on the temperature range where the material is cool enough so that neutrinos escape ($T \lesssim 5\,\mathrm{MeV}$) but warm enough so that nonzero temperature corrections to the Fermi surface approximation play an important role ($T \gtrsim 1\,\mathrm{MeV}$).

Previous work [73] found that a nonzero-temperature correction $\Delta\mu$ to the traditional beta equilibrium condition (Eq. (2.7)) was required to balance the rate of neutron decay

against the rate of electron capture. We have improved on that calculation by using a consistent description of nuclear matter, based on two relativistic mean field models, IUF and SFHo.

We find that when using relativistic mean field models it is important to use the full relativistic dispersion relations of the nucleons. In these theories the effective masses drop quickly with density, so the neutrons become relativistic at densities of 2 to $3\,n_0$. Using non-relativistic nucleon dispersion relations can make the modified Urca rates wrong by an order of magnitude and the direct Urca rates wrong by many orders of magnitude.

Our results for the nonzero-temperature correction $\Delta\mu$ are shown in Figs. 2.4 and 2.5. We find that it rises with the temperature, and can be of order 10 to 20 MeV for temperatures in the 3 to 5 MeV range. The density dependence is quite different for the two EoSs that we studied, and we showed in detail how it depends on specific properties of the EoS.

We find that the nonzero-temperature correction plays an important role in the correct calculation of Urca rates. Using the naive (low-temperature) beta equilibrium condition $\mu_n = \mu_p + \mu_e$ at $T = 3\,\mathrm{MeV}$ would yield electron capture rates that are too large by an order of magnitude, and neutron decay rates that are too small by an order of magnitude (Fig. 2.6). This would significantly affect calculations of neutrino emissivity in the cooler regions of a neutron star merger, and therefore the estimated energy loss due to neutrinos. Currently used neutrino leakage schemes (e.g. Ref. [118] and references therein), which often treat the temperature range $T \lesssim 5\,\mathrm{MeV}$ as neutrino free streaming, need to be adapted to the corrected beta equilibrium. Additionally, the bulk viscosity of nuclear matter [55] depends on the rate of the Urca process which restores the system to beta equilibrium. The improved calculation of the Urca rates presented here will modify the temperatures and densities at which bulk viscosity reaches its maximum strength. Using the correct beta equilibrium condition also affects the equation of state: a recent study estimated its impact to be at the 5% level [119],

and it would be interesting to evaluate the impact by performing a merger simulation using an EoS that incorporates the the finite-temperature correction described in this paper.

Chapter 3

Isospin Equilibration

We analyze the isospin ("beta") equilibration properties of neutrino-transparent nuclear (npe) matter in the temperature and density range that is relevant to neutron star mergers. With the state-of-the-art direct Urca rate calculation and the correction to the beta-equilibrium developed in the previous chapter, we find that the isospin relaxation rate rises rapidly as temperature rises, and at $T \approx 5$MeV, it is comparable to the timescale of the density oscillations that occur immediately after the merger. This produces a resonant peak in the bulk viscosity at $T \approx 5$MeV, which causes density oscillations to be damped on the timescale of the merger. We conclude that there is good reason to include isospin relaxation dynamics in merger simulations.

3.1 Introduction

Nuclear matter in neutron stars relaxes towards isospin ("beta") equilibrium; its steady state has an equilibrium proton fraction $x_p^{\rm eq}$ which is a function of baryon density n_B and temperature T. Equilibrium is established by weak interactions which operate on a timescale that can range from microseconds to minutes. Astrophysical phenomena such as density oscillations in neutron stars, which can be on a similar timescale, can therefore drive the

system out of equilibrium, and the dynamics of the relaxation process may be relevant to our understanding of the astrophysics.

In this analysis we focus on the astrophysical conditions found in neutron star mergers, where homogeneous nuclear matter at densities from one to several times nuclear saturation density n_0 and temperatures up to 80 MeV undergoes compression and rarefaction on millisecond timescales [79, 55], likely driving the system out of isospin equilibrium [119].

We calculate physical quantities relevant for isospin equilibration in neutrino-transparent homogeneous nuclear matter at densities above nuclear saturation density. Neutrino transparency is an approximation to the complex dynamics of neutrinos [69, 120] and is expected to become less reliable as temperatures rise beyond a few MeV [73], so we focus our calculation on the range $0 < T < 10\,\mathrm{MeV}$. We neglect muons because they introduce extra processes requiring a more sophisticated treatment. Previous analyses have found that they do not make a large difference to the equilibration and relaxation rates [65], so we postpone their inclusion to future work. The quantities we calculate are the isospin relaxation rate γ_I and the the frequency-dependent bulk viscosity ζ and damping (sound attenuation) time for density oscillations.

Previous work on this topic has assumed that the condition for isospin equilibrium is $\mu_n = \mu_p + \mu_e$. As we will now discuss, this is only valid at temperatures below about 1 MeV. At the temperatures attained in neutron star mergers there is a non-negligible correction to this condition. In this paper, we calculate the isospin relaxation rate and bulk viscosity using the proper equilibrium condition.

In the infinite volume thermodynamic limit, equilibrium is established when the forward and backward rates of each process are equal ("detailed balance"), so the equilibrium condition is a simple equality involving chemical potentials. However, neutrino transparency is a finite-volume effect, arising when the mean free path of neutrinos is not much smaller than

the size of the system. In a neutrino-transparent system neutrinos only occur in final states, never in initial states, so the system does not obey the principle of detailed balance. Equilibrium is attained when there is a balance between *different* processes: neutron decay and electron capture (as seen in (3.24) and (3.25) below). In general, the equilibrium condition in neutrino-transparent matter takes the form [67, 73],

$$\mu_n = \mu_p + \mu_e - \mu_I^{\rm eq}(n_B, T) \ , \tag{3.1}$$

where there is an isospin chemical potential $\mu_I^{\rm eq}$ whose value is determined by the requirement that the net rate of isospin creation is zero, i.e., the neutron decay and electron capture rates (3.26) are equal,

$$\Gamma_I \equiv \Gamma_{n\to p}^{\rm net} = 0 \tag{3.2}$$

At sufficiently low temperatures, $T \ll 1\,\mathrm{MeV}$, the correction $\mu_I^{\rm eq}$ in (3.1) becomes negligible because the Fermi surface approximation is valid: the Fermi-Dirac distribution exponentially suppresses contributions from particles away from their Fermi surfaces and the energy carried away by neutrinos is negligible (of order T). If neutrinos are kinematically negligible then neutron decay and electron capture are effectively the time-reverse of each other, $n \leftrightharpoons p\, e^-$, and the isospin equilibrium condition can be obtained from applying detailed balance to that process, yielding $\mu_n = \mu_p + \mu_e$, i.e., $\mu_I^{\rm eq} = 0$. However, as the temperature rises above about $1\,\mathrm{MeV}$, $\mu_I^{\rm eq}$ becomes non-negligible, and can reach values as large as 20 MeV (see Fig. 3.1 and Refs. [67, 73]). The main purpose of this paper is to calculate isospin equilibration properties of nuclear matter taking this correction into account. We hope this will clarify the relevance of isospin relaxation and help researchers performing merger simulations to decide when they should include isospin relaxation dynamics in their evolution algorithms.

In Sec. 3.2 we derive expressions for the isospin relaxation rate and the bulk viscosity in terms of the microscopic isospin equilibration rate Γ_I, i.e., the rate of Urca processes. In Sec. 3.3 we describe the relativistic mean field theories (RMFTs) that we use to model nuclear matter. In Sec. 3.4 we summarize the calculation of the Urca rates and in Sec. 3.5 we present our results.

We use natural units where $\hbar = c = k_B = 1$.

3.2 Isospin equilibration of nuclear matter

We now derive expressions for the isospin relaxation rate γ_I and the bulk viscosity ζ of neutrino-transparent *npe* mattter at arbitrary temperature. We will assume that matter always remains locally electrically neutral, so all calculations are performed at constant charge density $n_Q = 0$. The derivation in this section is applicable to both isothermal and adiabatic density oscillations, by taking the derivatives at constant temperature or constant entropy per baryon respectively. In the presentation below we will not explicitly show the dependence on T or s/n_B.

3.2.1 Isospin relaxation

In neutrino-transparent nuclear $npe(\mu)$ matter, in addition to the conserved baryon number B and conserved electric charge Q there is another "briefly-conserved" charge, isospin I. The relevant charge densities and chemical potentials can be related to the net densities and

chemical potentials of neutrons (n), protons (p) and electrons (e),

$$\begin{aligned} n_B &= n_p + n_n \ , \\ n_I &= \tfrac{1}{2} n_p - \tfrac{1}{2} n_n \ , \\ n_Q &= n_p - n_e \ , \\ \mu_B &= \tfrac{1}{2}\mu_p + \tfrac{1}{2}\mu_n + \tfrac{1}{2}\mu_e \ , \\ \mu_I &= \mu_p - \mu_n + \mu_e \ , \\ \mu_Q &= -\mu_e \ . \end{aligned} \tag{3.3}$$

The expressions above do not include a chemical potential for lepton number because the neutrinos are far from thermal equilibrium so there is no associated chemical potential.

It will be convenient to define the isospin fraction x_I, which is simply related to the proton fraction ($x_p \equiv n_p/n_B$),

$$x_I \equiv \frac{n_I}{n_B} = x_p - \tfrac{1}{2} \ . \tag{3.4}$$

For many purposes we can treat x_I as equivalent to x_p, since $\partial/\partial x_I$ is the same as $\partial/\partial x_p$, and a derivative at constant x_I is also a derivative at constant x_p.

As noted in Sec. 3.1, on strong-interaction ($\sim 10^{-23}\,\mathrm{s}$) timescales all three charges are conserved, but on longer timescales the weak interactions break isospin, so μ_I and x_I relax to their beta equilibrated values μ_I^{eq} and x_I^{eq}. To analyze this equilibration process, where the system has been driven out of equilibrium by a density oscillation, it is natural to work in terms of n_B and x_I, since baryon density is the quantity that tracks the density oscillation, and the isospin fraction tracks relaxation to equilibrium.

Isospin equilibration of isospin is governed by the rate equation

$$\frac{dn_I}{dt} = \frac{n_I}{n_B}\frac{dn_B}{dt} + \Gamma_I(n_B, x_I) \ . \tag{3.5}$$

The first term on the right side tells us that if isospin were conserved then compression would change the isospin density by the same fraction as it changes baryon density. In the second term Γ_I is the *isospin production rate*, i.e., the net rate per unit volume at which isospin increases, or equivalently the net rate at which neutrons are converted to protons. In Sec. 3.4 we describe how it can be calculated from the Fermi theory of weak interactions by integrating the net $n \to p$ rate over the Fermi-Dirac distributions of protons, neutrons, and electrons.

Using the definition (3.4), the rate equation (3.5) becomes

$$\frac{dx_I}{dt} = \frac{1}{n_B}\Gamma_I(n_B, x_I) \ , \tag{3.6}$$

and the equilibrium isospin fraction $x_I^{\rm eq}(n_B)$ is defined by

$$\Gamma_I\Big(n_B, x_I^{\rm eq}(n_B, T)\Big) = 0 \ . \tag{3.7}$$

If x_I is above its equilibrium value then there are too many protons, so the rate of $p \to n$ becomes larger than $n \to p$; Γ_I should then become negative, driving x_I back down towards its equilibrium value. To obtain physically relevant quantities such as the isospin relaxation rate and bulk viscosity we consider a generic small departure from equilibrium,

$$\Gamma_I(\bar{n}_B + \Delta n_B, \bar{x}_I + \Delta x_I) = \left.\frac{\partial \Gamma_I}{\partial n_B}\right|_{x_I} \Delta n_B + \left.\frac{\partial \Gamma_I}{\partial x_I}\right|_{n_B} \Delta x_I \, , \tag{3.8}$$

where $\bar{x}_I \equiv x_I^{\rm eq}(n_B)$. Using this in the rate equation (3.6) we obtain the rate equation for the isospin fraction

$$\frac{dx_I}{dt} = -\gamma_I \Delta x_I + \gamma_B \frac{\Delta n_B}{\bar{n}_B} \, , \tag{3.9}$$

where

$$\gamma_I \equiv -\frac{1}{\bar{n}_B}\frac{\partial \Gamma_I}{\partial x_I}\bigg|_{n_B} ,$$
$$\gamma_B \equiv \frac{\partial \Gamma_I}{\partial n_B}\bigg|_{x_I} , \tag{3.10}$$

with both the derivatives evaluated at $n_B = \bar{n}_B$, $x_I = \bar{x}_I$. According to (3.9) a small deviation of x_I from equilibrium (with no change in n_B) would evolve as $\dot{x}_I = -\gamma_I(x_I - x_I^{\rm eq})$, so we identify γ_I as the *isospin relaxation rate*, which we expect to be positive.

The other rate factor, γ_B, tells us how quickly equilibrium is restored in response to a change in density at fixed isospin fraction. In previous treatments (e.g. [121, 95, 122, 123, 124, 92, 88, 63]) this was simply related to γ_I (see (D.4)) because it was assumed that beta equilibrium corresponds to $\mu_I = 0$; however, as noted in Sec. 3.1, this is no longer true in neutrino-transparent matter at $T \gtrsim 1\,\mathrm{MeV}$.

3.2.2 Bulk viscosity

To see how isospin equilibration leads to bulk viscous damping, we consider a fluid element of nuclear matter, with pressure p, that is driven out of equilibrium by a small-amplitude density oscillation,

$$\begin{aligned} n_B(t) &= \bar{n}_B + \mathrm{Re}(\delta n_B\, e^{i\omega t}) , \\ x_I(t) &= \bar{x}_I + \mathrm{Re}(\delta x_I\, e^{i\omega t}) , \\ p(t) &= \bar{p} + \mathrm{Re}(\delta p\, e^{i\omega t}) . \end{aligned} \tag{3.11}$$

We assume that the oscillation occurs around equilibrium, so

$$\bar{x}_I = x_I^{\rm eq}(\bar{n}_B, T) . \tag{3.12}$$

We adopt the phase convention that the baryon density amplitude $\delta n_B \ll \bar{n}_B$ is real. Bulk viscous dissipation arises from a phase lag between pressure and density. The rate of energy dissipation for the the small-amplitude oscillation (3.11) is obtained from

$$W = -\frac{1}{\tau \bar{V}} \int_0^\tau p(t) \frac{dV}{dt} dt = \frac{1}{2} \omega \, \mathrm{Im}(\delta p) \, \frac{\delta n_B}{\bar{n}_B} \ , \tag{3.13}$$

where the period is $\tau = 2\pi/\omega$.

The hydrodynamic relation between bulk viscosity and rate of energy dissipation per unit volume is $W = \zeta (\nabla \cdot \vec{v})^2$, which for the small-amplitude oscillation (3.11) becomes (averaged over one oscillation period)

$$W = \frac{1}{2} \zeta \omega^2 \frac{(\delta n_B)^2}{\bar{n}_B^2} \ . \tag{3.14}$$

Identifying (3.13) with (3.14) we obtain the frequency-dependent bulk viscosity

$$\zeta(\omega) = \frac{\mathrm{Im}(\delta p)}{\delta n_B} \frac{\bar{n}_B}{\omega} \ . \tag{3.15}$$

For *npe* nuclear matter, where the phase lag of the pressure arises from the equilibration of isospin, this becomes

$$\zeta(\omega) = \frac{\bar{n}_B}{\omega} \left. \frac{\partial p}{\partial x_I} \right|_{n_B} \frac{\mathrm{Im}(\delta x_I)}{\delta n_B} \ . \tag{3.16}$$

We can now obtain the bulk viscosity of nuclear matter by analyzing the equilibration process in more detail, which will allow us to calculate the phase lag. Substituting the explicit form of the oscillations (3.11) in to the rate equation (3.9) we find the relationship between the amplitudes δx_I and δn_B

$$i\omega \delta x_I = -\gamma_I \delta x_I + \frac{\gamma_B}{\bar{n}_B} \delta n_B \tag{3.17}$$

which can be rewritten

$$\frac{\delta x_I}{\delta n_B} = \frac{1}{\bar{n}_B} \frac{\gamma_B}{\gamma_I + i\omega} \tag{3.18}$$

For the bulk viscosity (3.16) we take the imaginary part of (3.18),

$$\zeta = -\left.\frac{\partial p}{\partial x_I}\right|_{n_B} \frac{\gamma_B}{\gamma_I^2 + \omega^2} \ , \tag{3.19}$$

where γ_B and γ_I are defined in (3.10) This is the general expression for the bulk viscosity, valid even when temperature corrections shift the equilibrium away from its low temperature limit $\mu_I^{\rm eq} = 0$. In Appendix D we take the low temperature limit and show that previous calculations, which assumed $\mu_I^{\rm eq} = 0$, agree with the general result in that limit. In the low temperature limit (D.5) it is clear that the dependence of bulk viscosity on density and temperature features a resonant maximum when the relaxation rate $\gamma_I(n_B, T)$ coincides with the angular frequency ω of the density oscillation. This is less clear in the more general expression (3.19), but we have found that for typical equations of state $\mu_I^{\rm eq}$ varies slowly enough as a function of n_B and T so that $\gamma_B(n_B, T)$ is still roughly proportional to $\gamma_I(n_B, T)$ (the constant of proportionality is a slowly varying function of n_B and T), so the resonant peak is still present.

The bulk viscosity (3.19) can also be written

$$\zeta = \zeta_0 \, \frac{\gamma_I^2}{\gamma_I^2 + \omega^2} \ , \tag{3.20}$$

where

$$\zeta_0 = -\left.\frac{\partial p}{\partial x_I}\right|_{n_B} \frac{\gamma_B}{\gamma_I^2} \tag{3.21}$$

is the static (zero frequency) limit of the bulk viscosity. (Note that in the isothermal regime

the derivative of the pressure can be rewritten as a derivative of μ_I, see App. E). From the static bulk viscosity and the isospin relaxation rate γ_I, which are functions of n_B and T, one can reconstruct the full frequency-dependent bulk viscosity as a function of density and temperature.

3.3 Nuclear matter models

One of the most important features influencing the isospin relaxation rate of nuclear matter is the direct Urca threshold density, which separates the low-density range, where in the $T \to 0$ limit only modified Urca processes are allowed, from the high-density range where direct Urca processes are kinematically allowed (see Sec. 3.4). It is not known whether real-world nuclear matter has a direct Urca threshold in the relevant density range, so we perform calculations for two relativistic mean-field theories, IUF [59] and QMC-RMF3 [125]. Both are consistent with current astrophysical and nuclear constraints. IUF has a direct Urca threshold at 4 n_0 whereas QMC-RMF3 does not have a threshold in the range of densities found in neutron stars.

At a given baryon density n_B, temperature T, and proton fraction x_p we solve the RMFT mean field equations to obtain the values of the meson condensates, thermodynamic quantities such as the pressure and proton and neutron chemical potentials, and also the nucleon effective masses and energy shifts. The dispersion relations for nucleons in the relativistic mean field models are then specified,

$$E_n = \sqrt{m_n^{*2} + k_n^2} + U_n, \tag{3.22}$$

$$E_p = \sqrt{m_p^{*2} + k_p^2} + U_p, \tag{3.23}$$

where m_i^* are the effective masses, k_i are the particle momenta and U_i are the energy shifts. In RMFTs the effective masses and energy shifts are functions of density, temperature, and proton fraction. In the models that we use the protons and neutrons have the same effective mass, so the energy shifts play an important role by separating the neutron and proton energies and thereby opening up more phase space for the Urca processes.

3.4 Urca Rates

3.4.1 Overview of Urca processes

The isospin equilibration rate Γ_I (3.5) is given by the neutron decay and electron capture processes, which are governed by the weak interaction. Depending on the number of spectators, these processes are called direct or modified Urca. The direct Urca processes in neutrino transparent matter are neutron decay and electron capture

$$\begin{aligned} n &\to p + e^- + \bar{\nu}\,, \\ p + e^- &\to n + \nu\,. \end{aligned} \tag{3.24}$$

In most models of homogeneous nuclear matter the proton fraction x_p increases monotonically with the density. This means that for some models there is a direct Urca threshold density, defined as the density below which, in the limit $T \to 0$, the rate of the direct Urca process is exponentially suppressed. Since at low temperature the participating neutrons, protons, and electrons are all on their Fermi surfaces, the criterion for direct Urca to proceed is $k_{Fn} \leqslant k_{Fp} + k_{Fe}$ where k_{Fi} are the Fermi momenta for the particles. In *npe* matter this threshold is $x_p \geqslant 0.11$ since neutrality requires $k_{Fp} = k_{Fe}$. Below the threshold density, $k_{Fn} > k_{Fp} + k_{Fe}$, so momentum conservation forbids the direct Urca processes for particles

on their Fermi surfaces. In order for momentum conservation to be satisfied, some particles would need to be away from their Fermi surfaces, but this population is exponentially suppressed by their Fermi-Dirac distributions.

At densities below the direct Urca threshold, we expect the Urca rates to be dominated by the modified Urca process,

$$N + n \to N + p + e^- + \bar{\nu}\,, \tag{3.25}$$
$$N + p + e^- \to N + n + \nu\,,$$

where N is a spectator nucleon that can scatter from one part of its Fermi surface to another, injecting momentum via a virtual pion in to the accompanying direct Urca process.

We now discuss the calculation of the direct Urca ("dU") and modified Urca ("mU") rates, which establish beta equilibrium (see Sec. 3.2),

$$\Gamma_{\rm nd} = \Gamma_{\rm dU,nd} + \Gamma_{\rm mU,nd}\,, \tag{3.26}$$
$$\Gamma_{\rm ec} = \Gamma_{\rm dU,ec} + \Gamma_{\rm mU,ec}\,. \tag{3.27}$$

In this paper, we will calculate the direct Urca rates by integrating over the full phase space, including Fermi-Dirac-suppressed contributions that become non-negligible when the temperature rises to the MeV range [73]. We will calculate modified Urca rates in the Fermi surface approximation (in which participating nucleons and electrons are assumed to be on their Fermi surfaces) since modified Urca always has a non-suppressed contribution from such particles.

3.4.2 Direct Urca rates

The direct Urca neutron decay and electron captures rates are [3]

$$\Gamma_{\rm nd} = \int \frac{d^3k_n}{(2\pi)^3}\frac{d^3k_p}{(2\pi)^3}\frac{d^3k_e}{(2\pi)^3}\frac{d^3k_\nu}{(2\pi)^3} \\ f_n(1-f_p)(1-f_e)\frac{\sum|M|^2}{(2E_n^*)(2E_p^*)(2E_e)(2E_\nu)} \\ (2\pi)^4\delta^{(4)}(k_n - k_p - k_e - k_\nu)\,, \tag{3.28}$$

and

$$\Gamma_{\rm ec} = \int \frac{d^3k_n}{(2\pi)^3}\frac{d^3k_p}{(2\pi)^3}\frac{d^3k_e}{(2\pi)^3}\frac{d^3k_\nu}{(2\pi)^3} \\ (1-f_n)f_p f_e\,\frac{\sum|M|^2}{(2E_n^*)(2E_p^*)(2E_e)(2E_\nu)} \\ (2\pi)^4\delta^{(4)}(k_p + k_e - k_n - k_\nu)\,, \tag{3.29}$$

where $\Sigma|M|$ is the spin-summed matrix element, $E_i^* = \sqrt{k_i^2 + m_i^{*2}}$ are the effective nucleon dispersion relations, $E_e = \sqrt{k_e^2 + m_e^2}$ and $E_\nu = k_\nu$ are the electron/neutrino dispersion relations, and f_i are Fermi-Dirac distributions. Direct Urca rates are often calculated in various approximations such as using non-relativistic dispersion relations for the nucleons [122, 73, 62, 63], using vacuum masses for the nucleons [73], simplifying the matrix element [62, 63], or using the Fermi surface approximation [122].

Our direct Urca rate calculations use the complete matrix element, relativistic dispersion relations for all participating particles, and integrate momenta over the entire phase space. For details see Appendix A of Ref. [67].

3.4.3 Modified Urca rates

We use the standard expressions for the modified-Urca neutron decay and electron captures rates,

$$\begin{aligned}\Gamma_{mU,nd} = \int & \frac{d^3k_n}{(2\pi)^3}\frac{d^3k_p}{(2\pi)^3}\frac{d^3k_e}{(2\pi)^3}\frac{d^3k_\nu}{(2\pi)^3}\frac{d^3k_{N_1}}{(2\pi)^3}\frac{d^3k_{N_2}}{(2\pi)^3} \\ & (2\pi)^4\delta^{(4)}(k_n + k_{N_1} - k_p - k_e - k_\nu - k_{N_2}) \\ & f_n f_{N_1}(1-f_p)(1-f_e)(1-f_{N_2}) \\ & \left(s\frac{\sum|M|^2}{2^6 E_n^* E_p^* E_e E_\nu E_{N_1}^* E_{N_2}^*}\right),\end{aligned} \tag{3.30}$$

and

$$\begin{aligned}\Gamma_{mU,ec} = \int & \frac{d^3k_n}{(2\pi)^3}\frac{d^3k_p}{(2\pi)^3}\frac{d^3k_e}{(2\pi)^3}\frac{d^3k_\nu}{(2\pi)^3}\frac{d^3k_{N_1}}{(2\pi)^3}\frac{d^3k_{N_2}}{(2\pi)^3} \\ & (2\pi)^4\delta^{(4)}(k_p + k_e + k_{N_1} - k_n - k_\nu - k_{N_2}) \\ & f_p f_e f_{N_1}(1-f_n)(1-f_{N_2}) \\ & \left(s\frac{\sum|M|^2}{2^6 E_n^* E_p^* E_e E_\nu E_{N_1}^* E_{N_2}^*}\right),\end{aligned} \tag{3.31}$$

where $s = 1/2$ is a symmetry factor to account for identical particles. These are obtained using the matrix element from Ref. [2, 126] and using the Fermi surface approximation to simplify the phase space integral. For details see Appendix B of [67].

3.5 Results

We now present numerical results for the quantities described in Sec. 3.2. We perform all the computations in the isothermal regime: see Sec. 3.6 for further discussion of this assumption.

3.5.1 Isospin chemical potential

To calculate linear-response isospin equilibration properties such as the relaxation rate or bulk viscosity one needs to perturb around the equilibrium state. i.e., the state in which the net rate of isospin creation is zero. As noted in Sec. 3.1, at nonzero temperature this requires a nonzero isospin chemical potential, $\mu_I^{\rm eq}$ (Eq. (3.1)). Its value is negative because thermal corrections enhance electron capture more than neutron decay, so to restore the balance between these rates we need a chemical potential that reduces the proton fraction: this suppresses electron capture by reducing the proton population and enhances neutron decay by adding more occupied neutron states.

In Fig. 3.1 we show how $-\mu_I^{\rm eq}$ varies with density and temperature for our two exemplary equations of state, IUF and QMC-RMF3. The plot shows contours labeled by their value of $-\mu_I^{\rm eq}$. As discussed in Refs. [73, 67] $\mu_I^{\rm eq}$ tends to zero as $T \to 0$ which is why it was neglected in previous treatments of bulk viscosity in neutron stars. However, as the temperature rises above about 1 MeV, it becomes non-negligible. Note that for IUF, which has a direct Urca threshold at $n_B \approx 4n_0$, $\mu_I^{\rm eq}$ is enhanced near the threshold density. This is because thermal blurring of the Fermi surfaces becomes more important close to threshold, and opens up phase space for the electron capture process more than it does for neutron decay [73, 67]; this imbalance is the reason for a nonzero $\mu_I^{\rm eq}$.

3.5.2 Isospin Relaxation Rate

Fig. 3.2 shows how the isospin relaxation time $\tau = 1/\gamma_I$ (3.10) depends on density and temperature for our two reference equations of state, IUF (left) and QMC-RMF3 (right). We have shaded the range of density and temperature where relaxation occurs on the timescale relevant for mergers, 0.1 ms to 25 ms. The thick contour shows where $\gamma_I = 2\pi \times 1\,\text{kHz}$,

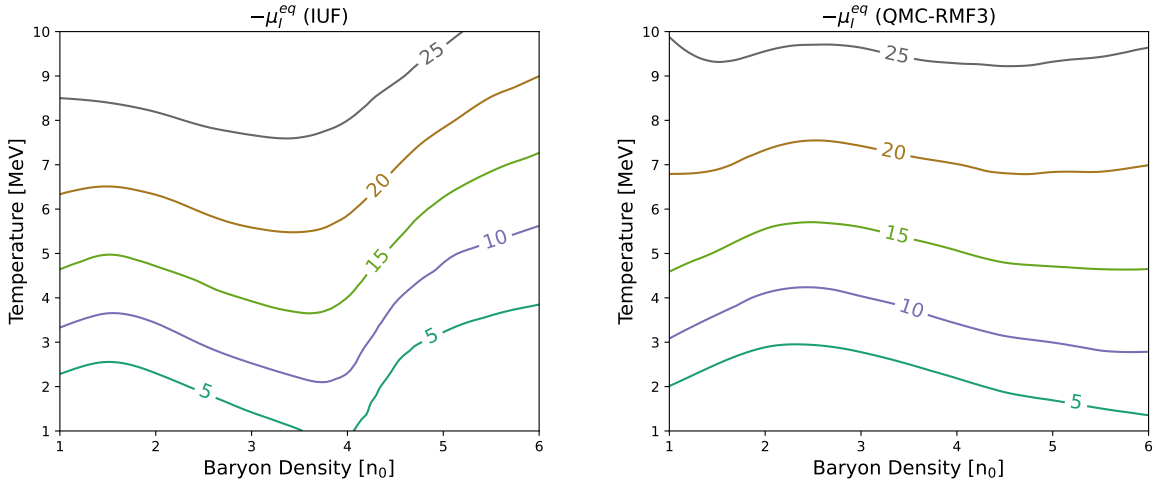

Fig. 3.1: Density and temperature dependence of $-\mu_I^{\rm eq}$, the isospin chemical potential in isospin equilibrium (Eq. (3.1)), for the IUF equation of state (left panel) and QMC-RMF3 (right panel); $-\mu_I^{\rm eq}$ rises with temperature because it arises from thermal blurring of the Fermi surfaces (see text). For IUF at low temperatures it is also influenced by the direct Urca threshold at $n_B \approx 4n_0$.

which as we will see below is where the bulk viscosity reaches a resonant maximum for a 1 kHz oscillation. If there is material in a merger that lies in this density/temperature range and obeys our assumptions (such as neutrino transparency), then the relaxation of its proton fraction is occurs on a timescale that is comparable to that of the merger dynamics, indicating that the relaxation process should be included in simulations.

In regions where the equilibration time is much smaller than 0.1 ms equilibration happens so fast that one could use the approximation that the matter is always in isospin equilibrium. In regions where the equilibration time is much longer than 20 ms the equilibration process is slow, and the proton fraction of each fluid element could be approximated as being constant. Previous simulations of neutron star mergers have either investigated these extreme cases of instantaneous equilibration, or frozen composition [127] or only partly implemented the low density and low-temperature approximation to the Urca rates studied here [128, 129, 120, 130, 131].

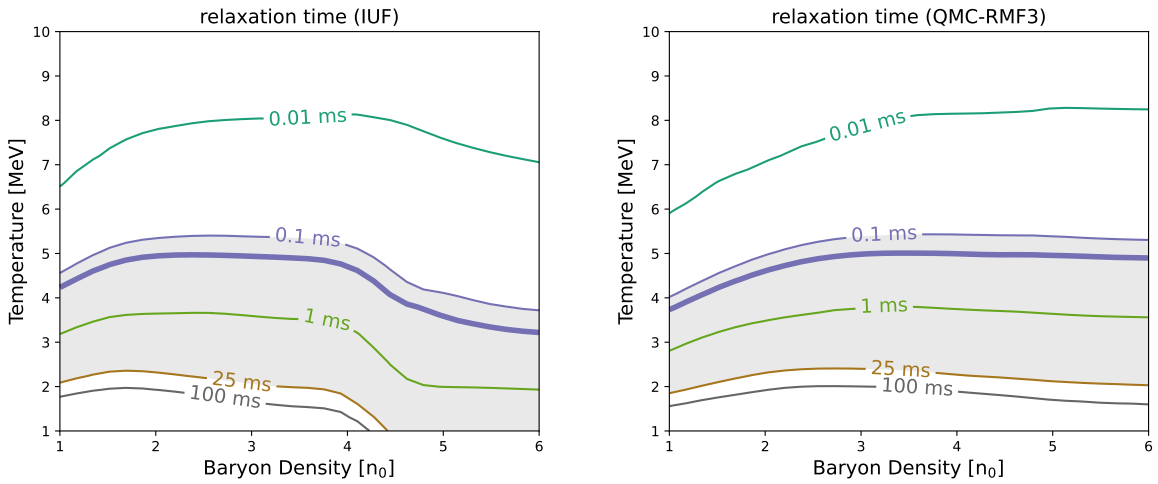

Fig. 3.2: Density and temperature dependence of the isospin relaxation time $\tau = 1/\gamma_I$ (Eq. (3.10)). The shaded region shows where the relaxation time is between 0.1 ms and 25 ms, i.e. comparable to the timescale of merger dynamics. The thick line shows the temperatures and densities where the bulk viscosity of a 1 kHz density oscillation would reach its maximum, i.e., where $\gamma_I = 2\pi \times 1\,\text{kHz}$ (Sec. 3.2.2).

Recently a first attempt has been made [132] to include both direct and modified Urca processes, calculated in the Fermi surface approximation, in the simulation. It was found that Urca processes affect the proton fraction of the fluid elements on the timescale of the merger dynamics.

For the IUF equation of state there is a noticeable feature in the relaxation time plot: relaxation becomes faster when the density reaches around $4n_0$. This is because IUF has a direct Urca threshold at this density. At densities above this threshold more phase space opens up and Urca rates, at a given temperature, are much faster than they are at densities below the threshold. Below the threshold density, the relaxation time is comparable to the merger timescale at temperatures of order 2 to 4 MeV. Above the threshold density, the relaxation time is comparable to the merger timescale at temperatures below 2 MeV.

For QMC-RMF3, the relaxation time depends only weakly on density. This is because there is no direct Urca threshold. Across the whole density range that we studied beta

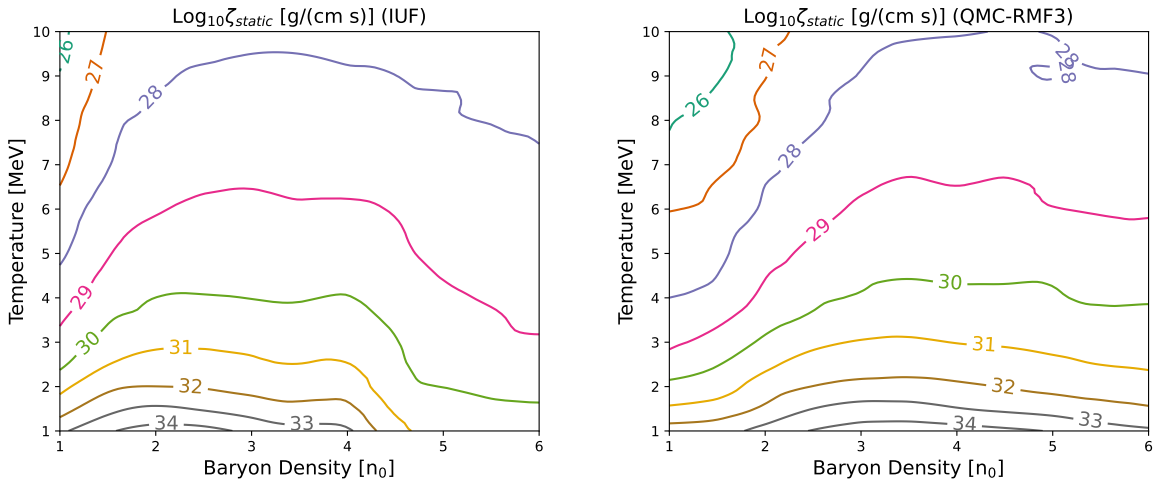

Fig. 3.3: Static (zero-frequency) bulk viscosity (3.21) for the IUF (left) and QMC-RMF3 (right) equations of state. The static bulk viscosity drops as temperature rises because it is inversely proportional to the relaxation rate.

equilibrium is determined by a balance between neutron decay (dominated by modified Urca) and electron capture (dominated by direct Urca) [73, 67]. Consequently, the region where the relaxation time is comparable to the merger timescale extends across the whole density range that we computed, for temperatures in the MeV-range.

Assuming that our reference EoSes are representative, Fig. 3.2 implies that if neutrino-transparent homogeneous matter is present in mergers then regions at $T \lesssim 5\,\mathrm{MeV}$ will likely be driven out of isospin equilibrium and regions at $T \sim 2$ to $5\,\mathrm{MeV}$ (the exact range depending on the EoS) will equilibrate on the timescale of the merger.

3.5.3 Bulk Viscosity and Damping Time

In Fig. 3.3 we show the density and temperature dependence of the static (zero-frequency) bulk viscosity ζ_0 (3.21). The plot shows contours of $\log_{10}(\zeta_0)$ where ζ_0 is in cgs units ($\mathrm{g\,cm^{-1}\,s^{-1}}$). The static bulk viscosity depends inversely on the relaxation rate, so it drops as the temperature rises, and at low temperatures we also see the effects of the direct Urca

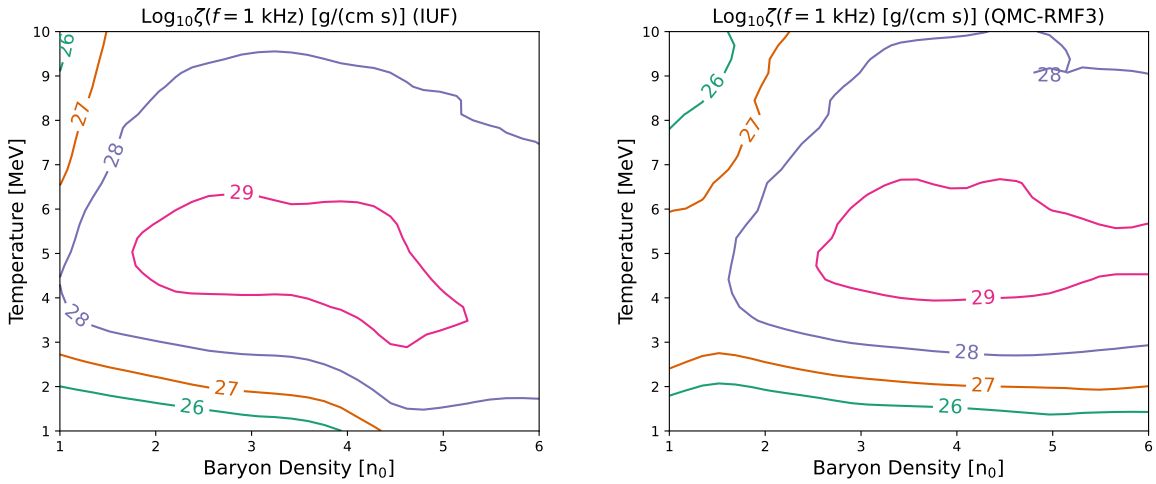

Fig. 3.4: Bulk viscosity at frequency $f = 1\,\mathrm{kHz}$ for the IUF (left) and QMC-RMF3 (right) equations of state. In both cases the resonant peak occurs where the relaxation rate passes through $\omega = 2\pi \times 1\,\mathrm{kHz}$, which occurs at $T \approx 5\,\mathrm{MeV}$.

threshold at $n_B \approx 4n_0$, as in Fig. 3.2.

From the isospin relaxation rate and the static bulk viscosity one can reconstruct the frequency-dependent bulk viscosity (Eq. (3.20)). Since density oscillations in neutron star mergers typically have frequencies in the kHz range, Fig. 3.4 shows the density and temperature dependence of bulk viscosity at angular frequency $\omega = 2\pi \times$ kHz.

As described in Sec. 3.2.2, we expect the bulk viscosity to reach a resonant maximum when the isospin relaxation rate $\gamma_I(n_B, T)$ coincides with the angular frequency ω of the density oscillation. The relaxation rate rises quickly with temperature since higher temperature opens up more phase space near the Fermi surfaces. We therefore expect the bulk viscosity to achieve its maximum value at the temperature where $\gamma_I(n_B, T) \approx \omega$. From Fig. 3.2 we see that for a 1 kHz density oscillation that temperature is around 5 MeV. This explains what we see in Fig. 3.4: the contours run roughly horizontally, with the bulk viscosity reaching a maximum at $T \approx 5\,\mathrm{MeV}$. At lower temperatures the system equilibrates so slowly that isospin is almost conserved: the proton fraction remains constant, and the system has a low

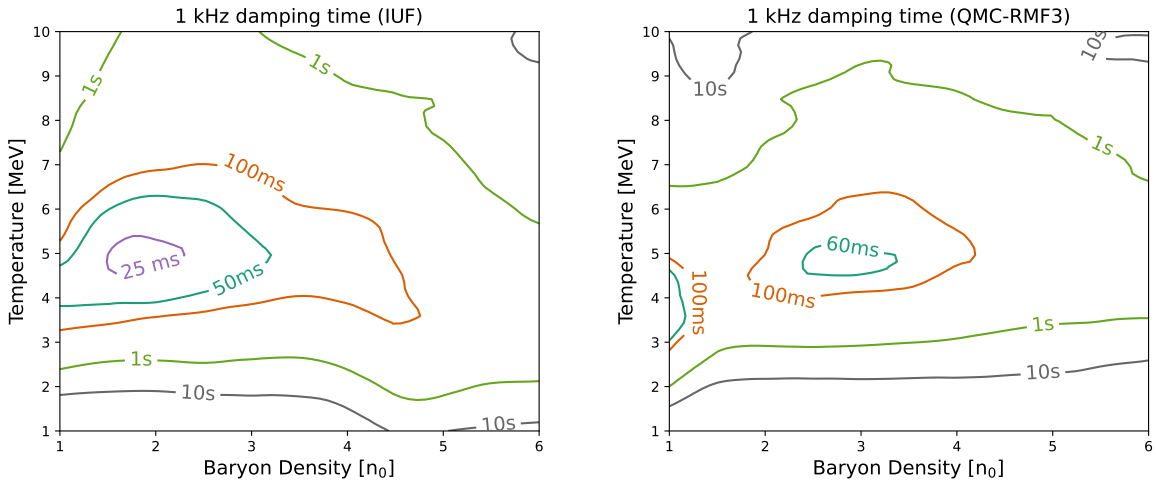

Fig. 3.5: Damping time for density oscillations of frequency 1 kHz as a function of density and temperature, for the IUF (left) and QMC-RMF3 (right) equations of state.

bulk viscosity. At higher temperatures where $\gamma_I \gg \omega$ the system equilibrates so quickly that there is little phase lag between pressure and density, and the bulk viscosity tends towards its static value ζ_0 (Fig. 3.21).

For the IUF EoS one can see the effect of the direct Urca threshold at $n_B \approx 4n_0$: below that density relaxation is slower (due to a lack of kinematically allowed phase space), and so a higher temperature is needed to bring the relaxation rate up to 1 kHz.

Comparing these to previous calculations that used nonrelativistic dispersion relations for the nucleons (e.g., Refs. [63], [85]), our resonance peaks are shifted to slightly higher temperatures for given densities. This is because in our models of nuclear matter the in-medium effective masses of the nucleons are much lower than the vacuum masses so the relativistic corrections are significant, decreasing the Urca rates and relaxation rates [67, 65], which means higher temperatures are required to achieve resonance ($\gamma_I = \omega$).

One physical manifestation of bulk viscosity is the damping of density oscillations. The

damping time for an oscillation of angular frequency ω is [85]

$$\tau_{\rm damp} = \frac{\kappa^{-1}}{\omega^2 \zeta(\omega)} \,, \tag{3.32}$$

where the incompressibility is

$$\kappa^{-1} \equiv n_B \left. \frac{\partial p}{\partial n_B} \right|_{x_I, T} \,. \tag{3.33}$$

Since this paper focuses on isothermal density oscillations we use the isothermal compressibility.

Fig. 3.5 shows how the damping time depends on density and temperature for IUF (left) and QMC-RMF3 (right). We expect that in density/temperature regions where the damping time is in the tens of milliseconds range, bulk viscosity will have a significant impact on density oscillations during the merger.

The key features of this plot are: (1) the temperature dependence of the damping time is mainly determined by that of the bulk viscosity, so the damping time is shortest when the bulk viscosity (Fig. 3.4) is largest, i.e. at $T \sim 5\,\mathrm{MeV}$; (2) the density dependence of the damping time also roughly follows that of the bulk viscosity, but damping is slowed at high densities by the growth of the incompressibility: oscillations then store more energy and so take longer to decay; (3) the shortest damping times are short enough so that bulk viscous damping is relevant on merger timescales.

These results are comparable to those obtained in Ref. [65], which used different models for nuclear matter and used the low-temperature approximation for beta equilibrium, $\mu_I^{\rm eq} = 0$.

The data for the plots shown in this section are available at `https://github.com/zzz-new/Physics_MUSES_Beta_Equilibration` or `https://gitlab.com/ahaber/npe-bulkviscosity`. The code used to develop the QMC-RMF3 model and to solve the mean-field equations for

both our models of nuclear matter can be found at `https://gitlab.com/ahaber`. The code for calculating Urca rates and isospin equilibration properties will be made public as part of the MUSES framework `https://musesframework.io/`.

3.6 Conclusions

We have analyzed the isospin equilibration properties of neutrino-transparent nuclear (npe) matter in the temperature and density range that is relevant to neutron star mergers. Our analysis includes corrections to the isospin equilibrium condition $\mu_n = \mu_p + \mu_e$ which arise at $T \gtrsim 1\,\mathrm{MeV}$. We find that at temperatures of order 2 to 5 MeV the isospin relaxation time, i.e., the timescale on which the proton fraction relaxes to its equilibrium value, is comparable to the timescale of the density oscillations that occur immediately after the merger. At lower temperatures, isospin relaxes more slowly, and at higher temperatures, it relaxes faster. For a 1 kHz density oscillation this leads to a resonant peak in the bulk viscosity at $T \sim 5\,\mathrm{MeV}$, when the relaxation rate matches the frequency. This causes damping of such a density oscillation on the timescale of the merger, providing strong motivation to include isospin relaxation dynamics in merger simulations.

There are many directions in which further work is needed to elucidate the dynamics of isospin under merger conditions. (1) Our most significant assumption is neutrino transparency, which is valid in the limit of a long mean free path for the neutrinos. The behavior of neutrinos in mergers is more complicated, with an energy-dependent mean free path that interpolates between the transparent and trapped regimes [120]. It will be important to develop tools that can handle this scenario. (2) Our calculation of the $n \rightleftharpoons p$ rate is based on the standard separation between the direct Urca and modified Urca contributions which are added to give the total rate. Our treatment of direct Urca is full and rigorous, including

the entire weak interaction matrix element and integrating the rate over the whole phase space, but the standard expression for the modified Urca rate uses crude approximations, and improving on it is a natural next step [4]. (3) We performed our calculation in the isothermal regime, assuming that the thermal relaxation rate is faster than the dynamical timescales. It would be straightforward to perform a parallel calculation in the adiabatic regime, but previous analyses [73, 65] have found that this does not change the results significantly. This is because the temperatures involved are lower than the Fermi energies of the relevant particles, so the entropy contribution to the pressure is generally a small correction. In reality thermal conduction in mergers is likely to interpolate between the isothermal and adiabatic regimes, again because of the role of neutrinos, which can have a long mean free path depending on their energy and the ambient density and temperature [55], so they likely dominate the thermal conductivity. (4) Our calculation of bulk viscosity and the damping time for oscillations assumes linear response ("subthermal bulk viscosity") where the amplitude of the oscillations is small in the sense that the departure of the chemical potentials from equilibrium is much less than the temperature. Simulations indicate that in the first few milliseconds after merger there are large-amplitude oscillations, for which the suprathermal bulk viscosity [133, 134] would be relevant. Note that if the Urca rate equation (3.6) is explicitly included in a merger simulation code then the resulting evolution will naturally incorporate the physical effects, including the subthermal and suprathermal bulk viscosity. (5) At merger densities we expect nuclear matter to contain muons, which we neglected in this work. Including them opens up additional equilibration channels ($n \rightleftharpoons p\,\mu$ and purely leptonic processes) leading to a more complicated picture with multiple relaxation times [65]. (6) A natural next step is to compare our results with the isospin equilibration properties of more exotic forms of matter, such as hyperonic [135] or quark matter [136, 137, 92, 138, 139].

In conclusion, this paper provides the most complete treatment to date of the physics

of isospin equilibration in homogeneous neutrino-transparent nuclear matter, in the density and temperature range that is relevant to neutron star mergers. Our calculation of the isospin relaxation rate and related phenomena such as bulk viscosity and the damping of density oscillations provides a guideline for merger simulators to assess which approximations for isospin equilibration are appropriate at a given density and temperature, and when an explicit implementation of the relaxation process is required.

Chapter 4

A Unified Approach to Urca Processes

This chapter is based on several unpublished results.

4.1 Introduction

As shown in the previous chapters, modified Urca has been commonly treated with a lot of approximations [2, 3]. Yakovlev et al. [3] treat nucleons as non-relativistic particles, neglect electron momentum, and average over neutrino orientation. Friman and Maxwell [2] have made further approximations as described in [3] Sec.3.4.(b). One of the crude treatment to the internal propagator (indicated in Fig. 4.1) involves approximating it as $\frac{1}{\mu_e}$. Shternin et al. [4] have improved the treatment of the internal propagator using

$$G = \frac{1}{\epsilon - E_k}\,, \tag{4.1}$$

where ϵ is the energy of the off-shell particle and E_k is the dispersion relation of the particle. However, this leads to an unphysical divergence of the rate when close to the direct Urca threshold, which will be discussed in Sec. 4.2. In the work done by Shternin et al., nucleons are treated as non-relativistic particles, which is not a good approximation above 2 to 3 n_0

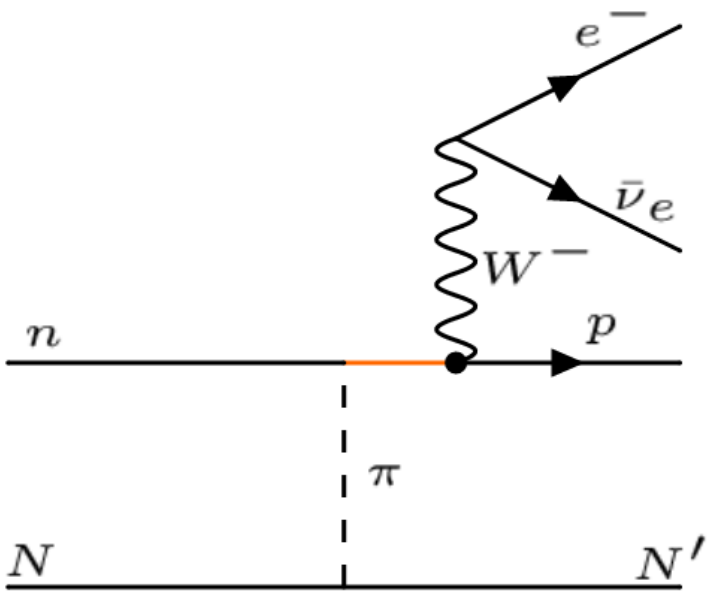

Fig. 4.1: Modified Urca Feynman diagram. The internal propagator is highlighted in orange. It is commonly approximated as $1/\mu_e$, which has been widely used [2, 3].

in RMFs (see discussions in Chap. 2). Therefore, a calculation with consistent relativistic treatment has been presented.

Before solving the divergence issue, in Sec. 4.3, we present a new relativistic calculation of the modified Urca processes by doing full phase-space integrals. This is among the first calculations that allow modified Urca to go beyond Fermi surface approximation and the first full phase-space rate calculation for modified Urca. More study in this section is ongoing.

Back to the divergence issue, we added a width to the internal propagator and showed that this approach solves the unphysical divergence, which is discussed in Sec. 4.4.

Up until the point of writing this thesis, direct Urca and modified Urca have been calculated separately. In Sec. 4.5, a first try towards a framework of unifying all Urca processes is presented. This is also among the first calculations that consistently allow modified Urca to go beyond Fermi Surface approximation. It is more efficient because instead of an 11-dim

integral, only a 6-dim integral is necessary.

4.2 Improved Modified Urca

4.2.1 The Modified Urca Rates and the Angular Averaged Matrix Element

To calculate the rate, we start from Fermi's Golden rule, as discussed in Chap. 2 and Chap. 3,

$$\Gamma_{mU,nd} = \int \frac{d^3k_n}{(2\pi)^3}\frac{d^3k_p}{(2\pi)^3}\frac{d^3k_e}{(2\pi)^3}\frac{d^3k_\nu}{(2\pi)^3}\frac{d^3k_{N_1}}{(2\pi)^3}\frac{d^3k_{N_2}}{(2\pi)^3}(2\pi)^4\delta^{(4)}(k_n + k_{N_1} - k_p - k_e - k_\nu - k_{N_2}) \\ f_n f_{N_1}(1-f_p)(1-f_e)(1-f_{N_2})\Big(s\frac{\sum|M|^2}{2^6 E_n^* E_p^* E_e E_\nu E_{N_1}^* E_{N_2}^*}\Big). \tag{4.2}$$

In this section, we still carry out the calculation under Fermi surface approximation. The details about the modified Urca Fermi surface approximation have been laid out in the Appendix. C, now with a different matrix element because of implementing a different propagator. The first step of Fermi surface approximation involves separating the integral into two parts, i.e. the angular integral and the energy integral. In order to carry out the angular integral analytically described in [89], we need to do an angular averaging of the matrix element $\langle|M|^2\rangle$ so that they are independent of the angles. The angular-averaged matrix element is calculated as the following,

$$\begin{aligned}\langle|M|^2\rangle &= \frac{I_M}{I_N} \\ &= \frac{\int(\prod_{i=i}^6 d^3k_i\delta(|\vec{k_i}| - k_i))\delta^{(3)}(\vec{k_{in}} - \vec{k_{out}})|M|^2}{\int(\prod_{i=i}^6 d^3k_i\delta(|\vec{k_i}| - k_i))\delta^{(3)}(\vec{k_{in}} - \vec{k_{out}})}\,.\end{aligned} \tag{4.3}$$

To calculate the I_M integral weighted by the matrix element, we setup a coordinate system

of the momentum transfers, and we label the incoming neutron by 1, outgoing proton by 2, incoming spectator by 3, and outgoing spectator by 4. We have

$$\vec{p_1} = \vec{k_1} - \vec{k_3}\,, \tag{4.4}$$

$$\vec{p_2} = \vec{k_4} - \vec{k_2}\,, \tag{4.5}$$

$$\vec{p_3} = \vec{k_2}\,, \tag{4.6}$$

$$\vec{p_4} = \vec{k_4}\,, \tag{4.7}$$

$$\vec{p_5} = \vec{k_e}\,. \tag{4.8}$$

Therefore, the coordinate system of the momentum transfers is

$$\vec{p_1} = \vec{p_2} + \vec{p_5}\,, \tag{4.9}$$

$$\vec{p_2} = p_2(0, 0, 1)\,, \tag{4.10}$$

$$\vec{p_3} = p_3(\sqrt{1 - z_3^2}, 0, z_3)\,, \tag{4.11}$$

$$\vec{p_4} = p_4(\sqrt{1 - z_4^2}\,\cos\phi_4, \sqrt{1 - z_4^2}\,\sin\phi_4, z_4)\,, \tag{4.12}$$

$$\vec{p_5} = p_5(\sqrt{1 - z_5^2}\,\cos\phi_5, \sqrt{1 - z_5^2}\,\sin\phi_5, z_5)\,. \tag{4.13}$$

After the angular-averaged matrix element is calculated, the remaining parts of the integration (both angular and energy integrals) are the same as described in Appendix. C. A notice to the angular integral that the neutrino 3-momentum is usually neglected so that $d\Omega$ can be integrated out first, leaving an angular integral with only 5 particles.

In this modified Urca calculation, we include 4 diagrams, same as in [4]. Fig. 4.2 shows the 2 direct diagrams. For each direct diagram, there is also a corresponding exchange diagram. The difference between the 2 direct diagrams comes from whether the weak vertex happens

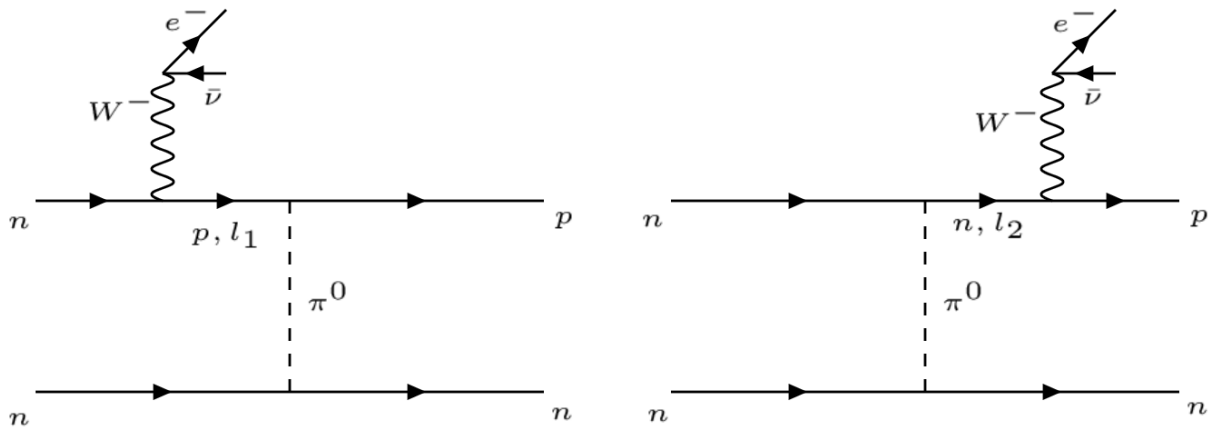

Fig. 4.2: Modified Urca Feynman diagrams [4]. For each direct diagram, there is also a corresponding exchange diagram where the incoming external legs of the direct diagram are exchanged.

before or after the strong vertex. The amplitude is calculated as the sum of the 2 direct diagrams minus the sum of the 2 exchange diagrams, i.e. $M = (M_{1D} + M_{2D}) - (M_{1E} + M_{2E})$. The difference between our modeling and the Shternin et al. modeling of the nucleon-nucleon interaction is that we use one-pion exchange (OPE) [2, 3] instead of complicated nucleon-nucleon interactions. Besides, in our calculation, we use a full Fermion propagator $\frac{i}{\not{k}-m}$, as opposed to using a non-relativistically approximated one.

4.2.2 Results

Fig. 4.3 shows the result of the modified Urca calculation with angular averaged matrix element under Fermi surface approximation. We also observed an enhancement from all densities below the threshold and an unphysical divergence around the threshold. As discussed in [4], the enhancement is mainly due to a better treatment of the internal propagator (there is also a contribution from a more complete angular-averaged matrix element).

We also observed the appearance of the divergence around the threshold. With gradually

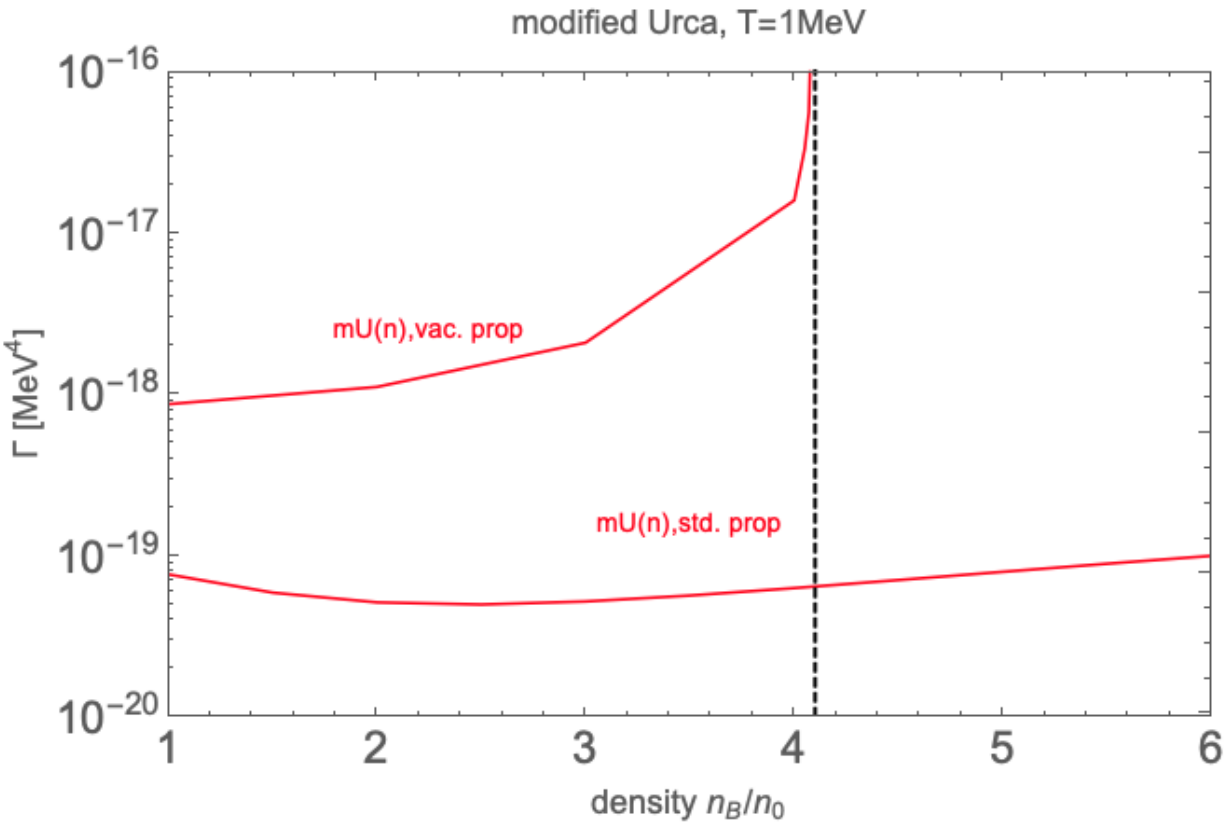

Fig. 4.3: Modified Urca rates under Fermi surface approximation. "Vacuum propagator" stands for the relativistic bare Fermion propagator, instead of a non-relativistic Fermion propagator.

increasing density, the momentum deficit for direct Urca is getting smaller. At the direct Urca threshold, $k_{Fn} = k_{Fp} + k_{Fe}$, no extra momentum is necessary for direct Urca to happen, and the spectator would not need to participate in the reaction anymore. At this point, the internal nucleon goes on-shell, $k^2 = m^2$, which means that its energy and momentum can be connected via the dispersion relation, i.e. $\epsilon = E_k$, where $E_k = \sqrt{m^{*2} + k^2} + U$ for RMF models. Therefore, the propagator diverges, hence the rate.

4.3 Modified Urca with Full Phase Space Integral

Before we discuss how to solve the divergence issue, we take further steps to improve the modified Urca calculations. In this section, we present a full phase space integration, as opposed to Fermi surface approximation, thus we do not need to perform angular-averaging of the matrix element anymore.

4.3.1 Method

We still start from the rate expression

$$\begin{aligned}
\Gamma_{mU,nd} = & \int \frac{d^3k_n}{(2\pi)^3}\frac{d^3k_p}{(2\pi)^3}\frac{d^3k_e}{(2\pi)^3}\frac{d^3k_\nu}{(2\pi)^3}\frac{d^3k_{N_1}}{(2\pi)^3}\frac{d^3k_{N_2}}{(2\pi)^3}(2\pi)^4\delta^{(4)}(k_n + k_{N_1} - k_p - k_e - k_\nu - k_{N_2}) \\
& f_n f_{N_1}(1-f_p)(1-f_e)(1-f_{N_2})\Big(s\frac{\sum|M|^2}{2^6 E_n^* E_p^* E_e E_\nu E_{N_1}^* E_{N_2}^*}\Big) \\
& = \frac{(2\pi)^4}{(2\pi)^{18}}\int d\Omega_n d\Omega_p d\Omega_e d\Omega_\nu d\Omega_{N1} d\Omega_{N2} dk_n dk_p dk_e dk_\nu dk_{N1} dk_{N2} \\
& \delta((E_n + E_{N1}) - (E_p + E_e + E_\nu + E_{N2}))\delta^{(3)}((\vec{k_n} + \vec{k_{N1}}) - (\vec{k_p} + \vec{k_e} + \vec{k_\nu} + \vec{k_{N2}})) \\
& f_n f_{N_1}(1-f_p)(1-f_e)(1-f_{N_2})\Big(s\frac{\sum|M|^2}{2^6 E_n^* E_p^* E_e E_\nu E_{N_1}^* E_{N_2}^*}\Big)\,. \qquad (4.14)
\end{aligned}$$

We integrate out the momentum delta function first, then use the fact that neutrinos are ultra-relativistic, $E_\nu = |\vec{k_\nu}|$, we get

$$\begin{aligned}
\Gamma_{mU,nd} = & \frac{1}{(2\pi)^{14}}\int d\Omega_n d\Omega_p d\Omega_e d\Omega_\nu d\Omega_{N1} d\Omega_{N2} dk_n dk_p dk_e dk_\nu dk_{N1} dk_{N2} \\
& \delta\Big((E_n + E_{N1}) - (E_p + E_e + E_{N2}) - |(\vec{k_n} + \vec{k_{N1}}) - (\vec{k_p} + \vec{k_e} + \vec{k_{N2}})|\Big) \\
& f_n f_{N_1}(1-f_p)(1-f_e)(1-f_{N_2})\Big(s\frac{\sum|M|^2}{2^6 E_n^* E_p^* E_e E_\nu E_{N_1}^* E_{N_2}^*}\Big)\,. \qquad (4.15)
\end{aligned}$$

The coordinate system is set up as

$$\vec{k}_n = k_n(0, 0, 1)\,, \tag{4.16}$$

$$\vec{k}_p = k_p(\sqrt{1 - z_p^2}, 0, z_p)\,, \tag{4.17}$$

$$\vec{k}_e = k_e(\sqrt{1 - z_e^2}\,\cos\phi_e, \sqrt{1 - z_e^2}\,\sin\phi_e, z_e)\,, \tag{4.18}$$

$$\vec{k}_{N1} = k_{N1}(\sqrt{1 - z_{N1}^2}\,\cos\phi_{N1}, \sqrt{1 - z_{N1}^2}\,\sin\phi_{N1}, z_{N1})\,, \tag{4.19}$$

$$\vec{k}_{N2} = k_{N2}(\sqrt{1 - z_{N2}^2}\,\cos\phi_{N2}, \sqrt{1 - z_{N2}^2}\,\sin\phi_{N2}, z_{N2})\,, \tag{4.20}$$

and we define the argument of the energy delta function as $g(z_p) = E_\nu - |\vec{k_\nu}|$. Then the energy-conserving delta function becomes

$$\delta(g(z_p)) = \frac{\delta(z_p - z_{p0})}{|g'(z_p)|_{z_p = z_{p0}}}\,, \tag{4.21}$$

where $g(z_{p0}) = 0$.

This calculation is different from [140] in several ways:

- They calculate the neutrino opacity, whereas we calculate the full 11-dim rate
- They use non-relativistic approximations for the nucleons, while we use fully relativistic calculations. We emphasized in Chap. 2 that in RMF, nucleons become relativistic above 2 - 3 n_0.

4.3.2 Results

In our calculation, we empirically observed that the interference terms are negligible compared to the non-interference terms, which is also observed in [4] for modified Urca processes.

Fig. 4.4 shows the result of a full phase-space, fully relativistic calculation. For now, we

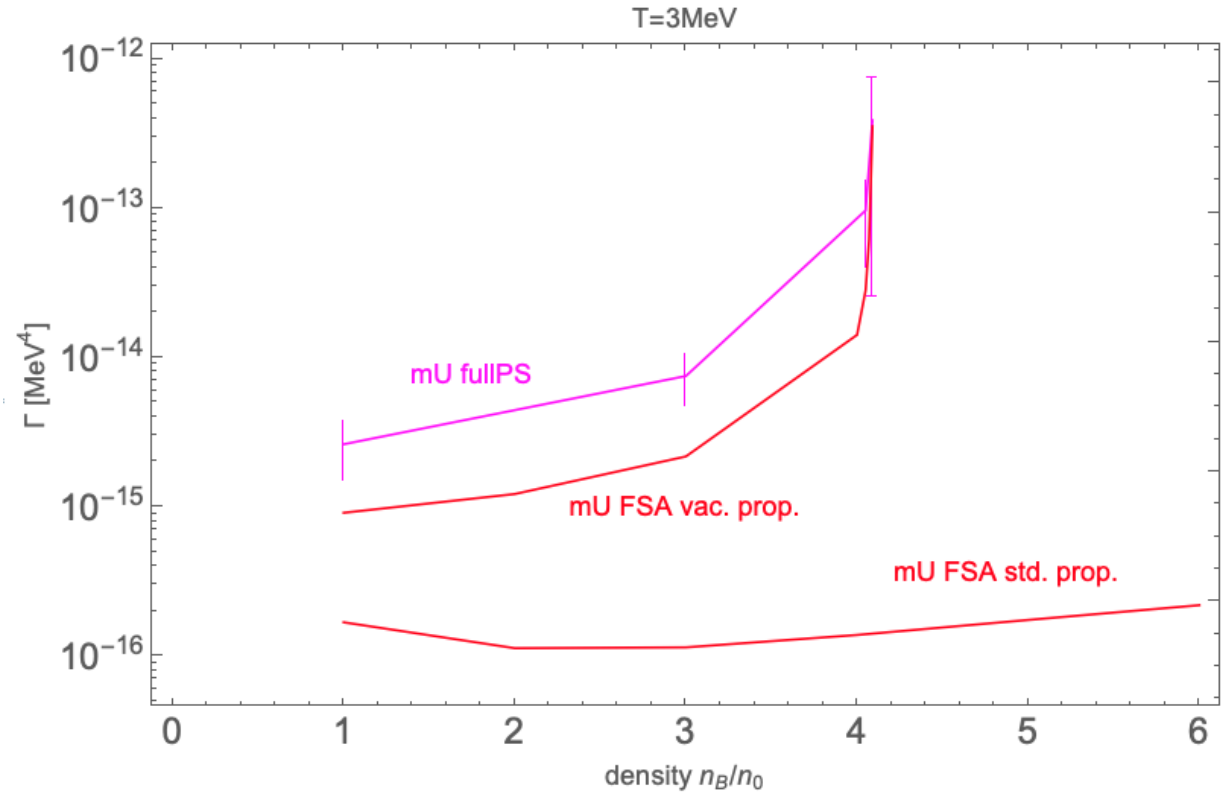

Fig. 4.4: Modified Urca rate calculated from a full phase-space integral. All particles are treated relativistically.

only included 2 diagrams rather than all 4. The corresponding Fermi surface approximation calculation with vacuum propagator in this plot also included only 2 diagrams in order to compare. The plot also compares the rate with different treatments to the modified Urca processes. The plot confirms the enhancement of the modified Urca rate at all densities, as discussed in [4, 140]. The full phase space rate is larger than the Fermi surface approximation rate by a factor of 2 or so. Fermi surface approximation and angular-averaged matrix element should mainly contribute to the difference. The enhancement may lead to some impact in physics such as faster cooling [4], bulk viscosity peak shift [141], etc.

Under Fermi surface approximation, neutrino energies are on the order of the tempera-

ture, so they are negligible, and the cold beta equilibrium is $\mu_n = \mu_p + \mu_e$. In this equilibrium, neutron decay and electron capture are the reverse processes of each other, so the two rates are equal. Since this method goes above Fermi surface approximation, we plan to check if the two rates are equal under the cold beta equilibrium. If not, we could correct the beta equilibrium as we did in Chap. 2.

4.4 Solving the Divergence by Adding a Width to the Propagator: A First Study

We have improved the modified Urca calculations in the previous two sections. Now, we go back to the unphysical divergence issue in the rate.

4.4.1 Method

The goal of the first attack on this problem is to solve the unphysical divergence issue. We improve the in-medium nucleon propagator by adding a self-energy. We expect that with this form of the propagator, the infinity issue can be solved and the modified Urca process will show a smooth behavior around the direct Urca threshold. This is because the imaginary part of the denominator of the propagator pushes the pole above the real axis, and by integrating over the real axis, the pole will not be encountered.

From the physics point of view, we have added an imaginary part to the mass. The quantum mechanical analog is that of a wave function

$$\psi(t) \propto e^{i\omega t - \Gamma t} = e^{i(\omega + i\Gamma)t} \,. \tag{4.22}$$

Then, the probability of finding the particle with this wave function decays exponentially,

$$|\psi(t)|^2 \propto e^{-\Gamma t} \,. \tag{4.23}$$

Thus, having an imaginary part of the mass or the energy indicates that the particle is unstable.

Back to the problem. To dress the bare propagator with a width, we start with Dyson's equation, which states that

$$G = G^{(0)} + G^{(0)}\Sigma G^{(0)} + ... = \frac{G^{(0)}}{1 - \Sigma G^{(0)}} \,, \tag{4.24}$$

where G is the full or dressed propagator, $G^{(0)}$ is the bare propagator, Σ is the self-energy. For a fermion, the bare propagator is

$$G^{(0)} = \frac{i}{\not{k} - m} \,. \tag{4.25}$$

Therefore, the dressed propagator is

$$G = \frac{i}{\not{k} - (m + i\Sigma)} \,. \tag{4.26}$$

4.4.2 Results

Fig. 4.5 shows the effects when including the width in the internal particle propagator. Without the width, the bare relativistic propagator reproduced the unphysical divergence around the threshold. When a finite width of 1 MeV is included, which is a reasonable value from [142], we observed that the modified Urca becomes smooth around the threshold. As

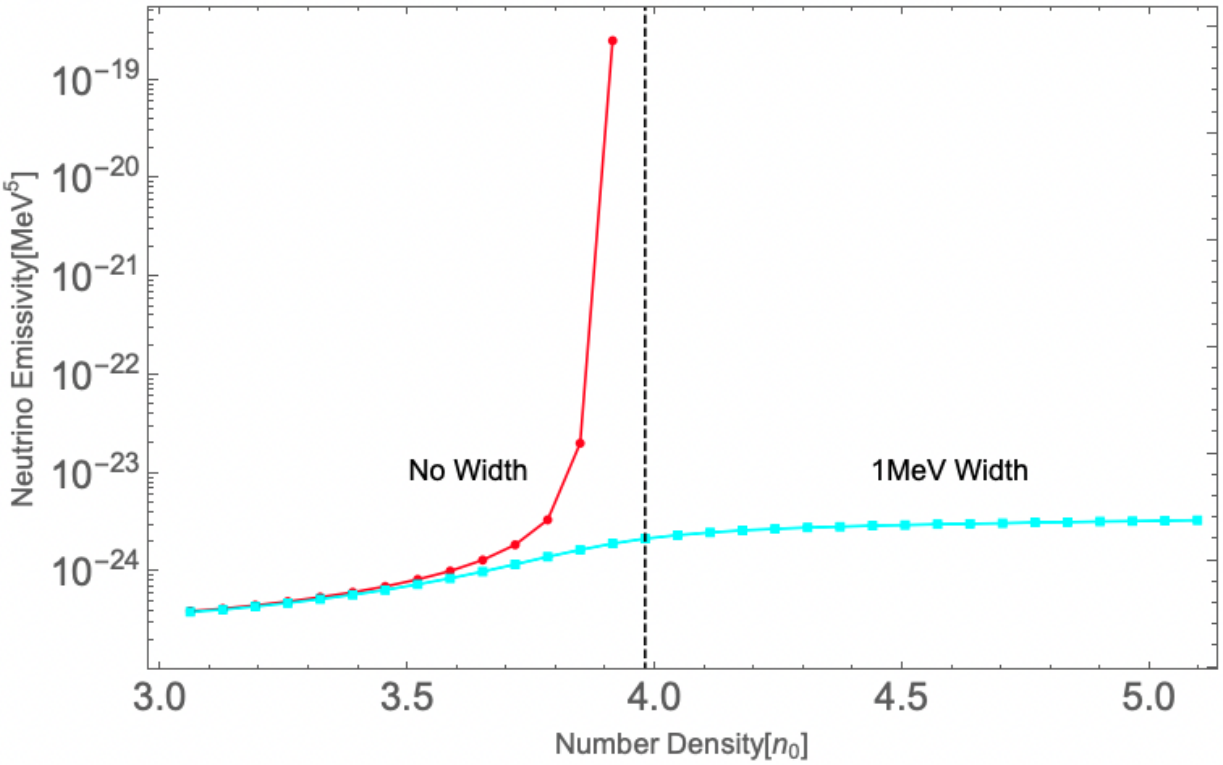

Fig. 4.5: Modified Urca neutrino emissivity with and without a width in the internal relativistic propagator at $T = 1\,\mathrm{MeV}$. We use IUF to model the nuclear matter.

we have discussed before, the imaginary part of the self-energy pushes the pole away from the real axis, thus avoiding the divergence.

In our exploration, we tried different values of the width and found that below 3.5 n_0 in IUF, the emissivities with and without a width overlap. At densities from 3.5 n_0 to the threshold, the emissivity without width may be overestimated from the observation of the divergence. From 3.5 n_0 to the treshold, in order to get the correct rate, one needs to calculate the imaginary part of the self-energy as the width. For now, the self-energy is taken only as a parameter. The nucleon scattering processes are supposed to contribute to the self-energy, and the calculation for the self-energy would be left for future works.

Notice that this plot is the neutrino emissivity (i.e. rate weighted by the neutrino energy). The nucleons are treated non-relativistically. This work was done in 2020, and most recently, Suleiman et al. [140] have used the same approach adding a width to the internal propagator to solve the divergence issue and treating width as a parameter to vary.

4.5 A Unified Approach of Urca Processes

In the previous section, we solved the divergence issue by adding a width to the internal propagator, and the modified Urca becomes smooth around the direct Urca threshold. Now, in this section, we tackle this problem from a different perspective. Not only has the modified Urca avoided the divergence, but also it smoothly transits into direct Urca. This is our approach to a unified framework of Urca processes.

4.5.1 The Idea of Unified Urca

When we add a width to the internal nucleon propagator, we have successfully solved the divergence, and the modified Urca is smooth around the threshold. Then we can step forward for a more advanced question, that is can we calculate some kind of sum of the Urca processes, where it naturally and smoothly transits from modified Urca into direct Urca processes around the threshold?

An idea is that we can think of direct Urca as some first-order expansion and modified Urca as some higher-order expansion and so on. To realize this idea, we construct a neutrino self-energy diagram, shown in Fig. 4.6, where we dressed the neutron propagator. The proton propagator could also be dressed, but for now, let us leave it as a bare propagator.

To understand this diagram, we can expand the dressed propagator using Dyson's equation, and then this diagram is equivalent to the sum of Fig. 4.7, Fig. 4.8, and ***all*** higher-order

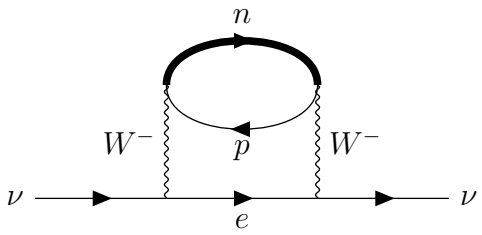

Fig. 4.6: Neutrino self-energy diagram.

terms.

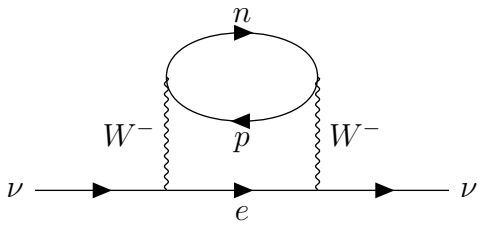

Fig. 4.7: Neutrino self-energy diagram with the bare nucleon propagator.

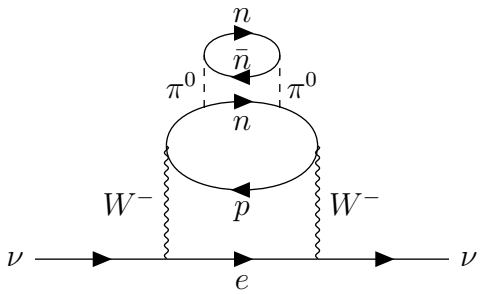

Fig. 4.8: Second order expansion of the neutrino self-energy diagram.

To connect these diagrams to the Urca processes, we recall the Cutkosky cutting rules [143], which states that the imaginary part of the self-energy diagrams can be calculated by cutting the internal lines of the loops and putting virtual particles on-shell. Then the the imaginary part of the self-energy can be calculated via the related tree-level diagram. In our case, the imaginary part of the self-energy in Fig. 4.7 gives direct Urca, the imaginary part of the self-energy in Fig. 4.8 gives modified Urca. Therefore, by calculating the imaginary

part of the neutrino self-energy diagram with dressed nucleon propagators, we effectively calculated ***all*** Urca processes.

4.5.2 An Ansatz of an Unstable Particle Propagator

In real-time thermal field theory, the degree of freedom is doubled, and the particle propagator is represented by a matrix [144, 145, 146, 147, 148]. The G_{11} component of the thermal propagator for fermions is

$$iG_{11}(k) = \frac{i}{\not{k} - m + i\epsilon} - n_F(k)(\not{k} + m)\, 2\pi\delta(k^2 - m^2)\,, \tag{4.27}$$

where the component propagator consists of a usual zero-temperature part and a thermal part, with n_F being the Fermi-Dirac distribution. The components are related, so we only show the relevant changes in G_{11}, and then changes can be made to other components accordingly.

As discussed in [144], the on-shell delta function is obtained from the spectral density of a fermion when $\epsilon \to 0$. We conjecture that the correct general expression is

$$iG_{11}(k) = \frac{i}{\not{k} - (m - i\Gamma/2)} - n_F(k)\rho_{uF}(k)\,, \tag{4.28}$$

where $\rho_{uF}(k)$ is the spectral density function for an unstable fermion, defined analogously to the one for scalar particles,

$$\rho_{\rm uF}(k) = i(G_{\rm uF}(k) - G^*_{\rm uF}(k))\ , \tag{4.29}$$

in terms of the non-thermal propagator for an unstable fermion

$$G_{\rm uF}(k) = \frac{\not{k} + m - i\Gamma/2}{k^2 - (m - i\Gamma/2)^2} \ . \tag{4.30}$$

To test our conjecture, we look at the limit of small Γ, where (4.28) should reduce to (4.27). We substitute (4.30) in to (4.29), and assume that the particle width is fairly small, $\Gamma \ll m$, so the function is sharply peaked near $k^2 = m^2$, which means we can also assume $(k^2 - m^2) \ll m^2$. In this approximation we find

$$\rho_{uF}(k) \approx (\not{k} + m)\, 2\pi R(k^2 - m^2) \tag{4.31}$$

$$\text{where} \quad R(k^2 - m^2) \equiv \frac{1}{\pi} \frac{m\Gamma}{(k^2 - m^2)^2 + m^2\Gamma^2} \ . \tag{4.32}$$

$R(k^2 - m^2)$ is a regulated delta function, sharply peaked at $k^2 = m^2$ and properly normalized

$$\int_{-\infty}^{\infty} R(x)dx = 1 \, . \tag{4.33}$$

In the limit $\Gamma \to 0$, $R(k^2 - m^2) \to \delta(k^2 - m^2)$. This confirms that in the limit of small width Γ, our conjectured expression (4.28) reduces to the expression (4.27). If our conjecture is correct, the propagator for a particle of finite (but not too large) width is given by (4.28) and (4.31).

4.5.3 Formulation

We start from a self-energy calculation established in [145] Sec. 3, and we should be able to get the same rate expression discussed in Chap. 2 and Chap. 3, which we will show below.

The direct Urca calculation is given by

$$\Gamma = -\left(\frac{G_F\, cos\theta_c}{\sqrt{2}}\right)^2 \int \frac{d^3k_e}{(2\pi)^3(2E_e)} \int \frac{d^3k_\nu}{(2\pi)^3(2E_\nu)}\, d^4k_W \delta^{(4)}(k_e + k_\nu - k_W)(1-f_\nu)(1-f_e)$$
$$g_B(k_W^0)\, \mathrm{Tr}\Big[\gamma^\mu(1-\gamma^5)\not{k}_e\gamma^\lambda(1-\gamma^5)\not{k}_\nu\Big]\, \mathrm{Im}\Pi^R_{\mu\lambda}(k_W)\,, \tag{4.34}$$

where $\Pi^R_{\mu\lambda}(k_W)$ is the W boson polarization tensor. Note that the expression in the paper is multiplied by a factor of 2 to include the inverse process, but we do not include it here.

Following the identity (Eq. 187 to Eq. 188 in [145]; [146]; also see Le Bellac [147] Chap. 4)

$$\Pi^<_{\mu\lambda}(q) = \Pi^>_{\mu\lambda}(-q) = 2ig_B(q^0)\mathrm{Im}\Pi^R_{\mu\lambda}(q), \tag{4.35}$$

and

$$i\Pi^<_{\mu\lambda}(q) = \int \frac{d^4k_n}{(2\pi)^4}\frac{d^4k_p}{(2\pi)^4}\mathrm{Tr}\Big[\gamma_\mu(1-g_A\gamma^5)G^<(k_p)\gamma_\lambda(1-g_A\gamma^5)G^>(k_n)\Big]\delta^{(4)}(k_W - k_n - k_p)\,, \tag{4.36}$$

where

$$G^<(k) = 2\pi\,\mathrm{sign}(k^0)(1-n_F)(\not{k}+m)\delta(k^2-m^2)\,, \tag{4.37}$$
$$G^>(k) = -2\pi\,\mathrm{sign}(k^0)n_F(\not{k}+m)\delta(k^2-m^2)\,, \tag{4.38}$$

are the bare thermal propagators of the nucleons.

Combing these equations, we get

$$\Gamma = \frac{G_F^2\, cos^2\theta_c}{16(2\pi)^8} \int \frac{d^3k_n}{E_n}\frac{d^3k_p}{E_p}\frac{d^3k_e}{E_e}\frac{1}{E_\nu} f_n(1-f_p)(1-f_e)\delta(E_n - E_p - E_e - E_\nu)$$
$$\mathrm{Tr}\Big[\gamma^\mu(1-\gamma^5)\not{k}_e\gamma^\lambda(1-\gamma^5)\not{k}_\nu\Big]\,\mathrm{Tr}\Big[\gamma_\mu(1-g_A\gamma^5)(\not{k}+m_p)\gamma_\lambda(1-g_A\gamma^5)(\not{k}+m_n)\Big]\,. \quad (4.39)$$

Including the mean fields [75], as discussed in Chap. 2, the expression becomes

$$\Gamma = \frac{G_F^2\, cos^2\theta_c}{16(2\pi)^8} \int \frac{d^3k_n}{E_n^*}\frac{d^3k_p}{E_p^*}\frac{d^3k_e}{E_e}\frac{1}{E_\nu} f_n(1-f_p)(1-f_e)\delta(E_n - E_p - E_e - E_\nu)$$
$$\mathrm{Tr}\Big[\gamma^\mu(1-\gamma^5)\not{k}_e\gamma^\lambda(1-\gamma^5)\not{k}_\nu\Big]\,\mathrm{Tr}\Big[\gamma_\mu(1-g_A\gamma^5)(\not{k}+m_p^*)\gamma_\lambda(1-g_A\gamma^5)(\not{k}+m_n^*)\Big]\,. \quad (4.40)$$

This rate expression indeed agrees with what we got from Appendix. B.

Taking one step further, we can replace the on-shell delta function(s) in Eq. 4.37 and Eq. 4.38 with our proposed unstable particle propagator(s) suggested in Sec. 4.5.2 with $R(k^0, \vec{k}, \Gamma)$. We first start with including the neutron width by dressing the neutron propagator. Then, the rate expression (with a neutron width) becomes

$$\Gamma = \frac{G_F^2\, cos^2\theta_c}{16(2\pi)^8} \int \frac{d^3k_p}{E_p^*}\frac{d^3k_e}{E_e}\frac{1}{E_\nu}(2d^4k_n)R(k_n^0, \vec{k}_n, \Gamma_n)\, sign(k_n^0)\, f_n(1-f_p)(1-f_e)$$
$$\mathrm{Tr}\Big[\gamma^\mu(1-\gamma^5)\not{k}_e\gamma^\lambda(1-\gamma^5)\not{k}_\nu\Big]\,\mathrm{Tr}\Big[\gamma_\mu(1-g_A\gamma^5)(\not{k}+m_p^*)\gamma_\lambda(1-g_A\gamma^5)(\not{k}+m_n^*)\Big]$$
$$\delta(E_n - E_p - E_e - E_\nu)\,. \quad (4.41)$$

Notice that when the width $\Gamma_n \to 0$, that is, when the neutron is on-shell,

$$2\int d^4k_n R(k_n^0, \vec{k}_n, \Gamma_n)\, sign(k_n^0) \to 2\int d^4k_n \delta(k_n^2 - m_n^2)\, sign(k_n^0)$$
$$= \int d^3k_n \frac{\delta(k_n^0 - m_n)}{E_n}\,, \quad (4.42)$$

Eq. 4.41 reduces to Eq. 4.40.

4.5.4 Results

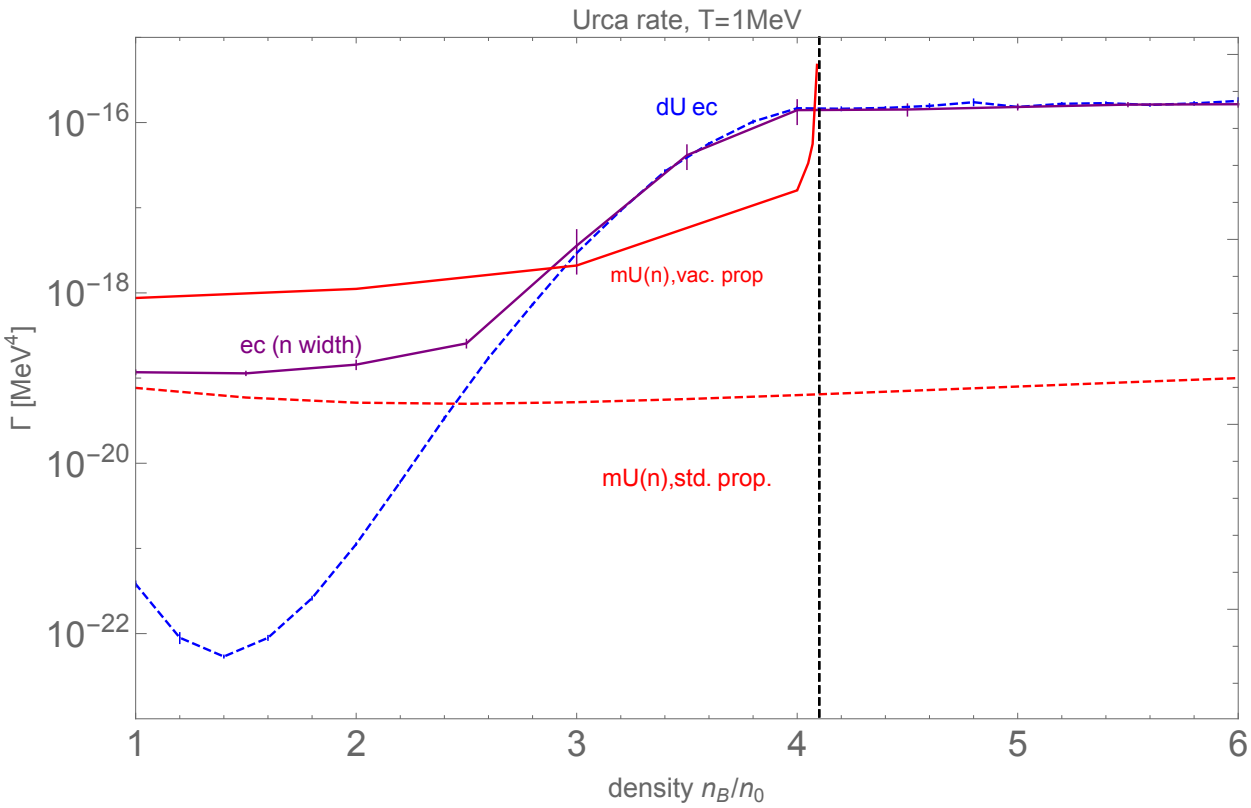

Fig. 4.9: Unified Urca electron capture rate at $T = 1\,\mathrm{MeV}$ using IUF.

We implemented the unified Urca rate with a neutron width. Instead of taking the neutron width as a constant value, we calculated the neutron scattering diagram ($nn \to nn$) with Fermi surface approximation as the contribution to the neutron width.

The results are shown in Fig. 4.9 for $T = 1\,\mathrm{MeV}$ using IUF. The blue dashed line is the electron capture direct Urca rate, and the red dashed line is the crude modified Urca, as we have discussed in detail in Chap. 2. The red solid line is the modified Urca with

angular-averaged matrix element, fully relativistic vacuum propagator, and under Fermi surface approximation (denoted as modified Urca with vacuum propagator). The purple solid line is the unified Urca rate with neutron width implemented. For the modified Urca with vacuum propagator, 4 diagrams have been included, i.e. we include the 2 diagrams of the weak vertices happening before and after the strong vertices and then subtract the sum of their corresponding exchange diagrams. Squaring the total sum $|M_{d,1} + M_{d,2} - M_{e,1} - M_{e,2}|^2$ will also give the interference terms, which are negligible (Sec. 4.3). The divergence issue is discussed in Sec. 4.4, and the enhancement at lower densities [4] because of using a full vacuum propagator instead of $1/\mu_e$ propagator has been observed as well.

For the unified Urca, one can see that it starts from being slightly above the crude modified Urca at low densities, and gradually it makes a transition into direct Urca around the threshold, as expected. One might notice that at low densities, the enhancement is not as strong as the modified Urca with vacuum propagator. This is because this unified Urca calculation only includes the neutron width, which should correspond to the diagram where the strong vertex happens before the weak vertex. It has not been explored that if we include both neutron and proton widths in the unified Urca calculation, then we would get the exchange diagrams and the interference terms. However, as a first step, we have successfully included the sum of direct Urca, modified Urca, and higher-order processes in a single unified calculation. A more rigorous derivation and some technical details are being further explored.

4.6 Conclusion

In this chapter, we have presented several results improving modified Urca calculations and a unified approach to Urca processes. Specifically, we start from Shternin et al. [4] and perform

a relativistic calculation under Fermi surface approximation, where the full propagator leads to a significant enhancement in modified Urca. Then we performed a full phase space and fully relativistic calculation without angular averaging over the matrix element. We found an even larger enhancement, mainly due to phase space integration and not performing angular averaging.

However, in these calculations, an unphysical divergence emerges around the threshold. To solve the issue, we tried two different approaches. First, we add a width to the internal propagator, which pushes the pole above the real axis and solves the infinity problem. However, this approach does not explain what it becomes above the threshold. This leads to the second approach which is an approach that unifies Urca calculations into a neutrino self-energy diagram. In this approach, modified Urca smoothly makes a transition into direct Urca above the threshold.

The full phase space modified Urca and the unified Urca calculations are among the first calculations that allow modified Urca to go beyond Fermi surface approximation. The unified Urca will also be less computationally expensive than the full phase-space integral. In all of the calculations presented in this chapter, an enhancement of modified Urca is observed compared to the traditional calculation. This can lead to faster cooling [4], a shift of bulk viscosity resonance peak [141], and so on. Since our full phase-space approach can go beyond Fermi surface approximation, we plan to check if neutron decay and electron capture modified Urca are equal in cold beta equilibrium. If not, we can correct the beta equilibrium as we did in Chap. 2.

Chapter 5

The MUSES Framework and Gaussian Process Interpolation

5.1 Introduction to MUSES

MUSES (Modular Unified Solver of Equation of States) is an open-source cyberinfrastructure that provides novel tools to study gravitational wave astrophysics, nuclear physics, and heavy-ion physics. The MUSES official website is `https://musesframework.io/` and all the source codes are in the following GitLab repo `https://gitlab.com/nsf-muses`.

As mentioned previously, MUSES mainly consists of two parts, the equation of state modules and the users or observable modules. The alpha release of MUSES, which is expected in 2024, will include the CMF group [15], χEFT group [17], UTK group [16], flavor equilibration group [67, 68] and QLIMR group (I-L-Q plus M-R).

An important technology that MUSES uses is the Docker `https://www.docker.com/` container. It is a modern technology that is essentially a lightweight virtual machine. The two core concepts are the Docker images and the Docker containers. A Docker image is a file of a wrapped-up application, and a Docker container is an instance of the file. This pair of concepts is similar to class and instance of class in object-oriented programming. In the

Docker architecture, there is a Docker registry that stores the images, a Docker host server, and a Docker client, where users interact with the host server. In the host server, the core part is Docker Daemon, which manages Docker images and Docker containers.

An advantage of the containerization technology is that it easily allows scalable deployment. Currently, each individual module will be containerized and will use Pegasus workflow management system (Pegasus WMS) `https://pegasus.isi.edu/` to automate computation tasks.

5.2 The Flavor Equilibration Module

Our flavor equilibration module aims at providing calculations of relevant observables for the users, which includes Urca rates, warm beta-equilibrium proton fraction and chemical potentials, relaxation rates, susceptibilities, static bulk viscosity, and damping time. All the observables and their physics have been discussed in the previous chapters. The source code is published at `https://gitlab.com/nsf-muses/flavor-equilibration/beta_equil` with user instructions included.

The module can either be used as an independent package or within the MUSES calculation engine. If the module is used as part of the MUSES calculation framework, then the user will pick one of the EoSes available within the framework. At the moment, the calculation engine is under construction. More information will be provided at the alpha release.

On the other hand, if one wants to provide and use some other EoSes not available from the MUSES framework, the module also works as an independent package. The workflow of the flavor equilibration module is shown in Fig. 5.1. Note that the lepton module on the top left corner will replace our internal neutralizer when used within the MUSES calculation

engine. One can provide a hadron EoS with dispersion relations, then the module can provide calculations for the Urca rates and/or the flavor equilibration information. More instructions are provided in the README.md file of the Gitlab repo.

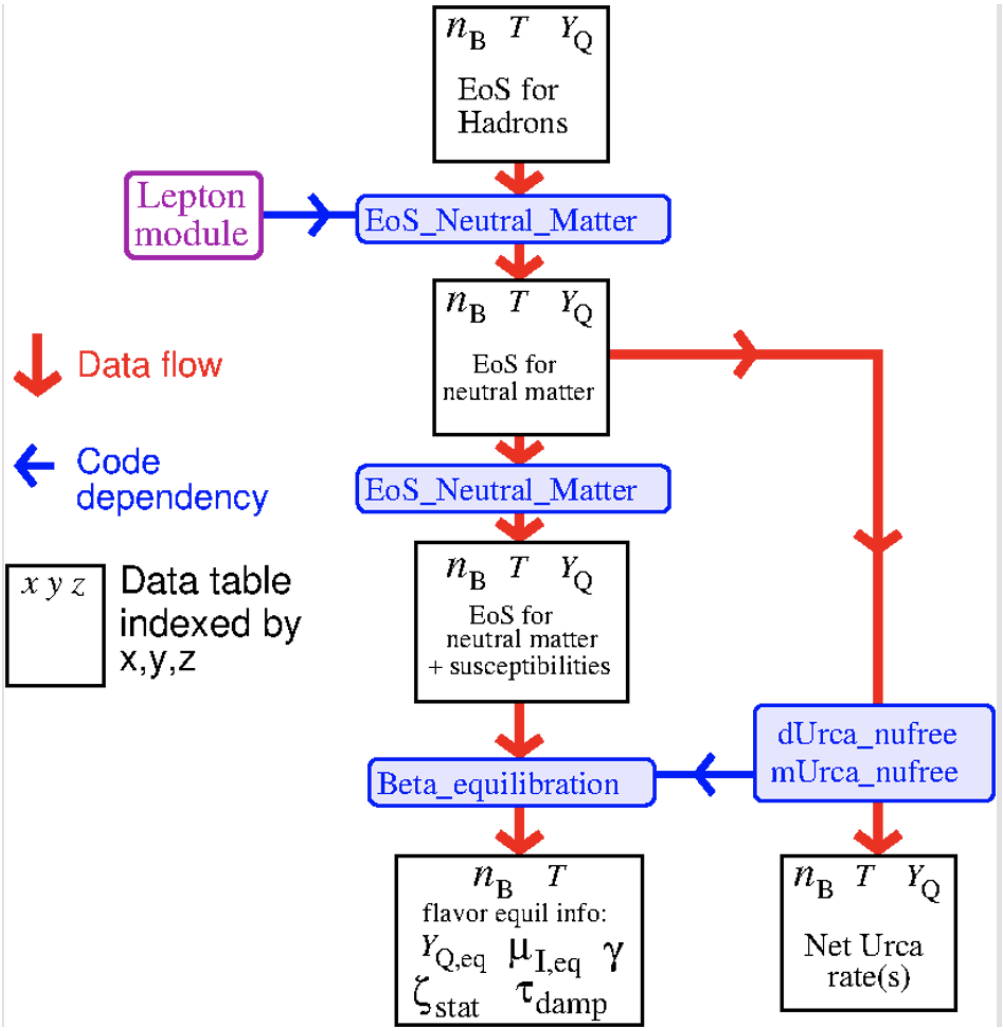

Fig. 5.1: MUSES flavor equilibration module workflow. Produced by Mark Alford.

5.3 Gaussian Process Interpolation

At the moment, the interpolation method used in the collaboration predominantly is linear interpolation. The main disadvantages are that, first, it is not able to provide smooth higher-order derivatives, and second, its accuracy may not be good enough to match the requirements for some modules. Therefore, the aim of this section is to provide a study on Gaussian process interpolation and investigate its performance compared to linear interpolation.

Gaussian process (GP) regression is a Bayesian framework for regressing data. It models data by a joint multidimensional Gaussian distribution, i.e. assuming the data given are samples drawn from a joint distribution, and the parameters that describe the distribution can be estimated from the data. Now, predictions at new points correspond to calculating the mean of conditional distributions.

A standard textbook for GP regression is [149]. A nice tutorial on GP regression is [150].

For the development of this section, I would like to thank Reed Essick for helpful advice.

5.3.1 General Formalism and A Basic Example

Suppose we have a data set. We assume that the dependent variables are realizations of a random variable f. We model the conditional distribution of the dependent variable $f|X$ as a joint Gaussian distribution $f|X \sim N(\mu, K)$, where μ is the vector of means and K is the covariance matrix that describes the correlations between each independent variables. The mean vector and the covariance matrix fully characterize and determine the joint Gaussian distribution.

If we want to predict the value f_* at a new point x_*, we first construct a joint Gaussian

distribution $f, f_*|X, x_*$, and then obtain the conditional distribution

$$f_*|f, X, x_* \sim N(K_*^T K^{-1} f \, , K_{**} - K_*^T K^{-1} K_*) \, . \tag{5.1}$$

Essentially, we are predicting a distribution, where the mean of the predicted distribution is the desired value. The math proof is given in Chapter 2 of [149].

A simple example would easily illustrate how it works. Suppose we have a data set $D = \{(x_1, \mu_1), (x_2, \mu_2)\}$, and we want to predict the value μ_* at a new point x_*. We assume the data D is drawn from a joint 2d Gaussian distribution, that is,

$$P_{f_1,f_2}(f_1 = \mu_1, f_2 = \mu_2) = \frac{1}{(2\pi)|K|^{\frac{1}{2}}} \exp\left(-\frac{1}{2} \begin{bmatrix} f_1 - \mu_1 & f_2 - \mu_2 \end{bmatrix} \begin{bmatrix} K_{11} & K_{12} \\ K_{21} & K_{22} \end{bmatrix}^{-1} \begin{bmatrix} f_1 - \mu_1 \\ f_2 - \mu_2 \end{bmatrix} \right) , \tag{5.2}$$

where K is the covariance matrix, and $|K|$ is the determinant of K. Let us pick the most common kernel function that generates the covariance matrix, which is usually called the squared exponential kernel. We have, for each entry,

$$K_{ij} = \theta_1 e^{-\frac{|x_i - x_j|^2}{2\theta_2}} \, , \tag{5.3}$$

where θ_1 and θ_2 are two hyperparameters we choose. In general, θ_1 describes the variance of the data, and θ_2 describes the correlation lengths of the data.

Now, we include one more piece of information, which is x_*. The new joint distribution is

$$P_{f_1,f_2,f_*}(f_1=\mu_1, f_2=\mu_2, f_*=\mu_*) \propto$$
$$\exp\left(-\frac{1}{2}\begin{bmatrix} f_1-\mu_1 & f_2-\mu_2 & f_*-\mu_* \end{bmatrix}\begin{bmatrix} K_{11} & K_{12} & K_{1*} \\ K_{21} & K_{22} & K_{2*} \\ K_{*1} & K_{*2} & K_{**} \end{bmatrix}^{-1}\begin{bmatrix} f_1-\mu_1 \\ f_2-\mu_2 \\ f_*-\mu_* \end{bmatrix}\right), \quad (5.4)$$

and the conditional distribution $f_*|X, f, x_* \sim N(\mu_*, \sigma_*)$, where

$$\mu_* = K_*^T K^{-1} f\,, \quad (5.5)$$

and

$$\sigma_* = K_{**} - K_*^T K^{-1} K_*\,. \quad (5.6)$$

The mean μ_* is the value we want to predict at x_*.

A simple test of setting x_* to x_1 will get back μ_1 with no uncertainty, i.e. $\sigma_* = 0$. Given that $x_* = x_1$ and $K_* = \begin{bmatrix} \theta_1 \\ K_{21} \end{bmatrix}$, and define $K_{12} = \theta_1 k_{12}$, then

$$
\begin{aligned}
\mu_* &= K_{x_*}^T K^{-1} f \\
&= \begin{bmatrix} \theta_1 & K_{21} \end{bmatrix} \begin{bmatrix} \theta_1 & K_{12} \\ K_{21} & \theta_1 \end{bmatrix}^{-1} \begin{bmatrix} \mu_1 \\ \mu_2 \end{bmatrix} \\
&= \begin{bmatrix} 1 & k_{12} \end{bmatrix} \cdot \frac{1}{1-k_{12}^2} \begin{bmatrix} 1 & -k_{12} \\ -k_{21} & 1 \end{bmatrix} \begin{bmatrix} \mu_1 \\ \mu_2 \end{bmatrix} \\
&= \frac{1}{1-k_{12}^2} \begin{bmatrix} 1 & k_{12} \end{bmatrix} \begin{bmatrix} \mu_1 - k_{12}\mu_2 \\ -\mu_1 k_{21} + \mu_2 \end{bmatrix} \\
&= \frac{1}{1-k_{12}^2} (\mu_1 - k_{12}\mu_2 - \mu_1 k_{12}^2 + k_{12}\mu_2) \\
&= \frac{1}{1-k_{12}^2} (1-k_{12}^2) * \mu_1 \\
&= \mu_1 \,,
\end{aligned}
$$

and

$$\begin{aligned}
\sigma_*^2 &= K_{**} - K_*^T K^{-1} K_* \\
&= \theta_1 - \begin{bmatrix} \theta_1 & K_{21} \end{bmatrix} \begin{bmatrix} \theta_1 & K_{12} \\ K_{21} & \theta_1 \end{bmatrix}^{-1} \begin{bmatrix} \theta_1 \\ K_{21} \end{bmatrix} \\
&= \theta_1 - \begin{bmatrix} \theta_1(1 & k_{12}) \end{bmatrix} \cdot \frac{1}{1-k_{12}^2} \begin{bmatrix} 1 & -k_{12} \\ -k_{21} & 1 \end{bmatrix} \begin{bmatrix} 1 \\ k_{12} \end{bmatrix} \\
&= \theta_1 - \frac{\theta_1}{1-k_{12}^2} \begin{bmatrix} 1 & k_{12} \end{bmatrix} \begin{bmatrix} 1-k_{12}^2 \\ 0 \end{bmatrix} \\
&= \theta_1 - \theta_1 \\
&= 0\,.
\end{aligned}$$

5.3.2 Kernel Functions

Kernel functions are different ways of generating the covariance matrix in the Gaussian distribution. The most common one is the square exponential kernel (also called RBF), as we have encountered in the example above. It assumes the covariance between points x_i and x_j to be

$$K_{ij} = \theta_1 \exp\left(-\frac{|x_i - x_j|^2}{2\theta_2}\right). \tag{5.7}$$

θ_1 describes the variance of the covariances, and θ_2 describes the correlation lengths of the data. A characteristic of the matrix element is that the values of the entries decay exponentially when getting away from the diagonal, and only the entries close to the diagonal are non-vanishing. If the correlation length is too short, then very few points are correlated with each other. In this case, the regression would be zigzag, because for each point, it does

not know much information about the neighboring points. If the correlation length is too long, then a point is correlated with too many other points. The regression would be too "smooth" or too "averaged" such that it loses some information about the fine structures of the data. Finding good hyperparameters would be an important topic which we will cover in the next subsection.

If the underlying function is smooth and continuous, this square exponential kernel is a good one to start with. In the case of interpolating equation of states without phase transition, the thermodynamic quantities are generally smooth, so we will work with this kernel in the project. If the equation of state has sharp features, then modifications might be needed [151].

Other kernel functions include white noise kernel, which adds some noise to the data, Matern kernel, which captures some degrees of non-smoothness, periodic kernel, which assumes some periodicity of the underlying data and so on. It is common to combine some of these kernels to capture more features.

5.3.3 Hyperparameter Estimation from the Likelihood

In GP regression, we have some hyperparameters that describe the characteristics of the data, for example, variance and correlation length. A common systematic way of estimating these hyperparameters is to maximize the likelihood function (or maximize the posterior) over the hyperparameters.

From Bayes theorem,

$$P(\theta|D) = P(D|\theta)P(\theta)\,, \tag{5.8}$$

where $P(\theta)$ is the prior, which is our belief about the parameters θ *before* doing any experiment, $P(\theta|D)$ is the posterior, which is the updated information including what we learned

from the experiment, $P(D) = 1$ since this is the data we obtained, and finally $L(\theta) \equiv P(D|\theta)$ is the likelihood.

In our exploration, we use a flat prior (i.e. assume a uniform distribution of θ), so maximizing the likelihood and maximizing the posterior are the same.

For example, we have a set of data that we believe are from a normal distribution:

$$X_1, \ldots, X_N \sim \mathcal{N}(\mu, \sigma^2)\,, \tag{5.9}$$

where X_i are independent draws from this identical distribution. The log-likelihood function is:

$$\begin{aligned} \log P(X_1, \ldots, X_N|\mu, \sigma^2) &= \log\left(\prod_{i=1}^{N} \frac{1}{\sqrt{2\pi\sigma^2}} \exp\left(-\frac{(x_i-\mu)^2}{2\sigma^2}\right)\right) \\ &= -\frac{N}{2}\log(2\pi) - \frac{N}{2}\log\left(\sigma^2\right) - \sum_{i=1}^{N}\frac{(x_i-\mu)^2}{2\sigma^2}\,. \end{aligned} \tag{5.10}$$

Calculating the partial derivatives $\frac{\partial L}{\partial \mu}$ and $\frac{\partial L}{\partial \sigma^2}$, we can get the estimate for each of the parameters

$$\mu = \frac{\sum X_i}{N}\,, \tag{5.11}$$

and

$$\sigma^2 = \frac{1}{N}\sum (X_i - \mu)^2\,. \tag{5.12}$$

In reality, the likelihood functions would be much more complicated than the simple example above. The (log) likelihood for GP (given in Chapter 2 of [149]) is

$$logP(f|X,\theta) = -\frac{1}{2}f^T K^{-1} f - \frac{1}{2}log|K| - \frac{N}{2}log2\pi\,, \tag{5.13}$$

where N is the number of training data. Therefore, some other numerical methods need to be used.

Gradient descent is a common approach to maximize likelihood (or minimize the negative of likelihood). At each point in parameter space, one can calculate the gradient, whose direction is the fastest change at the point, and iteratively "go down the hill" to reach the global minimum of the objective function (or to reach a good local minimum in case the landscape to complicated).

On the practical level, at each iteration, the matrix inversion operation is carried out, whose time complexity is on the order of $O(n^3)$. Therefore, if the data size is too large (empirically a few thousand data points in our exploration), downsampling or sparse matrix approximation may be necessary.

5.3.4 Markov Chain Monte Carlo (MCMC) and Autocorrelation Analysis

In order for the GP interpolator to be more robust, we use Markov Chain Monte Carlo to sample from the likelihood distribution over all hyperparameters, and then randomly pick some of the samples out of the whole MC chain, each determining one interpolator and then we average over all predictions. The argument for doing this is based on posterior predictive distribution, where

$$p(x_*|X) = \int_\Theta p(x_*|\theta)p(\theta|X)d\theta \tag{5.14}$$

$$\approx \frac{1}{M}\sum_i p(x_*|\theta_i)p(\theta_i|X)\,. \tag{5.15}$$

Therefore, by sampling the hyperparameter sets multiple times, each hyperparameter set defining a GP interpolator, we average over all of the interpolators to obtain an approximation of the posterior predictive distribution.

Before we get into the MCMC sampling technique, we start from Markov Chain. Markov Chain is a chain of states such that the probability of transiting from the current state to the next depends only on the current state, i.e. does not depend on the history paths of how it reaches the current state. Mathematically,

$$P(X_{n+1} = x | X_1 = x_1, X_2 = x_2, \ldots, X_n = x_n) = P(X_{n+1} = x | X_n = x_n)\,. \tag{5.16}$$

An important concept for Markov Chains is stationary distribution. Denote the transition matrix from one state to another as T, and we start from a random distribution S_i over all states. Then, the transition from the distribution over current states to the next is

$$S_{i+1} = S_i T\,. \tag{5.17}$$

If we keep applying the transition matrix, the distribution over the chain may stay stationary, that is

$$S = ST\,. \tag{5.18}$$

What this means is that the probability distribution of being at each state stays the same from some time point on. Therefore, as we keep applying the transition operation, the distribution S over the Markov Chain asymptotically reaches the target distribution P, which is the distribution we want to sample our hyperparameters from.

When the stationary distribution is reached, we have the detailed balance:

$$P(X_1)T(X_1 \to X_2) = P(X_2)T(X_2 \to X_1)\,. \tag{5.19}$$

The transition probability is further divided into two parts, a proposal distribution g and an acceptance rate A,

$$T(X_1 \to X_2) = g(X_2|X_1)A(X_1 \to X_2)\,. \tag{5.20}$$

so

$$\frac{A(X_1 \to X_2)}{A(X_2 \to X_1)} = \frac{g(X_1|X_2)}{g(X_2|X_1)}\frac{T(X_1 \to X_2)}{T(X_2 \to X_1)}\,. \tag{5.21}$$

A common choice of the acceptance rate is

$$A(X_1 \to X_2) = \min\Big(1, \frac{g(X_1|X_2)}{g(X_2|X_1)}\frac{T(X_1 \to X_2)}{T(X_2 \to X_1)}\Big)\,. \tag{5.22}$$

This is the well-known Metroplis-Hastings algorithm in Monte Carlo.

Now that we know Markov Chain and Monte Carlo, we can put together to see how MCMC works. In our hyperparameter space, we want to sample from the likelihood. We start from a (good) initial guess of the hyperparameters (a point in the parameter space x_1). We propose a distribution $g(x)$, sample a point from this distribution $g(x_2|x_1)$, and calculate the acceptance rate $A(x_1 \to x_2)$. Then we generate a random number r from a uniform distribution between 0 and 1. If $r < A$, then we accept the new state. Otherwise, we stay in the same state. Then, we iteratively perform the steps described above, until the stationary distribution is reached. Discarding some first samples (known as burn-in step), we obtain a good approximation to the likelihood function.

In the actual calculations, we use the emcee package (`https://emcee.readthedocs.io/`

en/stable/) to perform MCMC sampling. The algorithm is published in [152].

At this point, a question is: How long does the chain need to be? If the chain is short, the samples close to each other would be correlated, dependent samples. If the chain is too long, we are guaranteed to obtain independent samples but it would be computationally costly. Therefore, we need to perform the autocorrelation analysis.

Autocorrelation is the self-correlation of a time series, i.e. how the series at different time lags correlated with each other. Denote the series of our samples as $B(t)$, and the time lag or the shift as τ,

$$\rho_{B(t)B(t+\tau)}(\tau) = \frac{E[B(t)B(t+\tau)]}{\sigma_{B_{(t)}}\sigma_{B_{(t+\tau)}}} \,. \tag{5.23}$$

At $\tau = 0$, the autocorrelation should be 1, and decay as τ increases. One can define a threshold value below which the samples are considered as independent. The emcee package provides the functionalities of estimating autocorrelation time.

5.3.5 Derivatives

GP interpolators can also provide gradient information. The predicted value as a function of new points x_* is

$$f(x_*) = K_*^T K^{-1} y \,. \tag{5.24}$$

Suppose in our training set, we have n points. Then, K_*^T is the vector consisting of $K(x_i, x_*)$, where x_i are all n training points. K_*^T is of size 1 by n. If we denote $\alpha \equiv K^{-1}y$, then α is of size n by 1. We can rewrite the matrix multiplication as the sum of each multiplication,

$$f(x_*) = \sum_{i=1}^{n} \alpha_i K(x_i, x_*) \,. \tag{5.25}$$

Calculating the gradient of f at x_* is equivalent to calculating the gradient of the kernel

function K at x_*, i.e.

$$\nabla f(x_*) = \sum_{i=1}^{n} \alpha_i \nabla K(x_i, x_*) \,. \tag{5.26}$$

GP allows smooth high-order derivatives, as long as the kernel has smooth high-order derivatives. For example, if we choose the square exponential kernel,

$$K(x_0, x_*) = \sigma_f^2 e^{-\frac{(x_0 - x_*)^2}{l^2}} \,, \tag{5.27}$$

$$\nabla K(x_0, x_*) = K(x_0, x_*) * \frac{2 * (x_0 - x_*)}{l^2} \,. \tag{5.28}$$

5.3.6 Results on Interpolating the Equation of States

We carry out some preliminary tests on the performance of the GP interpolator to compare to the performance of the linear interpolator.

From the practical point of view, as mentioned above, the plain type of matrix inversion operation has a time complexity of $O(n^3)$, we only use no more than 2000 data points on this test. For the inversion, we simply use numpy packages numpy.linalg.inv. In order to speed up the algorithms of maximizing the likelihood and MCMC sampling, it would be better if we have some good estimation as initial guesses of the hyperparameters. Since the hyperparameters are supposed to describe the mean and variance of the data, we calculate the mean and variance of the data in each direction and use them as the initial guesses for the algorithms.

Another important thing to point out is that we perform tests on a regular grid, since most of the EoS tables can be generated as regular grids. Besides this, if downsampling is involved, it is necessary that the downsampled data is also in a regular grid (i.e. cannot simply take one row of data out of every few lines).

The following is the result for IUF equation of state on a $13 \times 15 \times 10$ grid in number density n_B, temperature T and proton fraction Y_Q, ranging from $1n_0$ to $6n_0$ in n_B, 1 MeV to 10 MeV in T, and 0.05 to 0.25 in Y_Q.

Also, it is worthwhile pointing out that *in this test case* the chain length needs not to be as many as that estimated by the emcee package autocorrelation analysis. Within 100 MC steps, the errors are already low, likely due to good initial guesses.

Tab. 5.1: Mean absolute percentage error of different methods.

Linear	Maximizing Likelihood	Avg. over 50 MCMC Samples
0.0241	0.0053	0.0025

One can see from Tab. 5.1 that both of the GP interpolator predictions have higher accuracy compared to the linear interpolator, with the averaged interpolator result being 10 times better in terms of error. This averaging method may have small fluctuations in its performance because of randomly picking the samples. However, the more sets of hyperparameters one sample (i.e. the more interpolators), the better these interpolator predictions should approximate the true distribution, and the better the result should be.

5.3.7 Conclusion

From what we have seen in the performance tests, Gaussian process interpolation on the equation of states has demonstrated its promising power in terms of accuracy.

In reality, the equation of state used would have 10^5 data points or more. In every optimization step, the inversion of the covariance matrix is required, and a plain type of matrix inversion would make this task formidable. Since we use the square exponential kernel, a characteristic is that entries of the matrix further away from the diagonal are exponentially suppressed. Then, it would be valid to discard points away from where we are

predicting, because only "neighboring points" are correlated to each other. This is the idea of the sparse matrix approximation and this approximation is suggested for the implementation stage.

APPENDICES

Appendix A

The SFHo relativistic mean field theory

The Lagrangian for the SFHo relativistic mean field model is given in Refs. [153, 5] and reads

$$\mathcal{L} = \mathcal{L}_{\rm N} + \mathcal{L}_{\rm M} + \mathcal{L}_{l}\,, \tag{A.1}$$

$$\mathcal{L}_N = \bar{\psi}(i\gamma^\mu\partial_\mu - m_N + g_\sigma\sigma - g_\omega\gamma^\mu\omega_\mu - \frac{g_\rho}{2}\boldsymbol{\tau}\cdot\boldsymbol{\rho}_\mu\gamma^\mu)\psi\,, \tag{A.2}$$

with bold symbols being vectors in iso-space, $\boldsymbol{\tau}$ being the iso-spin generators, and

$$\begin{aligned}\mathcal{L}_M =& \frac{1}{2}\partial_\mu\sigma\partial^\mu\sigma - \frac{1}{2}m_\sigma^2\sigma^2 - \frac{bM}{3}(g_\sigma\sigma)^3 - \frac{c}{4}(g_\sigma\sigma)^4 - \frac{1}{4}\omega_{\mu\nu}\omega^{\mu\nu} + \frac{1}{2}m_\omega^2\omega_\mu\omega^\mu + \frac{\zeta}{24}g_\omega^4(\omega_\mu\omega^\mu)^2 \\ & - \frac{1}{4}\boldsymbol{B}_{\mu\nu}\cdot\boldsymbol{B}^{\mu\nu} + \frac{1}{2}m_\rho^2\boldsymbol{\rho}_\mu\cdot\boldsymbol{\rho}^\mu + \frac{\xi}{24}g_\rho^4(\boldsymbol{\rho}_\mu\cdot\boldsymbol{\rho}^\mu)^2 + g_\rho^2\Big[\sum_{i=1}^{6}a_i\sigma^i + \sum_{j=1}^{3}b_j(\omega_\mu\omega^\mu)^j\Big]\boldsymbol{\rho}_\mu\cdot\boldsymbol{\rho}^\mu\,,\end{aligned} \tag{A.3}$$

where

$$\omega_{\mu\nu} = \partial_\mu \omega_\nu - \partial_\nu \omega_\mu \,, \tag{A.4}$$

$$\boldsymbol{B}_{\mu\nu} = \partial_\mu \boldsymbol{\rho}_\nu - \partial_\nu \boldsymbol{\rho}_\mu \,. \tag{A.5}$$

The lepton contribution

$$\mathcal{L}_l = \bar{\psi}_e \left(i\gamma^\mu \partial_\mu - m_e \right) \psi_e \,, \tag{A.6}$$

consists of free electrons with a mass of $m_e = 0.511\,\mathrm{MeV}$. In our calculations we use the values of the masses and couplings given in the online CompOSE database. These are listed in Table A.1. In the table,

$$c_\sigma = g_\sigma / m_\sigma \,, \tag{A.7}$$

$$c_\omega = g_\omega / m_\omega \,, \tag{A.8}$$

$$c_\rho = g_\rho / m_\rho \,. \tag{A.9}$$

Quantity	Unit	Value
c_σ	fm	3.1791606374
c_ω	fm	2.2752188529
c_ρ	fm	2.4062374629
b		$7.3536466626 \times 10^{-3}$
c		$-3.8202821956 \times 10^{-3}$
ζ		$-1.6155896062 \times 10^{-3}$
ξ		$4.1286242877 \times 10^{-3}$
a_1	fm^{-1}	$-1.9308602647 \times 10^{-1}$
a_2		$5.6150318121 \times 10^{-1}$
a_3	fm	$2.8617603774 \times 10^{-1}$
a_4	fm^2	2.7717729776
a_5	fm^3	1.2307286924
a_6	fm^4	$6.1480060734 \times 10^{-1}$
b_1		5.5118461115
b_2	fm^2	-1.8007283681
b_3	fm^4	4.2610479708×10^2
m_σ	fm^{-1}	2.3689528914
m_ω	fm^{-1}	3.9655047020
m_ρ	fm^{-1}	3.8666788766
m_n	MeV	939.565346
m_p	MeV	938.272013
M	MeV	939

Tab. A.1: SFHo parameter values taken from CompOSE (`https://compose.obspm.fr/eos/34`). The last three masses are taken from [5].

Appendix B

Direct Urca neutron decay rate

From Fermi's Golden rule, we have the rate (Eq. 3.28) [3, 115]

$$\Gamma_{\rm nd} = \int \frac{d^3k_n}{(2\pi)^3}\frac{d^3k_p}{(2\pi)^3}\frac{d^3k_e}{(2\pi)^3}\frac{d^3k_\nu}{(2\pi)^3}\frac{\sum|M|^2}{(2E_n^*)(2E_p^*)(2E_e)(2E_\nu)}(2\pi)^4\delta^{(4)}(k_n-k_p-k_e-k_\nu)f_n(1-f_p)(1-f_e)\,. \tag{B.1}$$

There is no neutrino Fermi-Dirac factor because we assume the medium is neutrino-transparent, i.e., neutrinos escape the star. The spin-summed matrix element is [77]

$$\sum|M|^2 = 32G^2[(g_A^2-1)m_n^*m_p^*(k_e\cdot k_\nu)+(g_A-1)^2(k_e\cdot k_n)(k_p\cdot k_\nu)+(1+g_A)^2(k_p\cdot k_e)(k_n\cdot k_\nu)]\,, \tag{B.2}$$

where $G = G_F\cos\theta_c$, $G_F = 1.166\times10^{-11}$ MeV^{-2} is the Fermi constant and $\theta_c = 13.04°$ is the Cabbibo angle. As they originate from spin summations (see Appendix B of [75]), the 4-vector dot products in the matrix element (B.2) are $k^\mu = (E^*, \mathbf{k})$.

It is convenient to define the rescaled dimensionless matrix element

$$\begin{aligned}\mathcal{M} &\equiv \frac{\sum |M|^2}{32G^2 E_n^* E_p^* E_e E_\nu} \\ &= \frac{(g_A^2-1)m_n^* m_p^*(k_e\cdot k_\nu) + (g_A-1)^2(k_e\cdot k_n)(k_p\cdot k_\nu) + (1+g_A)^2(k_p\cdot k_e)(k_n\cdot k_\nu)}{E_n^* E_p^* E_e E_\nu} \ .\end{aligned} \tag{B.3}$$

In the nonrelativistic limit, since $g_A \approx 1$, $\mathcal{M} \approx (1+3g_A^2) \sim 4$ [62, 122, 97, 77, 3, 154].

The neutron decay rate can now be written

$$\Gamma_{\rm nd} = \frac{2G^2}{(2\pi)^8}\int d^3k_n d^3k_p d^3k_e d^3k_\nu \, \mathcal{M}\, \delta^{(4)}(k_n - k_p - k_e - k_\nu) f_n(1-f_p)(1-f_e)\,. \tag{B.4}$$

The 12-dimensional integral can be reduced to a 5-dimensional integral as follows. Integrating over the 3-momentum conservation delta functions reduces the integral to 9 dimensions (compare (E.1) in Ref. [117])

$$\Gamma_{\rm nd} = \frac{2G^2}{(2\pi)^8}\int d^3k_n d^3k_p d^3k_e \, \mathcal{M}\delta(E_n - E_p - E_e - |\vec{k}_n - \vec{k}_p - \vec{k}_e|) f_n(1-f_p)(1-f_e)\ . \tag{B.5}$$

The remaining delta function imposes energy conservation in the creation of the neutrino: $E_\nu = |\vec{k}_\nu|$, so the argument of the delta function is

$$\begin{aligned} g(\phi) &\equiv E_\nu - |\vec{k}_n - \vec{k}_p - \vec{k}_e|\ , \\ E_\nu &\equiv E_n - E_p - E_e\ . \end{aligned} \tag{B.6}$$

Each momentum integral can be written in polar co-ordinates as $d^3k = k^2 dk dz d\phi$ where $z = \cos\theta$. Setting up the following coordinate system (see Appendix E in [117])

$$\vec{k}_n = k_n(0,0,1)\,, \tag{B.7}$$

$$\vec{k}_p = k_p(\sqrt{1-z_p^2},0,z_p)\,, \tag{B.8}$$

$$\vec{k}_e = k_e(\sqrt{1-z_e^2}\,\cos\phi,\sqrt{1-z_e^2}\,\sin\phi,z_e)\,, \tag{B.9}$$

allows us to integrate over z_n and ϕ_n yielding a factor of 4π and over ϕ_p yielding a factor of 2π, which eliminates three angular integrals, so that (compare (E.5) in [117])

$$\Gamma_{\rm nd} = \frac{G^2}{16\pi^6}\int_0^\infty dk_n \int_0^{k_p^{\rm max}} dk_p \int_0^{k_e^{\rm max}} dk_e k_n^2 k_p^2 k_e^2\, f_n(1-f_p)(1-f_e)\, I(k_n,k_p,k_e)\ , \tag{B.10}$$

where

$$I(k_n,k_p,k_e) \equiv \Theta(E_\nu)\int_{-1}^1 dz_p \int_{-1}^1 dz_e \int_0^{2\pi} d\phi\, \mathcal{M}\,\delta(g(\phi))\ . \tag{B.11}$$

Note that for simplicity we label the electron azimuthal angle as ϕ (rather than ϕ_e). The factor of $\Theta(E_\nu)$ restricts the integral to the region of momentum space where the neutrino energy $E_\nu(k_n,k_p.k_e)$ is positive, which is a requirement for the emission of a neutrino. This condition leads to the upper limits on the proton and electron momenta. If we perform the integrals in the order shown in (B.10) then the electron momentum integral is the inner integral, so it is performed for known values of k_n and k_p, so the constraint $E_\nu > 0$ corresponds to $E_e < E_n - E_p$. Similarly, the k_p integral is performed for a known value of k_n, so its range is constrained by requiring that there is enough energy to create an electron (of unknown momentum) and a neutrino, $E_p < E_n - m_e$. This leads to upper limits on the proton and

electron integral,

$$k_p^{\max} = \Theta(E_n - U_p - m_p - m_e)\sqrt{(E_n - U_p - m_e)^2 - m_p^2}\,, \tag{B.12}$$

$$k_e^{\max} = \Theta(E_n - E_p - m_e)\sqrt{(E_n - E_p)^2 - m_e^2}\,. \tag{B.13}$$

In the delta function in Eq.(B.11),

$$g(\phi) = E_\nu - \sqrt{R + S\cos\phi}\,, \tag{B.14}$$

$$\text{where} \quad R \equiv k_n^2 + k_p^2 + k_e^2 - 2k_n k_e z_e - 2k_n k_p z_p + 2k_p k_e z_p z_e\,, \tag{B.15}$$

$$S \equiv 2k_p k_e \sqrt{1 - z_p^2}\sqrt{1 - z_e^2}\,. \tag{B.16}$$

Since $g(\phi)$ depends on ϕ only via $\cos\phi$ there will be either zero or two solutions to $g(\phi) = 0$, so

$$I(k_n, k_p, k_e) = 2\,\Theta(E_\nu)\int_{-1}^{1} dz_p \int_{-1}^{1} dz_e\,\Theta\Big(S - |E_\nu^2 - R|\Big)\frac{\mathcal{M}_{\phi_0}}{|g'(\phi_0)|}\,, \tag{B.17}$$

where $\mathcal{M}_{\phi_0}$ is the dimensionless rescaled matrix element (B.3) evaluated at ϕ_0, which can be either of the two solutions of $g(\phi) = 0$,

$$\cos\phi_0 = \frac{E_\nu^2 - R}{S}\,. \tag{B.18}$$

It does not matter which solution we use for ϕ_0 because g is a function of $\cos\phi$ and $\mathcal{M}$ depends only on $\cos\phi$ and $\sin^2\phi$, so the integrand has the same value for both the solutions. The theta function $\Theta(S - |E_\nu^2 - R|)$ imposes the condition that there are two solutions (rather than none), by limiting the integral to the domain where $-1 < \cos\phi_0 < 1$.

We now use (B.14) and (B.18) to evaluate the integrand in (B.17).

Firstly, the Jacobian of the delta function is

$$|g'(\phi_0)| = \frac{\sqrt{S^2 - (E_\nu^2 - R)^2}}{2E_\nu} \ . \tag{B.19}$$

Using (B.19) in (B.17),

$$I = 4E_\nu \Theta(E_\nu) \int_{-1}^{1} dz_p \int_{-1}^{1} dz_e \frac{\Theta\Big(S - |E_\nu^2 - R|\Big)}{\sqrt{S^2 - (E_\nu^2 - R)^2}} \mathcal{M}_{\phi_0} \ . \tag{B.20}$$

Secondly, substituting (B.18) in to (B.2) gives the matrix element

$$\mathcal{M}_{\phi_0} = \frac{1}{2} \frac{(g_A - 1)^2 F_1 + (g_A + 1)^2 F_2 + (g_A^2 - 1) F_3}{E_n^* E_p^* E_e E_\nu} \, , \tag{B.21}$$

where

$$F_1 = \Big(k_n^2 + k_e^2 - k_p^2 - 2E_p^* E_\nu - E_\nu^2 - 2k_n k_e z_e\Big)\Big(k_n k_e z_e - E_e E_n^*\Big) \ , \tag{B.22}$$

$$F_2 = \Big(k_n^2 + k_p^2 + k_e^2 + 2E_p^* E_e - E_\nu^2 - 2k_n(k_p z_p + k_e z_e)\Big)\Big(E_n^* E_\nu + k_n(k_p z_p + k_e z_e - k_n)\Big) \ , \tag{B.23}$$

$$F_3 = m_n^{*2}\Big(k_e^2 - k_n^2 - k_p^2 + 2E_e E_\nu + E_\nu^2 + 2k_n k_p z_p\Big) \ . \tag{B.24}$$

Limits of angular integration To speed up the numerical evaluation of (B.20) we implement the theta function as limits on the range of integration over z_p and z_e. The condition

$S > |E_\nu^2 - R|$ can be written (using (B.15), (B.16)) as

$$|a + bz_e| < c\sqrt{1 - z_e^2} \ , \tag{B.25}$$

$$\text{where} \quad a \equiv q^2 - k_n^2 - k_p^2 - k_e^2 + 2k_n k_p z_p \ , \tag{B.26}$$

$$b \equiv 2k_e(k_n - k_p z_p) \ , \tag{B.27}$$

$$c \equiv 2k_e k_p \sqrt{1 - z_p^2} \ . \tag{B.28}$$

The inequality (B.25) is obeyed for $z_e^- < z_e < z_e^+$ where

$$z_e^\pm = \frac{-ab \pm c\sqrt{c^2 + b^2 - a^2}}{b^2 + c^2} \ . \tag{B.29}$$

Note that if the roots are real then they are always within the physical range $z_e \in [-1, 1]$. We can therefore put bounds on z_p by requiring that (B.29) has real roots,

$$\begin{aligned} & c^2 + b^2 > a^2 \\ \Rightarrow \ & 2k_p E_\nu > |E_\nu^2 + k_e^2 - k_n^2 - k_p^2 + 2k_n k_p z_p| \, . \end{aligned} \tag{B.30}$$

This means that $z_p^- < z_p < z_p^+$, where

$$z_p^\pm = \frac{k_n^2 + k_p^2 - k_e^2 - E_\nu^2 \pm 2k_e E_\nu}{2k_n k_p} \ . \tag{B.31}$$

In this case, however, these bounds are not necessarily within the physical range $z_p \in [-1, 1]$, so the true bounds on the z_p integral are

$$[z_p^{\min}, z_p^{\max}] = [z_p^+, z_p^-] \cap [-1, 1] \, . \tag{B.32}$$

We can now write the angular integral as

$$I = 4E_\nu \Theta(E_\nu) \int_{z_p^{\min}}^{z_p^{\max}} dz_p \int_{z_e^-}^{z_e^+} dz_e \frac{\mathcal{M}_{\phi_0}}{\sqrt{S^2 - (E_\nu^2 - R)^2}} \ . \tag{B.33}$$

Using this in (B.10) we obtain

$$\begin{aligned} \Gamma_{\rm nd} = \frac{G^2}{16\pi^6} \int_0^\infty dk_n \int_0^{k_p^{\max}} dk_p \int_0^{k_e^{\max}} dk_e \, k_n^2 k_p^2 k_e^2 f_n (1-f_p)(1-f_e) \\ \Theta(E_\nu) \int_{z_p^{\min}}^{z_p^{\max}} dz_p \int_{z_e^-}^{z_e^+} dz_e \frac{4E_\nu \mathcal{M}_{\phi_0}}{\sqrt{S^2 - (E_\nu^2 - R)^2}} \ . \end{aligned} \tag{B.34}$$

The second line corresponds to the I integral (B.11), (B.33). It is natural to group a factor of E_ν with $\mathcal{M}_{\phi_0}$ to cancel the factor of E_ν in the denominator (B.21) which can cause numerical problems at the edge of the kinematically allowed momentum range where $E_\nu \to 0$.

The neutron decay rate can therefore be computed as a 5-dimensional momentum integral (B.34), obtaining the integration ranges from (B.12), (B.13), (B.32), and (B.29), the matrix element from (B.21), and the Jacobian (square root denominator) from (B.15), (B.16).

Appendix C

Modified Urca neutron decay rate

The matrix element is (4.16) in [3, 117]

$$\left(s\frac{\sum|M_n|^2}{2^6E_n^*E_p^*E_eE_\nu E_{N_1}^*E_{N_2}^*}\right)=42G^2\frac{f^4}{m_\pi^4}\frac{g_A^2}{E_e^2}\frac{k_{Fn}^4}{(k_{Fn}^2+m_\pi^2)^2}\,, \tag{C.1}$$

where $f\approx 1$ is the N-π coupling and $s=1/2$ for the identical particles. The conventional way of doing the integral is to divide the integral into an energy integral and an angular integral (termed "phase space decomposition" [61])

$$\int dk_n^3dk_p^3dk_e^3dk_\nu^3dk_{N_1}^3dk_{N_2}^3=\int dk_ndk_pdk_edk_\nu dk_{N_1}dk_{N_2}k_n^2k_p^2k_e^2k_\nu^2k_{N_1}^2k_{N_2}^2\times\int d\Omega_nd\Omega_pd\Omega_ed\Omega_\nu d\Omega_{N_1}d\Omega_{N_2}\,. \tag{C.2}$$

We use relativistic dispersion relations for nucleons

$$E_N=\sqrt{k^2+m_N^{*^2}}+U_N\,, \tag{C.3}$$

where U is the mean field contribution to the energy. We define $E^* \equiv \sqrt{k^2 + m^{*2}}$, then $dE^* = kdk/E^*$. We use ultra-relativistic dispersion relations for electron and neutrino,

$$E = k\,, \tag{C.4}$$

then $dE = dk$ (the electron mass $m_e = 0.511\,\mathrm{MeV}$ is negligible compared to its momentum). Therefore, we can convert the momentum integral to an energy integral, and the rate integral becomes

$$\begin{aligned}\Gamma_{mU,nd(n)} = \frac{42G^2 g_A^2 f^4}{(2\pi)^{14} m_\pi^4} \int & d\Omega_n d\Omega_p d\Omega_e d\Omega_\nu d\Omega_{N_1} d\Omega_{N_2} \\ & \times \delta^{(3)}(\vec{k}_n + \vec{k}_{N_1} - \vec{k}_p - \vec{k}_e - \vec{k}_{N_2}) k_n^2 k_p^2 k_e^2 k_\nu^2 k_{N_1}^2 k_{N_2}^2 \frac{1}{E_e^2} \frac{k_{Fn}^4}{(k_{Fn}^2 + m_\pi^2)^2} \\ & \times \int dE_n^* dE_p^* dE_e dE_\nu dE_{N_1}^* dE_{N_2}^* \frac{E_n^*}{k_n} \frac{E_p^*}{k_p} \frac{E_{N_1}^*}{k_{N_1}} \frac{E_{N_2}^*}{k_{N_2}} \\ & \times \delta(E_n + E_{N_1} - E_p - E_e - E_\nu - E_{N_2}) f_n f_{N_1} (1 - f_p)(1 - f_e)(1 - f_{N_2})\,. \end{aligned} \tag{C.5}$$

Notice that it is most common to set $\vec{k}_\nu = 0$ in the momentum conserving delta function but keep E_ν in the energy delta function.

In the Fermi surface approximation, we set all momenta to Fermi momenta and we will have $E_e = k_e = k_{Fe}$, $k_\nu = E_\nu$.

Now, the rate integral becomes

$$\begin{aligned}\Gamma_{mU,nd(n)} = & \frac{42G^2 g_A^2 f^4}{(2\pi)^{14} m_\pi^4} k_{Fn}^2 k_{Fp}^2 k_{Fe}^2 k_{F_{N_1}}^2 k_{F_{N_2}}^2 \frac{1}{k_{Fe}^2} \frac{k_{Fn}^4}{(k_{Fn}^2 + m_\pi^2)^2} \frac{E_n^*}{k_{Fn}} \frac{E_p^*}{k_{Fp}} \frac{E_{F_{N_1}}^*}{k_{F_{N_2}}} \frac{E_{N_2}^*}{k_{N_2}} \\ & \times \int d\Omega_n d\Omega_p d\Omega_e d\Omega_\nu d\Omega_{N_1} d\Omega_{N_2} \delta^{(3)}(\vec{k}_n + \vec{k}_{N_1} - \vec{k}_p - \vec{k}_e - \vec{k}_{N_2}) \\ & \times \int dE_n^* dE_p^* dE_e dE_\nu dE_{N_1}^* dE_{N_2}^* E_\nu^2 f_n f_{N_1} (1 - f_p)(1 - f_e)(1 - f_{N_2}) \\ & \times \delta(E_n^* + E_{N_1}^* - E_p^* - E_e - E_\nu - E_{N_2}^* + (U_n - U_p)) \,. \end{aligned} \tag{C.6}$$

For the energy integral, we do a change of variable,

$$x = \frac{E^* - \mu^*}{T} \,, \tag{C.7}$$

then, $dx = (1/T)dE^*$ and $\mu = 0$ for the neutrino. For the integral bounds, we have

$$\int_{m^*}^{+\infty} dE^* = T \int_{(m^* - \mu^*)/T}^{+\infty} dx = T \int_{-(\mu^* - m^*)/T}^{+\infty} dx \approx T \int_{-\infty}^{+\infty} dx \,, \tag{C.8}$$

where the approximation is valid because $\mu^* \gg T$. For neutrino, $\mu = 0$ and $m = 0$, so the

lower bound is 0. Then, the energy integral, which we denote as I, becomes

$$\begin{aligned}
I \equiv & \int dE_n^* dE_p^* dE_e dE_\nu dE_{N_1}^* dE_{N_2}^* E_\nu^2 f_n f_{N_1}(1-f_p)(1-f_e)(1-f_{N_2}) \\
& \times \delta(E_n^* + E_{N_1}^* - E_p^* - E_e - E_\nu - E_{N_2}^* + (U_n - U_p)) \\
= & T^7 \int dx_n dx_p dx_e dx_\nu dx_{N_1} dx_{N_2}\, x_\nu^2 f(x_n) f(x_{N_1})(1-f(x_p))(1-f(x_e)) \\
& \times (1-f(x_{N_2}))\delta(x_n + x_{N_1} - x_p - x_e - x_\nu - x_{N_2} + \frac{\mu_n - \mu_p - \mu_e}{T}) \\
= & T^7 \int_0^{+\infty} dx_\nu x_\nu^2 \int_{-\infty}^{+\infty} dx_n dx_p dx_e dx_{N_1} dx_{N_2}\, f(x_n) f(x_{N_1}) f(-x_p) f(-x_e) \\
& \times f(-x_{N_2})\delta(x_n + x_{N_1} - x_p - x_e - x_\nu - x_{N_2} + \frac{\mu_n - \mu_p - \mu_e}{T}) \\
= & T^7 \int_0^{+\infty} dx_\nu x_\nu^2 \int_{-\infty}^{+\infty} dx_n dx_p dx_e dx_{N_1} dx_{N_2}\, f(x_n) f(x_{N_1}) f(x_p) f(x_e) f(x_{N_2}) \\
& \times \delta(x_n + x_{N_1} + x_p + x_e - x_\nu + x_{N_2} + \frac{\mu_n - \mu_p - \mu_e}{T})\,. \qquad \text{(C.9)}
\end{aligned}$$

One can use Mathematica to obtain an analytical expression,

$$I = \frac{1}{12} F(\xi)\,, \qquad \text{(C.10)}$$

where $\xi \equiv (\mu_n - \mu_p - \mu_e)/T$, and

$$\begin{aligned}
F(\xi) \equiv & -(\xi^4 + 10\pi^2\xi^2 + 9\pi^4)\mathrm{Li}_3(-e^\xi) + 12(\xi^3 + 5\pi^2\xi)\mathrm{Li}_4(-e^\xi) \\
& - 24(3\xi^2 + 5\pi^2)\mathrm{Li}_5(-e^\xi) + 240\xi\mathrm{Li}_6(-e^\xi) - 360\mathrm{Li}_7(-e^\xi)\,. \qquad \text{(C.11)}
\end{aligned}$$

For the angular integral, we can look up [89], which calculated the n-dimensional angular integral for n=3,4,5, and obtain

$$A = \frac{32\pi(2\pi)^4}{k_n^3}\theta_n\,, \qquad \text{(C.12)}$$

where

$$\theta_n = \begin{cases} 1 & k_{Fn} > k_{Fp} + k_{Fe} \\ 1 - \dfrac{3}{8}\dfrac{(k_{Fp} + k_{Fe} - k_{Fn})^2}{k_{Fp}k_{Fe}} & k_{Fn} < k_{Fp} + k_{Fe}\,. \end{cases} \tag{C.13}$$

Therefore, the neutron decay modified Urca rate with n-spectator under Fermi surface approximation is

$$\Gamma_{mU,nd(n)}(\xi) = \frac{7}{64\pi^9} G^2 g_A^2 f^4 \frac{(E^*_{Fn})^3 E^*_{Fp}}{m_\pi^4} \frac{k_{Fn}^4 k_{Fp}}{(k_{Fn}^2 + m_\pi^2)^2} F(\xi) T^7 \theta_n\,. \tag{C.14}$$

Similarly, we can calculate the electron capture mU rate with n-spectator

$$\Gamma_{mU,ec(n)}(\xi) = \Gamma_{mU,nd(n)}(-\xi)\,. \tag{C.15}$$

For p-spectator processes, the matrix element is

$$\left(s \frac{\sum |M_p|^2}{2^6 E_n^* E_p^* E_e E_\nu E_{N_1}^* E_{N_2}^*}\right) = 48 G^2 \frac{f^4}{m_\pi^4} \frac{g_A^2}{E_e^2} \frac{(k_{Fn} - k_{Fp})^4}{((k_{Fn} - k_{Fp})^2 + m_\pi^2)^2}\,, \tag{C.16}$$

where we still have $s = 1/2$. Then we have the mU rates with p-spectator

$$\Gamma_{mU,nd(p)}(\xi) = \frac{1}{64\pi^9} G^2 g_A^2 f^4 \frac{(E^*_{Fp})^3 E^*_{Fn}}{m_\pi^4} \frac{(k_{Fn} - k_{Fp})^4 k_{Fn}}{((k_{Fn} - k_{Fp})^2 + m_\pi^2)^2} F(\xi) T^7 \theta_p\,, \tag{C.17}$$

$$\Gamma_{mU,ec(p)}(\xi) = \Gamma_{mU,nd(p)}(-\xi)\,, \tag{C.18}$$

where

$$\theta_p = \begin{cases} 0 & k_{Fn} > 3k_{Fp} + k_{Fe} \\ \dfrac{(3k_{Fp} + k_{Fe} - k_{Fn})^2}{k_{Fn}k_{Fe}} & 3k_{Fp} + k_{Fe} > k_{Fn} > 3k_{Fp} - k_{Fe} \\ \dfrac{4(3k_{Fp} - k_{Fn})}{k_{Fn}} & 3k_{Fp} - k_{Fe} > k_{Fn} > k_{Fp} + k_{Fe} \\ 2 + \dfrac{3(2k_{Fp} - k_{Fn})}{k_{Fe}} - \dfrac{3(k_{Fp} - k_{Fe})^2}{k_{Fn}k_{Fe}} & k_{Fn} < k_{Fp} + k_{Fe}\,. \end{cases} \tag{C.19}$$

Appendix D

Cold beta equilibrium

Previous calculations of the bulk viscosity of neutrino-transparent matter assumed that isospin equilibrium occurs when $\mu_n = \mu_p + \mu_e$, i.e. $\mu_I^{\rm eq} = 0$ for any n_B, T. As we have described, this is only valid when the temperature is below about 1 MeV. In this low-temperature regime the isospin creation rate depends only on $\Delta\mu_I$,

$$\Gamma_I = \frac{d\Gamma}{d\mu_I}\Delta\mu_I = \frac{d\Gamma}{d\mu_I}\left(\left.\frac{\partial\mu_I}{\partial x_I}\right|_{n_B}\Delta x_I + \left.\frac{\partial\mu_I}{\partial n_B}\right|_{x_I}\Delta n_B\right) \tag{D.1}$$

To make contact with earlier results we define

$$\chi_{n_B} \equiv -n_B\left.\frac{\partial\mu_I}{\partial n_B}\right|_{x_I} \tag{D.2}$$

and

$$\chi_{x_I} \equiv \frac{1}{\bar{n}_B}\left.\frac{\partial\mu_I}{\partial x_I}\right|_{n_B} . \tag{D.3}$$

Then comparing (D.1) with (3.8) and (3.9) we can write γ_B in terms of γ_I,

$$\begin{aligned} \gamma_I &= -\chi_{x_I}\frac{d\Gamma}{d\mu_I} \\ \gamma_B &= \frac{1}{\bar{n}_B}\frac{\chi_{n_B}}{\chi_{x_I}}\,\gamma_I \ . \end{aligned} \tag{D.4}$$

Using the thermodynamic identity (E.1) we can then write the bulk viscosity (3.20) as

$$\zeta_{\rm cold} = \frac{\chi_{n_B}^2}{\chi_{x_I}} \, \frac{\gamma_I}{\gamma_I^2 + \omega^2} \, . \tag{D.5}$$

This agrees with previous calculations such as Eq. (128) of Ref. [88].

Appendix E

A relevant thermodynamic identity

In this appendix we show that

$$\frac{1}{n_B}\frac{\partial p}{\partial x_I}\bigg|_{n_B,T} = n_B \frac{\partial \mu_I}{\partial n_B}\bigg|_{x_I,T} . \tag{E.1}$$

We start by observing that

$$\frac{1}{n_B}\frac{\partial p}{\partial x_I}\bigg|_{n_B,T} = \frac{\partial p}{\partial n_I}\bigg|_{n_B,T} . \tag{E.2}$$

Using the thermodynamic expression for pressure, $p = \mu_B n_B + \mu_I n_I + Ts - \varepsilon(n_B, n_I, s)$, and the relation

$$\begin{aligned} \frac{\partial \varepsilon}{\partial n_I}\bigg|_{n_B,T} &= \frac{\partial \varepsilon}{\partial n_I}\bigg|_{n_B,s} + \frac{\partial s}{\partial n_I}\bigg|_{n_B,T}\frac{\partial \varepsilon}{\partial s}\bigg|_{n_B,n_I} \\ &= \mu_I + T\,\frac{\partial s}{\partial n_I}\bigg|_{n_B,T} \end{aligned} \tag{E.3}$$

it follows that

$$\frac{\partial p}{\partial n_I}\bigg|_{n_B,T} = n_B \frac{\partial \mu_B}{\partial n_I}\bigg|_{n_B,T} + n_I \frac{\partial \mu_I}{\partial n_I}\bigg|_{n_B,T} . \tag{E.4}$$

We now use the Maxwell relation

$$\frac{\partial \mu_B}{\partial n_I}\bigg|_{n_B,T} = \frac{\partial^2 \varepsilon}{\partial n_B \partial n_I}\bigg|_{T} = \frac{\partial \mu_I}{\partial n_B}\bigg|_{n_I,T} , \tag{E.5}$$

where derivatives with respect to n_B are taken at constant n_I and vice versa, so (E.4) becomes

$$\begin{aligned} \left.\frac{\partial p}{\partial n_I}\right|_{n_B,T} &= n_B \left.\frac{\partial \mu_I}{\partial n_B}\right|_{n_I,T} + n_I \left.\frac{\partial \mu_I}{\partial n_I}\right|_{n_B,T} \\ &= n_B \left.\frac{\partial \mu_I}{\partial n_B}\right|_{x_I,T} , \end{aligned} \tag{E.6}$$

which proves Eq. (E.2) and therefore Eq. (E.1)

Bibliography

[1] Mark G. Alford, Andreas Schmitt, Krishna Rajagopal, and Thomas Schäfer. Color superconductivity in dense quark matter. *Rev. Mod. Phys.*, 80:1455–1515, 2008.

[2] B. L. Friman and O. V. Maxwell. Neutron Star Neutrino Emissivities. *Astrophys. J.*, 232:541–557, 1979.

[3] D. G. Yakovlev, A. D. Kaminker, Oleg Y. Gnedin, and P. Haensel. Neutrino emission from neutron stars. *Phys. Rept.*, 354:1, 2001.

[4] P. S. Shternin, M. Baldo, and P. Haensel. In-medium enhancement of the modified Urca neutrino reaction rates. *Phys. Lett. B*, 786:28–34, 2018.

[5] Andrew W. Steiner, Matthias Hempel, and Tobias Fischer. Core-collapse supernova equations of state based on neutron star observations. *Astrophys. J.*, 774:17, 2013.

[6] Kenji Fukushima and Tetsuo Hatsuda. The phase diagram of dense QCD. *Rept. Prog. Phys.*, 74:014001, 2011.

[7] Kenji Fukushima and Chihiro Sasaki. The phase diagram of nuclear and quark matter at high baryon density. *Prog. Part. Nucl. Phys.*, 72:99–154, 2013.

[8] Mark G. Alford, Krishna Rajagopal, and Frank Wilczek. Color superconductivity and signs of its formation. *Nucl. Phys. A*, 638:515C–518C, 1998.

[9] Eemeli Annala. *From QCD to Neutron Stars and Back : Probing the Fundamental Properties of Dense Matter*. PhD thesis, Helsinki U., 2020.

[10] Gordon Baym, Tetsuo Hatsuda, Toru Kojo, Philip D. Powell, Yifan Song, and Tatsuyuki Takatsuka. From hadrons to quarks in neutron stars: a review. *Rept. Prog. Phys.*, 81(5):056902, 2018.

[11] D. T. Son and Misha A. Stephanov. QCD at finite isospin density. *Phys. Rev. Lett.*, 86:592–595, 2001.

[12] J. Noronha-Hostler, P. Parotto, C. Ratti, and J. M. Stafford. Lattice-based equation of state at finite baryon number, electric charge, and strangeness chemical potentials. *Physical Review C*, 100(6), December 2019.

[13] Paolo Parotto, Marcus Bluhm, Debora Mroczek, Marlene Nahrgang, Jacquelyn Noronha-Hostler, Krishna Rajagopal, Claudia Ratti, Thomas Schäfer, and Mikhail Stephanov. QCD equation of state matched to lattice data and exhibiting a critical point singularity. *Phys. Rev. C*, 101(3):034901, 2020.

[14] Joaquin Grefa, Jorge Noronha, Jacquelyn Noronha-Hostler, Israel Portillo, Claudia Ratti, and Romulo Rougemont. Hot and dense quark-gluon plasma thermodynamics from holographic black holes. *Phys. Rev. D*, 104(3):034002, 2021.

[15] V. A. Dexheimer and S. Schramm. Novel approach to modeling hybrid stars. *Physical Review C*, 81(4), April 2010.

[16] Xingfu Du, Andrew W. Steiner, and Jeremy W. Holt. Hot and dense homogeneous nucleonic matter constrained by observations, experiment, and theory. *Physical Review C*, 99(2), February 2019.

[17] J. W. Holt, N. Kaiser, and T. R. Whitehead. Tensor fermi liquid parameters in nuclear matter from chiral effective field theory. *Physical Review C*, 97(5), May 2018.

[18] S. Borsányi, Z. Fodor, J. N. Guenther, R. Kara, S. D. Katz, P. Parotto, A. Pásztor, C. Ratti, and K. K. Szabó. Lattice QCD equation of state at finite chemical potential from an alternative expansion scheme. *Phys. Rev. Lett.*, 126(23):232001, 2021.

[19] Keitaro Nagata. Finite-density lattice QCD and sign problem: Current status and open problems. *Prog. Part. Nucl. Phys.*, 127:103991, 2022.

[20] Philippe de Forcrand. Simulating QCD at finite density. *PoS*, LAT2009:010, 2009.

[21] Marco Cristoforetti, Francesco Di Renzo, and Luigi Scorzato. New approach to the sign problem in quantum field theories: High density QCD on a Lefschetz thimble. *Phys. Rev. D*, 86:074506, 2012.

[22] Z. Fodor and S. D. Katz. A New method to study lattice QCD at finite temperature and chemical potential. *Phys. Lett. B*, 534:87–92, 2002.

[23] Oleg Komoltsev and Aleksi Kurkela. How Perturbative QCD Constrains the Equation of State at Neutron-Star Densities. *Phys. Rev. Lett.*, 128(20):202701, 2022.

[24] John Collins. *Foundations of Perturbative QCD*, volume 32 of *Cambridge Monographs on Particle Physics, Nuclear Physics and Cosmology*. Cambridge University Press, 7 2023.

[25] Jacopo Ghiglieri, Aleksi Kurkela, Michael Strickland, and Aleksi Vuorinen. Perturbative Thermal QCD: Formalism and Applications. *Phys. Rept.*, 880:1–73, 2020.

[26] Raymond Brock et al. Handbook of perturbative QCD: Version 1.0. *Rev. Mod. Phys.*, 67:157–248, 1995.

[27] Willem Hendrik Dickhoff and Dimitri VY Van Neck. *Many-body theory exposed! Propagator description of quantum mechanics in many-body systems*. World Scientific Publishing Company, 2008.

[28] R. Machleidt and D. R. Entem. Chiral effective field theory and nuclear forces. *Phys. Rept.*, 503:1–75, 2011.

[29] E. Epelbaum, W. Glockle, and Ulf-G. Meissner. The Two-nucleon system at next-to-next-to-next-to-leading order. *Nucl. Phys. A*, 747:362–424, 2005.

[30] Evgeny Epelbaum. Few-nucleon forces and systems in chiral effective field theory. *Prog. Part. Nucl. Phys.*, 57:654–741, 2006.

[31] Pasi Huovinen and Pter Petreczky. QCD Equation of State and Hadron Resonance Gas. *Nucl. Phys. A*, 837:26–53, 2010.

[32] V. Vovchenko, D. V. Anchishkin, and M. I. Gorenstein. Hadron Resonance Gas Equation of State from Lattice QCD. *Phys. Rev. C*, 91(2):024905, 2015.

[33] N. Brambilla et al. QCD and Strongly Coupled Gauge Theories: Challenges and Perspectives. *Eur. Phys. J. C*, 74(10):2981, 2014.

[34] A. Bazavov et al. The chiral and deconfinement aspects of the QCD transition. *Phys. Rev. D*, 85:054503, 2012.

[35] Benjamin Svetitsky and Laurence G. Yaffe. Critical Behavior at Finite Temperature Confinement Transitions. *Nucl. Phys. B*, 210:423–447, 1982.

[36] Philippe Chomaz. The nuclear liquid gas phase transition and phase coexistence. *AIP Conf. Proc.*, 610(1):167, 2002.

[37] Kenji Fukushima, Jan Horak, Jan M. Pawlowski, Nicolas Wink, and Carl Philipp Zelle. The nuclear liquid-gas transition in QCD. *arXiv:2308.16594 [nucl-th]*, 8 2023.

[38] H. T. Cromartie et al. Relativistic Shapiro delay measurements of an extremely massive millisecond pulsar. *Nature Astron.*, 4(1):72–76, 2019.

[39] Thomas E. Riley et al. A NICER View of the Massive Pulsar PSR J0740+6620 Informed by Radio Timing and XMM-Newton Spectroscopy. *Astrophys. J. Lett.*, 918(2):L27, 2021.

[40] N. Chamel and P. Haensel. Physics of Neutron Star Crusts. *Living Rev. Rel.*, 11:10, 2008.

[41] Jurgen Schaffner-Bielich. *Compact Star Physics*. Cambridge University Press, 2020.

[42] B.P. Abbott et al. Observation of gravitational waves from a binary black hole merger. *Phys. Rev. Lett.*, 116:061102, Feb 2016.

[43] B. P. Abbott et al. GWTC-1: A Gravitational-Wave Transient Catalog of Compact Binary Mergers Observed by LIGO and Virgo during the First and Second Observing Runs. *Phys. Rev. X*, 9(3):031040, 2019.

[44] R. Abbott et al. GWTC-2: Compact Binary Coalescences Observed by LIGO and Virgo During the First Half of the Third Observing Run. *Phys. Rev. X*, 11:021053, 2021.

[45] R. Abbott et al. GW190814: Gravitational Waves from the Coalescence of a 23 Solar Mass Black Hole with a 2.6 Solar Mass Compact Object. *Astrophys. J. Lett.*, 896(2):L44, 2020.

[46] R. Abbott et al. Observation of Gravitational Waves from Two Neutron Star–Black Hole Coalescences. *Astrophys. J. Lett.*, 915(1):L5, 2021.

[47] David Radice, Sebastiano Bernuzzi, and Albino Perego. The Dynamics of Binary Neutron Star Mergers and GW170817. *Ann. Rev. Nucl. Part. Sci.*, 70:95–119, 2020.

[48] James M. Lattimer. The nuclear equation of state and neutron star masses. *Ann. Rev. Nucl. Part. Sci.*, 62:485–515, 2012.

[49] Feryal Ozel, Dimitrios Psaltis, Tolga Guver, Gordon Baym, Craig Heinke, and Sebastien Guillot. The Dense Matter Equation of State from Neutron Star Radius and Mass Measurements. *Astrophys. J.*, 820(1):28, 2016.

[50] F. J. Fattoyev, J. Piekarewicz, and C. J. Horowitz. Neutron Skins and Neutron Stars in the Multimessenger Era. *Phys. Rev. Lett.*, 120(17):172702, 2018.

[51] Kentaro Takami, Luciano Rezzolla, and Luca Baiotti. Constraining the Equation of State of Neutron Stars from Binary Mergers. *Phys. Rev. Lett.*, 113(9):091104, 2014.

[52] Chun Huang, Geert Raaijmakers, Anna L. Watts, Laura Tolos, and Constanca Providencia. Constraining a relativistic mean field model using neutron star mass-radius measurements I: Nucleonic models. *arXiv:2303.17518 [astro-ph.HE]*, 3 2023.

[53] Reed Essick, Isaac Legred, Katerina Chatziioannou, Sophia Han, and Philippe Landry. Phase transition phenomenology with nonparametric representations of the neutron star equation of state. *Phys. Rev. D*, 108(4):043013, 2023.

[54] Reed Essick, Philippe Landry, and Daniel E. Holz. Nonparametric Inference of Neutron Star Composition, Equation of State, and Maximum Mass with GW170817. *Phys. Rev. D*, 101(6):063007, 2020.

[55] Mark G. Alford, Luke Bovard, Matthias Hanauske, Luciano Rezzolla, and Kai Schwenzer. Viscous Dissipation and Heat Conduction in Binary Neutron-Star Mergers. *Phys. Rev. Lett.*, 120(4):041101, 2018.

[56] N. K. Glendenning. *Compact stars: Nuclear physics, particle physics, and general relativity*. Springer, 1997.

[57] Andreas Schmitt. Dense matter in compact stars. *Lecture Notes in Physics*, 2010.

[58] M. Dutra, O. Lourenco, S. S. Avancini, B. V. Carlson, A. Delfino, D. P. Menezes, C. Providencia, S. Typel, and J. R. Stone. Relativistic Mean-Field Hadronic Models under Nuclear Matter Constraints. *Phys. Rev. C*, 90(5):055203, 2014.

[59] F. J. Fattoyev, C. J. Horowitz, J. Piekarewicz, and G. Shen. Relativistic effective interaction for nuclei, giant resonances, and neutron stars. *Phys. Rev. C*, 82:055803, 2010.

[60] Richard C. Tolman. Static solutions of Einstein's field equations for spheres of fluid. *Phys. Rev.*, 55:364–373, 1939.

[61] S. L. Shapiro and S. A. Teukolsky. *Black holes, white dwarfs, and neutron stars: The physics of compact objects*. Wiley, 1983.

[62] Mark Alford, Arus Harutyunyan, and Armen Sedrakian. Bulk viscosity of baryonic matter with trapped neutrinos. *Phys. Rev. D*, 100(10):103021, 2019.

[63] Mark Alford, Arus Harutyunyan, and Armen Sedrakian. Bulk Viscous Damping of Density Oscillations in Neutron Star Mergers. *Particles*, 3:500–517, 2020.

[64] Mark Alford, Arus Harutyunyan, and Armen Sedrakian. Bulk viscosity from Urca processes: npeμ matter in the neutrino-trapped regime. *Phys. Rev. D*, 104(10):103027, 2021.

[65] Mark Alford, Arus Harutyunyan, and Armen Sedrakian. Bulk Viscosity of Relativistic npeμ Matter in Neutron-Star Mergers. *Particles*, 5(3):361–376, 2022.

[66] Akihiko Monnai, BjÃ¶rn Schenke, and Chun Shen. Equation of state at finite densities for qcd matter in nuclear collisions. *Physical Review C*, 100(2), August 2019.

[67] Mark G. Alford, Alexander Haber, Steven P. Harris, and Ziyuan Zhang. Beta Equilibrium Under Neutron Star Merger Conditions. *Universe*, 7(11):399, 2021.

[68] Mark Alford, Arus Harutyunyan, and Armen Sedrakian. Bulk viscosity from Urca processes: npeμ matter in the neutrino-transparent regime. *Phys. Rev. D*, 108(8):083019, 2023.

[69] Albino Perego, Sebastiano Bernuzzi, and David Radice. Thermodynamics conditions of matter in neutron star mergers. *Eur. Phys. J. A*, 55(8):124, 2019.

[70] Andrea Endrizzi, Albino Perego, Francesco M. Fabbri, Lorenzo Branca, David Radice, Sebastiano Bernuzzi, Bruno Giacomazzo, Francesco Pederiva, and Alessandro Lovato. Thermodynamics conditions of matter in the neutrino decoupling region during neutron star mergers. *Eur. Phys. J. A*, 56(1):15, 2020.

[71] Matthias Hanauske, Jan Steinheimer, Anton Motornenko, Volodymyr Vovchenko, Luke Bovard, Elias R. Most, L.Jens Papenfort, Stefan Schramm, and Horst StÃ¶cker. Neutron Star Mergers: Probing the EoS of Hot, Dense Matter by Gravitational Waves. *Particles*, 2(1):44–56, 2019.

[72] Elias R. Most, Steven P. Harris, Christopher Plumberg, Mark G. Alford, Jorge Noronha, Jacquelyn Noronha-Hostler, Frans Pretorius, Helvi Witek, and Nicolás Yunes. Projecting the likely importance of weak-interaction-driven bulk viscosity in neutron star mergers. *Mon. Not. Roy. Astron. Soc.*, 509(1):1096–1108, 2021.

[73] Mark G. Alford and Steven P. Harris. Beta equilibrium in neutron star mergers. *Phys. Rev.*, C98(6):065806, 2018.

[74] Tobias Fischer, Gang Guo, Alan A. Dzhioev, Gabriel Martinez-Pinedo, Meng-Ru Wu, Andreas Lohs, and Yong-Zhong Qian. Neutrino signal from proto-neutron star evolution: Effects of opacities from charged-current–neutrino interactions and inverse neutron decay. *Phys. Rev. C*, 101(2):025804, 2020.

[75] Luke F. Roberts and Sanjay Reddy. Charged current neutrino interactions in hot and dense matter. *Phys. Rev.*, C95(4):045807, 2017.

[76] Wei-jie Fu, Guo-hua Wang, and Yu-xin Liu. Electron Capture and Its Reverse Process in Hot and Dense Astronuclear Matter. *Astrophys. J.*, 678:1517–1529, 2008.

[77] Sanjay Reddy, Madappa Prakash, and James M Lattimer. Neutrino interactions in hot and dense matter. *Phys. Rev. D*, 58:013009, 1998.

[78] Roland Oechslin, H. T. Janka, and A. Marek. Relativistic neutron star merger simulations with non-zero temperature equations of state. 1. Variation of binary parameters and equation of state. *Astron. Astrophys.*, 467:395, 2007.

[79] Luca Baiotti and Luciano Rezzolla. Binary neutron star mergers: a review of Einstein's richest laboratory. *Rept. Prog. Phys.*, 80(9):096901, 2017.

[80] Carolyn Raithel, Vasileios Paschalidis, and Feryal Özel. Realistic finite-temperature effects in neutron star merger simulations. *Phys. Rev. D*, 104(6):063016, 2021.

[81] L. B. Leinson and A. Perez. Relativistic direct Urca processes in cooling neutron stars. *Phys. Lett. B*, 518:15, 2001. [Erratum: Phys.Lett.B 522, 358–358 (2001)].

[82] Wen-Bo Ding, Zhan-Qiang Qi, Jia-Wei Hou, Geng Mi, Tmurbagan Bao, Zi Yu, Guang-Zhou Liu, and En-Guang Zhao. Relativistic Correction on Neutrino Emission from Neutron Stars in Various Parameter Sets. *Commun. Theor. Phys.*, 66(4):474–478, 2016.

[83] Qi Zhan-qiang, Ding Wen-bo, Zhang Cheng-min, and Hou Jia-wei. Relativistic Correction of Neutrino Emission in Neutron Stars. *Chin. Astron. Astrophys.*, 42:69–80, 2018.

[84] A Wadhwa, V K Gupta, S Singh, and J D Anand. On the cooling of neutron stars. *Journal of Physics G: Nuclear and Particle Physics*, 21(8):1137–1147, aug 1995.

[85] Mark G. Alford and Steven P. Harris. Damping of density oscillations in neutrino-transparent nuclear matter. *Phys. Rev.*, C100(3):035803, 2019.

[86] D. G. Yakovlev, M. E. Gusakov, and P. Haensel. Bulk viscosity in a neutron star mantle. *Mon. Not. Roy. Astron. Soc.*, 481(4):4924–4930, 2018.

[87] Phil Arras and Nevin N. Weinberg. Urca reactions during neutron star inspiral. *Mon. Not. Roy. Astron. Soc.*, 486(1):1424–1436, 2019.

[88] Andreas Schmitt and Peter Shternin. Reaction rates and transport in neutron stars. *Astrophys. Space Sci. Libr.*, 457:455–574, 2018.

[89] A. D. Kaminker, D. G. Yakovlev, and P. Haensel. Theory of neutrino emission from nucleon-hyperon matter in neutron stars: angular integrals. *Astrophys. Space Sci.*, 361(8):267, 2016.

[90] E. E. Kolomeitsev and D. N. Voskresensky. Viscosity of neutron star matter and r-modes in rotating pulsars. *Phys. Rev. C*, 91(2):025805, 2015.

[91] Peng Yin and Wei Zuo. Three-body force effect on neutrino emissivities of neutron stars within the framework of the Brueckner-Hartree-Fock approach. *Phys. Rev. C*, 88(1):015804, 2013.

[92] Mark G. Alford, Simin Mahmoodifar, and Kai Schwenzer. Large amplitude behavior of the bulk viscosity of dense matter. *J. Phys. G*, 37:125202, 2010.

[93] Shu-Hua Yang, Xiao-Ping Zheng, and Chun-Mei Pi. Radiative viscosity of neutron stars. *Phys. Lett. B*, 683:255–258, 2010.

[94] Michael E. Gusakov, D. G. Yakovlev, P. Haensel, and Oleg Y. Gnedin. Direct Urca process in a neutron star mantle. *Astron. Astrophys.*, 421:1143–1148, 2004.

[95] P. Haensel and R. Schaeffer. Bulk viscosity of hot-neutron-star matter from direct URCA processes. *Phys. Rev. D*, 45:4708–4712, 1992.

[96] P. Haensel. Non-equilibrium neutrino emissivities and opacities of neutron star matter. *Astron. Astrophys.*, 262(1):131–137, August 1992.

[97] J. M. Lattimer, M. Prakash, C. J. Pethick, and P. Haensel. Direct URCA process in neutron stars. *Phys. Rev. Lett.*, 66:2701–2704, 1991.

[98] J. Piekarewicz and G. Toledo Sanchez. Proton fraction in the inner neutron-star crust. *Phys. Rev. C*, 85:015807, 2012.

[99] W. Greiner, L. Neise, H. Stocker, H. Stöcker, and D. Rischke. *Thermodynamics and Statistical Mechanics*. Classical theoretical physics. Springer-Verlag, 1995.

[100] Ye-Fei Yuan. Electron positron capture rates and the steady state equilibrium condition for electron-positron plasma with nucleons. *Phys. Rev. D*, 72:013007, 2005.

[101] Men-Quan Liu. Steady state equilibrium condition of npe gas and its application to astrophysics. *Research in Astronomy and Astrophysics*, 11(1):91–102, Dec 2010.

[102] Emmanuel Fonseca et al. The NANOGrav Nine-year Data Set: Mass and Geometric Measurements of Binary Millisecond Pulsars. *Astrophys. J.*, 832(2):167, 2016.

[103] John Antoniadis et al. A Massive Pulsar in a Compact Relativistic Binary. *Science*, 340:6131, 2013.

[104] Peter T. H. Pang, Ingo Tews, Michael W. Coughlin, Mattia Bulla, Chris Van Den Broeck, and Tim Dietrich. Nuclear Physics Multimessenger Astrophysics Constraints on the Neutron Star Equation of State: Adding NICER's PSR J0740+6620 Measurement. *Astrophys. J.*, 922(1):14, 2021.

[105] Edward F. Brown, Andrew Cumming, Farrukh J. Fattoyev, C. J. Horowitz, Dany Page, and Sanjay Reddy. Rapid neutrino cooling in the neutron star MXB 1659-29. *Phys. Rev. Lett.*, 120(18):182701, 2018.

[106] Spencer Beloin, Sophia Han, Andrew W. Steiner, and Khorgolkhuu Odbadrakh. Simultaneous Fitting of Neutron Star Structure and Cooling Data. *Phys. Rev. C*, 100(5):055801, 2019.

[107] J. B. Wei, G. F. Burgio, and H. J. Schulze. Neutron star cooling with microscopic equations of state. *Mon. Not. Roy. Astron. Soc.*, 484:5162, 2019.

[108] Brendan T. Reed, F. J. Fattoyev, C. J. Horowitz, and J. Piekarewicz. Implications of PREX-2 on the Equation of State of Neutron-Rich Matter. *Phys. Rev. Lett.*, 126(17):172503, 2021.

[109] Dany Page, James M. Lattimer, Madappa Prakash, and Andrew W. Steiner. Minimal cooling of neutron stars: A New paradigm. *Astrophys. J. Suppl.*, 155:623–650, 2004.

[110] Brian D. Serot and John Dirk Walecka. Recent progress in quantum hadrodynamics. *Int. J. Mod. Phys. E*, 6:515–631, 1997.

[111] Prasanta Char, Silvia Traversi, and Giuseppe Pagliara. A bayesian analysis on neutron stars within relativistic mean field models. *Particles*, 3(3):621–629, 2020.

[112] Xilin Zhang and Madappa Prakash. Hot and dense matter beyond relativistic mean field theory. *Phys. Rev. C*, 93(5):055805, 2016.

[113] Bengt Friman and Wolfram Weise. Neutron Star Matter as a Relativistic Fermi Liquid. *Phys. Rev. C*, 100:065807, 2019.

[114] Bao-An Li, Bao-Jun Cai, Lie-Wen Chen, and Jun Xu. Nucleon Effective Masses in Neutron-Rich Matter. *Prog. Part. Nucl. Phys.*, 99:29–119, 2018.

[115] L. Villain and P. Haensel. Non-equilibrium beta processes in superfluid neutron star cores. *Astron. Astrophys.*, 444:539, 2005.

[116] Frank WJ Olver, Daniel W Lozier, Ronald F Boisvert, and Charles W Clark. *NIST handbook of mathematical functions hardback and CD-ROM*. Cambridge university press, 2010.

[117] Steven P. Harris. *Transport in neutron star mergers*. PhD thesis, Washington University in Saint Louis, 2020.

[118] David Radice, Albino Perego, Kenta Hotokezaka, Steven A. Fromm, Sebastiano Bernuzzi, and Luke F. Roberts. Binary Neutron Star Mergers: Mass Ejection, Electromagnetic Counterparts and Nucleosynthesis. *Astrophys. J.*, 869(2):130, 2018.

[119] Peter Hammond, Ian Hawke, and Nils Andersson. Thermal aspects of neutron star mergers. *Phys. Rev. D*, 104(10):103006, 2021.

[120] Francois Foucart. Neutrino transport in general relativistic neutron star merger simulations. *arXiv:2209.02538 [astro-ph.HE]*, 9 2022.

[121] R. F. Sawyer. Bulk viscosity of hot neutron-star matter and the maximum rotation rates of neutron stars. *Phys. Rev. D*, 39:3804–3806, 1989.

[122] P. Haensel, K. P. Levenfish, and D. G. Yakovlev. Bulk viscosity in superfluid neutron star cores. I. direct urca processes in npe mu matter. *Astron. Astrophys.*, 357:1157–1169, 2000.

[123] P. B. Jones. Bulk viscosity of neutron star matter. *Phys. Rev. D*, 64:084003, 2001.

[124] Mikhail E. Gusakov. Bulk viscosity of superfluid neutron stars. *Phys. Rev. D*, 76:083001, 2007.

[125] Mark G. Alford, Liam Brodie, Alexander Haber, and Ingo Tews. Relativistic mean-field theories for neutron-star physics based on chiral effective field theory. *Phys. Rev. C*, 106(5):055804, 2022.

[126] P. Haensel, K. P. Levenfish, and D. G. Yakovlev. Bulk viscosity in superfluid neutron star cores. 2. Modified Urca processes in npe mu matter. *Astron. Astrophys.*, 327:130–137, 2001.

[127] T. Celora, I. Hawke, P. C. Hammond, N. Andersson, and G. L. Comer. Formulating bulk viscosity for neutron star simulations. *Phys. Rev. D*, 105(10):103016, 2022.

[128] M. Ruffert, H. T. Janka, K. Takahashi, and Gerhard Schaefer. Coalescing neutron stars: A Step towards physical models. 2. Neutrino emission, neutron tori, and gamma-ray bursts. *Astron. Astrophys.*, 319:122–153, 1997.

[129] Elias R. Most, L. Jens Papenfort, and Luciano Rezzolla. Beyond second-order convergence in simulations of magnetized binary neutron stars with realistic microphysics. *Mon. Not. Roy. Astron. Soc.*, 490(3):3588–3600, 2019.

[130] Francesco Zappa, Sebastiano Bernuzzi, David Radice, and Albino Perego. Binary neutron star merger simulations with neutrino transport and turbulent viscosity: impact of different schemes and grid resolution. *arXiv:2210.11491 [astro-ph.HE]*, 10 2022.

[131] Carlo Musolino and Luciano Rezzolla. A practical guide to a moment approach for neutrino transport in numerical relativity. *Mon. Not. Roy. Astron. Soc.*, 528(4):5952–5971, 2024.

[132] Elias R. Most, Alexander Haber, Steven P. Harris, Ziyuan Zhang, Mark G. Alford, and Jorge Noronha. Emergence of microphysical viscosity in binary neutron star post-merger dynamics. *arXiv:2207.00442 [astro-ph.HE]*, 7 2022.

[133] J. Madsen. Bulk viscosity of strange quark matter, damping of quark star vibration, and the maximum rotation rate of pulsars. *Phys. Rev. D*, 46:3290–3295, 1992.

[134] Andreas Reisenegger and Axel A. Bonacic. Bulk viscosity, r-modes, and the early evolution of neutron stars. In *International Workshop on Pulsars, AXPs and SGRs Observed with BeppoSAX and other Observatories*, 3 2003.

[135] Mark G. Alford and Alexander Haber. Strangeness-changing Rates and Hyperonic Bulk Viscosity in Neutron Star Mergers. *Phys. Rev. C*, 103(4):045810, 2021.

[136] Mark G. Alford and Andreas Schmitt. Bulk viscosity in 2SC quark matter. *J. Phys. G*, 34:67–102, 2007.

[137] Mark G. Alford, Matt Braby, and Andreas Schmitt. Bulk viscosity in kaon-condensed color-flavor locked quark matter. *J. Phys. G*, 35:115007, 2008.

[138] Massimo Mannarelli and Cristina Manuel. Bulk viscosities of a cold relativistic superfluid: Color-flavor locked quark matter. *Phys. Rev. D*, 81:043002, 2010.

[139] Robert Bierkandt and Cristina Manuel. Bulk viscosity coefficients due to phonons and kaons in superfluid color-flavor locked quark matter. *Phys. Rev. D*, 84:023004, 2011.

[140] Lami Suleiman, Micaela Oertel, and Marco Mancini. Modified Urca neutrino emissivity at finite temperature. *Phys. Rev. C*, 108(3):035803, 2023.

[141] Mark G. Alford, Alexander Haber, and Ziyuan Zhang. Isospin Equilibration in Neutron Star Mergers. *arXiv:2306.06180 [nucl-th]*, 6 2023.

[142] L. Alvarez-Ruso, P. Fernandez de Cordoba, and E. Oset. The Imaginary part of nucleon selfenergy in hot nuclear matter. *Nucl. Phys. A*, 606:407–420, 1996.

[143] Michael E. Peskin and Daniel V. Schroeder. *An Introduction to quantum field theory*. Addison-Wesley, Reading, USA, 1995.

[144] Werner H. Keil. *Perturbative finite temperature field theory in Minkowski space*. PhD thesis, University of British Columbia, 1989.

[145] Armen Sedrakian. The Physics of dense hadronic matter and compact stars. *Prog. Part. Nucl. Phys.*, 58:168–246, 2007.

[146] Torbjörn Lundberg and Roman Pasechnik. Thermal Field Theory in real-time formalism: concepts and applications for particle decays. *Eur. Phys. J. A*, 57(2):71, 2021.

[147] Michel Le Bellac. *Thermal Field Theory*. Cambridge Monographs on Mathematical Physics. Cambridge University Press, 3 2011.

[148] Mikko Laine and Aleksi Vuorinen. *Basics of Thermal Field Theory*, volume 925. Springer, 2016.

[149] Carl Edward Rasmussen and Christopher K. I. Williams. *Gaussian processes for machine learning.* Adaptive computation and machine learning. MIT Press, 2006.

[150] Jie Wang. An intuitive tutorial to gaussian processes regression, 2022.

[151] Debora Mroczek, M. Coleman Miller, Jacquelyn Noronha-Hostler, and Nicolas Yunes. Searching for phase transitions in neutron stars with modified Gaussian processes. *J. Phys. Conf. Ser.*, 2536(1):012006, 2023.

[152] Daniel Foreman-Mackey, David W. Hogg, Dustin Lang, and Jonathan Goodman. emcee: The mcmc hammer. *Publications of the Astronomical Society of the Pacific*, 125(925):306–312, March 2013.

[153] Andrew W. Steiner, Madappa Prakash, James M. Lattimer, and Paul J. Ellis. Isospin asymmetry in nuclei and neutron stars. *Phys. Rept.*, 411:325–375, 2005.

[154] R. F. Sawyer and A. Soni. Transport of neutrinos in hot neutron-star matter. *The Astrophysical Journal*, 230:859–869, June 1979.